PLASMONIC PHOTOCHEMISTRY ON THE NANOSCALE

A Dissertation
Presented to
The Academic Faculty

by

CHUN-WAN YEN

In Partial Fulfillment
of the Requirements for the Degree
Doctor of Philosophy in the
School of Chemistry and Biochemistry

Georgia Institute of Technology
August 2011

PLASMONIC PHOTOCHEMISTRY ON THE NANOSCALE

Approved by:

Dr. Mostafa A. El-Sayed, Advisor
School of Chemistry and Biochemistry
Georgia Institute of Technology

Dr. Lawrence A. Bottomley
School of Chemistry and Biochemistry
Georgia Institute of Technology

Dr. Christopher Jones
School of Chemical and Biomolecular Engineering
Georgia Institute of Technology

Dr. Z. John Zhang
School of Chemistry and Biochemistry
Georgia Institute of Technology

Dr. Wendy L. Kelly
School of Chemistry and Biochemistry
Georgia Institute of Technology

Date Approved: May 9, 2011

To My Family

ACKNOWLEDGEMENTS

I would like to thank my advisor, Professor Mostafa A. El-Sayed, who supported and guided me during my five-year study at Georgia Tech. I also would like to express my appreciation to my committee members, Dr. Bottomley, Dr. Jones, Dr. Kelly, and Dr. Zhang, who provided insight and experience and helped make my thesis work better.

Thanks to all the LDL group members who provided professional knowledge and personal support. Especially, I would like to thank some past group members, Dr. Wei Qian, Dr. Wenyu Huang, and Dr. Christopher Tabor for their generous help. Dr. Li-Kang Chu shared his biophysics knowledge with me, and I could not have accomplished anything without his assistance. For the present group members, I would like to thank Mrs. Rachel Near who gave me great help with my English writing. Also, I would like to acknowledge Mr. Steven Hayden and Mr. Adam Poncheri for sharing my sorrow and happiness. I wish them all the best in their future.

I would like to express my gratitude to all of my friends in Atlanta for fulfilling my life, especially Mrs. Tze-Huei Chan, who takes care of me and makes me feel like I have a home in Atlanta.

Finally, I would like to thank my parents, my sister, and Hunghao for their support and understanding. Pursing a Ph.D degree is never an easy task, but their wholehearted love makes it much easier.

TABLE OF CONTENTS

LIST OF TABLES

LIST OF FIGURES

LIST OF SYMBOLS AND ABBREVIATIONS

bR	Bacteriorhodopsin
WT	Wild Type
PM	Purple Membrane
LA	Light Adapted
DA	Dark Adapted
LSPR	Localized Surface Plasmon Resonance
SPR	Surface Plasmon Resonance
NPs	Nanoparticles
AuNCs	Gold Nanocubes
ITO	Indium-tin-oxide
NIR	Near Infrared
MW	Molecular Weight
HOMO	Highest Occupied Molecular Orbital
LUMO	Lowest Unoccupied Molecular Orbital
PVP	Polyvinylpyrrolidone
TEM	Transmission Electron Microscopy
SEM	Scanning Electron Microscopy

SUMMARY

Over the past decade, nanomaterials have been the subject of enormous interest. These materials are notable for their tunable properties that exist when material's size is confined and show potential for use in wide-ranging industrial, biomedical, and electronic applications. The purpose of this thesis is to discuss some of the photochemistry that occurs on the nanoscale; especially those photochemical reactions that are adjustable by plasmonic metal nanoparticles.

When nanoparticles are small in size compared to the wavelength of incident light, a localized surface plasmon resonance occurs. For certain noble metals, such as gold and silver, this frequency occurs in the visible or near IR range, and therefore it can be utilized for many important applications. Only silver and gold nanoparticles were utilized in this thesis work, and they were used in application for three separate files: environment, catalysis, and energy.

The first application involves using gold nanocages for azo-dye degradation. Azo-dyes are frequently used in the textile industry and are toxic and carcinogenic. These dyes are typically released through waste water and thus are a threat to the surrounding ecosystem. The most challenging problem for removal of these pollutants is that azo-dyes are not compatible with traditional environmental treatment processes. A new nanoreactor, gold nanocages with unique hollow interiors, is developed to overcome this obstacle. The inner layer of a gold nanocage is silver and the outer surface is gold. When a gold nanocage is purged with oxygen gas, the silver atoms can be easily transformed to silver oxide. The band gap of silver oxide is 2.5-3.1 eV and it is therefore an analog of

other metal oxide materials, allowing it to absorb the energy from light and produce radicals to perform photodegradation of azo-dyes. The photocatalyic efficiency of these hollow gold nanocages is better than that of solid catalysts because the surface-to-volume ratios is higher in gold nanocages and also because of the increased likelihood of the azo-dyes contacting hydroxyl radicals since the reactants can be confined within the cages.

The second application is to use the photothermal effect for catalysis. The photothermal effect is when plasmonic metal nanoparticles rapidly convert absorbed light energy into heat and the heat from the metal lattice dissipates into the surrounding environment by phonon-phonon relaxation. Therefore, plasmonic metal nanoparticles can be regarded as a thermal agent. This characteristic is most often applied to cancer therapy. This is the first time that photothermal effect has been utilized to enhance the catalysis of the electron transfer reaction between hexacyanoferrate and thiosulfate. Two different types of plasmonic gold nanoparticles were prepared: gold nanospheres with a surface plasmon resonance band at 527 nm and gold nanocages with a surface plasmon resonance band at 796 nm. Two continuous wavelength laser were used, 514 and 808 nm, to irradiate the gold nanospheres and the gold nanocages, respectively. The gold nanoparticles served not only as a catalyst but also as a heating source to increase the reaction solution temperature. The properties of gold nanoparticles remained the same even after extended exposure to the laser. This technique can be used for accelerating thermal or photochemical reactions and may have the potential to heat reactions via solar energy.

The last application involves applying the plasmonic field of silver nanoparticles to bacteriorhodopsin, which is a photosynthetic system and a future candidate for use as

alternative energy. Bacteriorhodopsin (bR) can transfer light energy into electrochemical energy by utilizing a proton gradient. However, the photocurrent density values reported so far are around 0.2-40 pA cm^{-2} in thin film systems, which also require an external bias. In this thesis work, a non-thin film (solution) based electrochemical cell was successfully built up which did not require any external bias. The cell design used commercially available indium tin oxide glass as optical windows and electrodes. Small amounts of bR suspensions were utilized as the photovoltaic medium to generate the proton gradient between two half-cells separated by a molecular porous membrane. The maximum photocurrent density was 1.5 nA/cm^3, which is orders of magnitude higher than previous reports. To achieve an even higher photocurrent, metallic nanoparticles were prepared and incorporated into bR. Silver nanoparticles whose surface plasmon resonance overlaps well with the longest-lived intermediate of the bR photocycle (M_{412}) show a significant enhancement of photocurrent generation. The plasmonic field of silver nanoparticles can effectively increase the flux of blue photons and the bypassed photocycle is formed due to this enhanced blue light effect. The photocurrent generation of bR in the presence of silver nanoparticles can be as high as 25 nA/cm^3, 15 times higher than pure bR. The bypassed photocycle is formed, most notably affects the rates of bR ground state recovery and M_{412} formation. Spectroscopy is utilized for measuring the effect of the plasmonic field of the silver nanoparticles on the kinetics. The photocurrent generation of bR is still limited to the nano-ampere range. As an extension, bR was assembled onto TiO_2 nanotubes for water splitting applications. The generated photocurrent density was 0.65 mA/cm^2, which is a ~ 50% increase as compared to that measured for pure TiO_2 nanotubes (0.43 mA/cm^2) fabricated and tested under the same conditions. This

enhancement in photocurrent can be related to the unique proton pumping ability of bR as well as to the novel structural properties of the fabricated nanotube arrays.

CHAPTER 1

INTRODUCTION OF NANOMATERIALS AND BACTERIORHODOPSIN

ABSTRACT

This chapter is an introduction to metal nanomaterials and bacteriorhodopsin. First, the origins and properties of metal nanoparticles are introduced. The common methods of metal nanoparticles synthesis are also mentioned. The unique optical properties of metal nanoparticles, especially gold and silver, can be applied to various applications, including alteration of the bacteriorhodopsin photocycle and photothermal therapy, which are also discussed. Second, the structure and photocycle of bacteriorhodopsin are introduced. The use of bacteriorhodopsin for energy generation is also mentioned. Finally, the organization of the dissertation is presented.

1.1 Properties and Applications of Nanomaterials

Origins of Nanomaterials

Nanomaterials have been a major area of interest in scientific research over the previous few decades. Nanomaterials are in the size range of 1-100 nm, and can be dispersed in gaseous, liquid, or solid media. Because the size of nanomaterials are intermediate between that of a macroscopic solid and that of an atomic system, nanomaterials possess unique optical, electronic, and chemical properties that are extremely different from individual atoms as well as their bulk counterparts.[1,2] Three major factors are responsible for these differences: high surface-to-volume ratio,[3-5] quantum size effects,[6] and electrodynamic interactions.[7]

The first synthesis of metallic gold nanoparticles was probably in the 4th century BC in Egypt and China. Since then, gold has been exploited for both its curative and aesthetic properties. The centuries old methods of using colloidal gold to make ruby glass and for coloring ceramics are still in use today. The most famous example is the Lycurgus cup, crafted by the Romans in the 4th century and can been seen in the British Museum in London.[8] When the cup is illuminated from the outside by white light, bluish-green light is scattered and the cup appears green. When the light is placed inside the cup, the glass absorbs the green light and remaining colors of the white light appear reddish-orange (Figure 1-1). Barber *et al.* revealed the presence of approximately 70 nm metal nanoparticles via transmission electron microscopy. X-ray analysis showed that these nanoparticles were a silver-gold alloy, with a ratio of silver to gold of about 7:3. This evidence confirms the dichroic effect is caused by colloidal metal nanoparticles.[9]

.

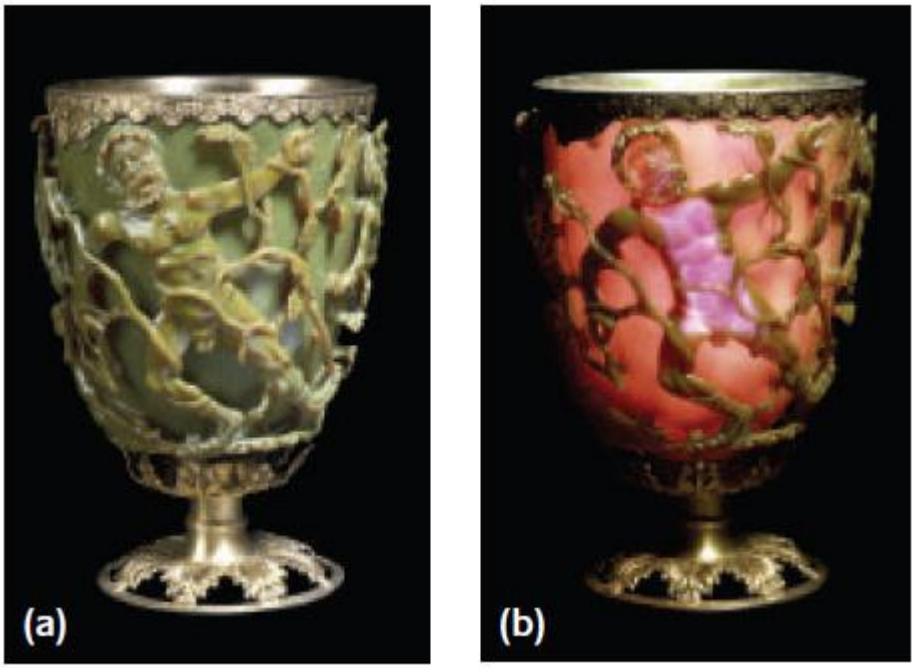

Figure 1-1: The Lycurgus Cup made by Romans around the 4th century AD. (a) When illuminated from the outside, it shows green (reflected light). (b) When illuminated from the inside, it glows red (transmitted light).

Optical Properties of Metallic Nanoparticles

One of the most interesting aspects of metal nanoparticles is their optical properties. In 1857, Michael Faraday was the first to scientifically study metallic nanoparticles in colloidal solutions, which exhibited colors from ruby red to amethyst.[10] He started to list the factors impacting the color of those solutions and evidenced that "the mere variation in the size of particles gave rise to a variety of resultant colors." The colors of white light absorbed and scattered by the small gold nanoparticles was first explained theoretically by Mie in 1908 by solving Maxwell's equation for spherical nanoparticles.[11] Mie theory attributes the plasmon band of spherical particles to the dipole oscillations of the free electrons in the conduction band occupying the energy states immediately above the Fermi energy level.[12] When gold nanoparticles are small enough, they display a ruby red color due to the strong absorption of green light at 520

nm, corresponding to the wavelength of the plasmon resonance that occurs for those gold nanoparticles.

The localized surface plasmon resonance (LPSR) is a phenomenon observed when the charge density of metallic nanoparticles oscillates. For a special domain of frequency, metallic nanoparticles interact with incident light, resulting in the collective of the conduction electrons of nanoparticles in resonance with the oscillation frequency of the incident light (Figure 1-2). This results in strong light scattering, the appearance of an intense surface plasmon absorption band and an enhancement of the local electromagnetic fields.[13-15] The frequency and intensity of the LSPR band are characteristic of the type of material,[16] and are highly sensitive to the size[17] ,shape[18], and local environment[19] of nanomaterials. The oscillation frequency is critically determined by four factors: the density of electrons, the effective electron mass, and shape/size of the charge distribution. In principle, one could control any of these parameters to tune the properties of metallic nanoparticles and further systematically vary the color of metallic nanoparticles (Figure 1-3).

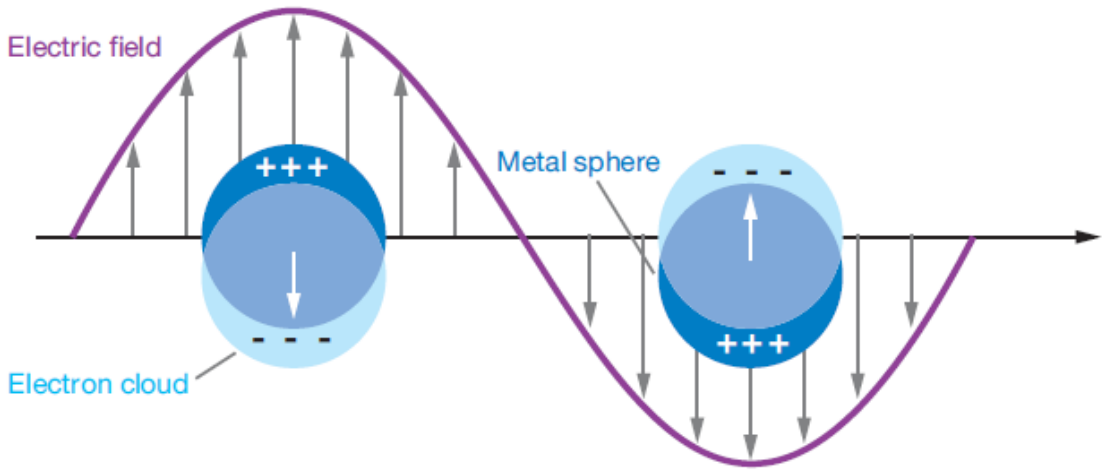

Figure 1-2: Schematic for localized surface plasmon resonance for a sphere, showing the displacement of the conduction electron charge cloud relative to the nuclei.

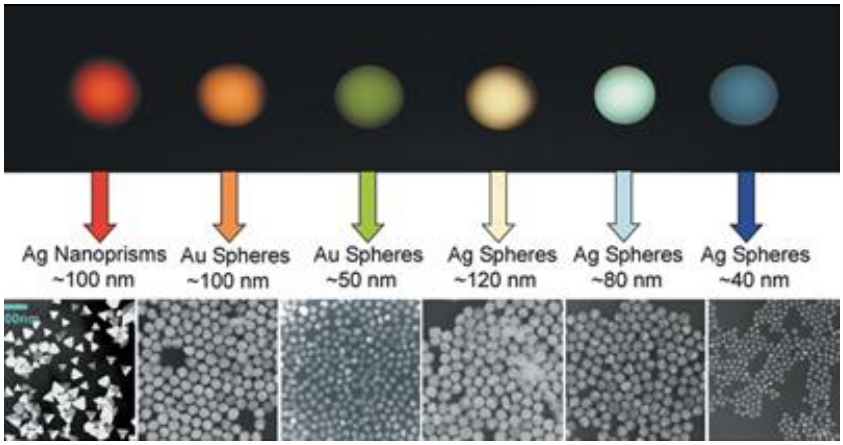

Figure 1-3: The optical properties of metallic nanoparticles are strongly dependent on the types of material, and are highly sensitive to the size and shape of nanostructures.

Methods of Metal Nanoparticles Synthesis

The ability to fabricate materials at the nanoscale level is crucial. Among the many attributes of nanoparticle scaffolds is their ability to be synthetically manipulated in term of size and shape, often exhibiting intrinsic functionality. In this section, some of methods used for metal nanoparticle synthesis are discussed.

Chemical Reduction Method

The chemical reduction methods used to prepare colloidal metal nanoparticles generally follows the same three-steps: (1) The precursor metal salt is dissolved into solution, (2) The precursor metal salt is reduced by a reducing agent, and (3) The metal particle grows in size as time progresses until a capping agent restricts the growth at a specific size and/or shape.

The chemical reduction method is the most common and simplest method of synthesizing metallic nanoparticles. The most popular one is the citrate reduction of metal salt in solutions, which was introduced by Tukevitch in 1951.[20] It leads to size of metal nanoparticles around 20 nm. In this method, citric acid acts both as a capping and

reducing agent. The size of metallic nanoparticles (between 16 to 147 nm) can be controlled by changing the citric acid to metallic salt ratio.[21]

The sodium borohydride reduction method is another common method of metal nanoparticles synthesis.[22-26] This method is generally fast, with metal nanoparticle formation occurring quickly after the addition of sodium borohydride. Metallic nanoparticles of various compositions, such as platinum, palladium, gold and silver have also been synthesized using the sodium borohydride reduction method in the presence of polymer protecting agents. The size of the metal nanoparticles produced via the sodium borohydride reduction method is usually less than 10 nm.

There are several other reduction methods that have been used to synthesize metal nanoparticles. Organic solvents (alcohol and methanol) act both as a solvent and reducing agent and the reduction of the metal salt takes place when the solution is refluxed in the presence of protecting polymer.[27-32] The use of solvent as a reducing agent results in a fast reduction of the metal salt and the solvent is oxidized to form a carbonyl compound after the reduction process. Hydrogen gas can be used as a reducing agent for the preparation metal nanoparticles.[33-35] The hydrogen reduction method involves bubbling hydrogen gas into a metal salt solution and nanoparticles can be formed after several hours of bubbling.

Physical Methods: Photochemistry, Sonochemistry, and Theromolysis

Light irradiation is another tool that can improve the quality of metallic nanoparticles. The photochemical reduction method can be divided into two mechanisms: reduction of metal salt by radiolytically produced reducing agents or degradation of an organometallic complex by radiolysis.[36,37] The radiation sources include X-ray or gamma-ray radiation and also UV-visible radiation by the use of a xenon or mercury lamp. Radiolysis produces solvated electrons in aqueous solution to form new radicals that are able to reduce metal salts.

The sonochemical reduction method of a precursor metal salt involves generation of an active species, reduction of the metal salt, and growth of the nanoparticle in a sonicated liquid.[38,39] A sonication method involves the formation, growth, and explosion of bubbles in liquid media. These steps include: in gas phase into the cavitation bubbles where high temperature and pressure allow water pyrolysis to form H and OH radicals, at the interface between the cavitation bubbles and the solution, and finally in the solution. The reduction process mainly takes place at the bubble/solution interface and in solution and does not take place in the gas phase due to the low vapor pressure of the precursor transition metal salts.

The thermal reduction of the precursor metal salt is a reduction method involving the decomposition of the precursor metal salt to the zerovalent form.[40,41] Thermolysis conditions such as reaction temperature and reaction time affect the size of nanoparticles. Thermal reduction method can be performed by using a laser as the heating generation source and the size of the resultant nanoparticles can be controlled by adjusting the laser settings.

Two-Phase Synthesis

The two-phase reduction method was developed by Schiffrin *et al* in 1993.[42] This method has had a considerable impact on the overall field in the past two decades because of the facile synthesis of thermal and air stable metal nanoparticles with controllable sizes. This method is inspired by Faraday's two-phase system and uses thiol ligands that strongly bind transition metals due to the soft character of both the transition metal and sulfur.[43] A precursor metal salt is transferred to toluene using tetractylammonium bromide (TOAB) as the phase-transfer reagent and reduced by sodium borohydride. Depending on the ratio of metal salt to capping agent (thiol or amine), the size of nanoparticle can be tuned between 1 and 10 nm. A single toluene phase method was also reported whereby ammonium salt-stabilized metal nanoparticles

were synthesized, followed by an exchange reaction with dodecanethiol.[44] Murray *et al.* have enhanced this method's popularity by offering various functional thiols, which has opened a new area of the two-phase method.[45]

Applications of Nanomaterials

The unusual size-dependent properties of metal nanoparticles have motivated a great number of researchers devoted into this field. Fascinating aspects of nanomaterials include size-related electronic, magnetic and optical properties (quantum size effect), and their applications to catalysis and biology. Nanotmaterials will be key materials and building block in the 21st century. Details of applications on optical property, photothermal effect, and catalysis involved in the dissertation work will be discussed in this section.

Application using Optical Property

Confinement and quantization of conduction electrons within a small volume enhance the optical conductance property of nanomaterials. When the dimensions of nanoparticles become smaller than the wavelength of exciting light, energy can be confined in the small spatial regions through the local excitation of the surface plasmon resonance. The enhanced fields in these regions are used in a wide range of applications including optical energy transport,[46] biological sensors,[47] surface-enhanced Raman scattering (SERS),[48] and waveguide.[49]

In this dissertation, the effect of the unique optical properties of metal nanoparticles the dynamic change of bacteriorhodopsin (bR) is of interest. Biesso *et al*. have reported alterations of the bacteriorhodopsin photocycle when a plasmonic field is introduced into the system.[50] The primary step of the bacteriorhodopsin photocycle involves the retinal isomerization of a protonated Schiff base. The sequence of events of the primary step is:

$$bR_{568} + h\nu \rightarrow (bR)_{FC}^{*} \rightarrow I_{460} \xrightarrow{500\ fs} J_{625} \xrightarrow{3\ ps} K_{610}$$

Biesso *et al* incorporated bR with citrate capped gold nanosphers (Figure 1-4) and used femtosecond time-resolved pump-probe spectroscopy to examine the effect of the plasmonic field effect during the transition of the intermediate I_{460} and J_{625}.

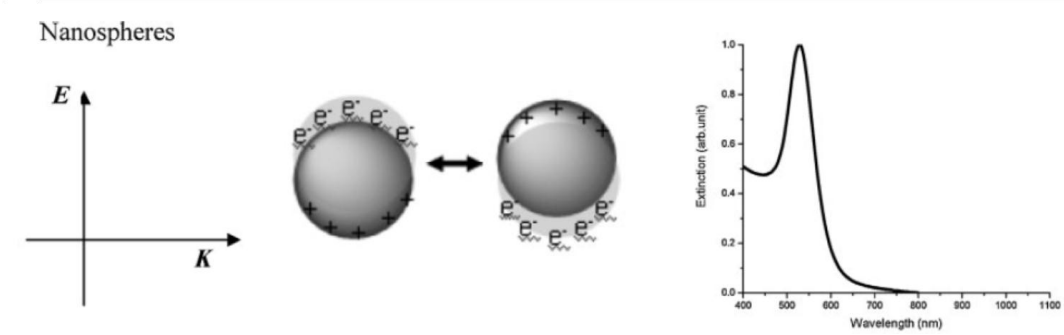

Figure 1-4: Gold nanosphere shows single surface plasmon resonance band in the visible range.[51]

The absorption of light by the retinal component of bR is followed a large charge redistribution in the protonated Schiff base is followed. This charge system is unbalanced and these should induce a large polarization on the protein cavity around the retinal electronic system. In the presence of a plasmonic electric field, the retinal electronic system will have a different potential energy surface than the unperturbed system. The plasmonic field of gold nanospheres should affect the rate of dynamic of bR within the protein pocket and affect the decay rate of I_{460} (Figure 1-5).

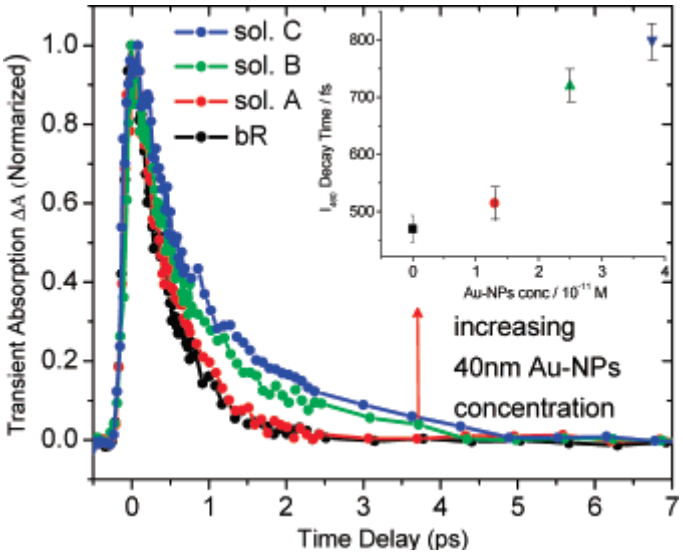

Figure 1-5: Effect of increasing the concentration of citrate-capped gold nanospheres on the dynamics of the primary step (the decay of I_{460}) of bR.[50]

Biesso *et al* also mentioned the M_{412} intermediate decay kinetics in the presence of plasmonic field of gold nanorods.[52] Upon absorption of light, bR undergoes a photocycle involving several intermediates where structural rearrangements take place. Among all of the intermediates, M_{412} is the longest-lived and the most studied. The decay of M_{412} was measured via flash photolysis carried out using a frequency doubled nanosecond laser at 532 nm. An NIR cw laser at 808 nm continuously excited the gold nanorods whose surface plasmon resonance absorption occurs at 795 nm (Figure 1-6).

l Nanorods

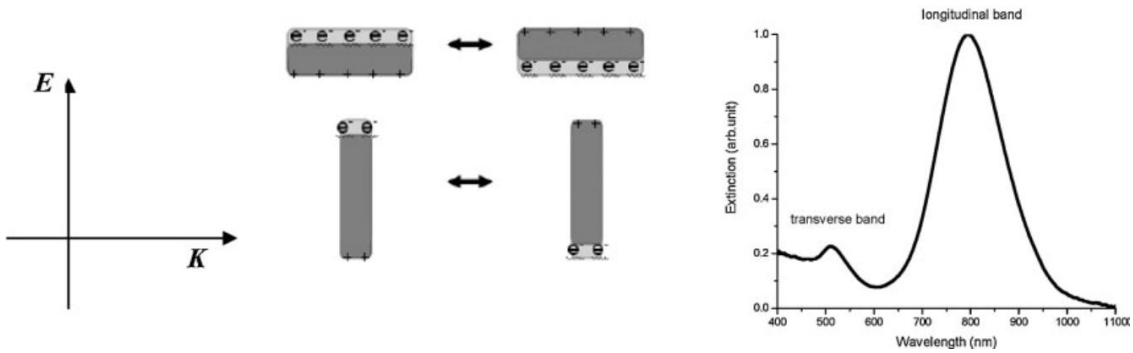

Figure 1-6: While gold nanospheres show one SPR band in the visible region, gold nanorods show two bands: a strong longitudinal band in the near-infrared region corresponding to electron oscillation along the long axis and a weak transverse band, similar to that of gold nanospheres, in the visible region corresponding to electron oscillations along the short axis.[51]

In the presence of gold nanorods, the decay time of M_{412} decreased as the concentration of gold nanorods increased. The dependence of the decay time constant on the concentration of gold nanorods is shown in the inset of Figure 1-7. Gold nanorods are known to efficiently convert absorbed photons into heat through electron-electron or electron-photon relaxation. Therefore, the decrease in M_{412} lifetime observed in the presence of gold nanorods may be due to the heat transfer from gold nanorods to the bR medium.

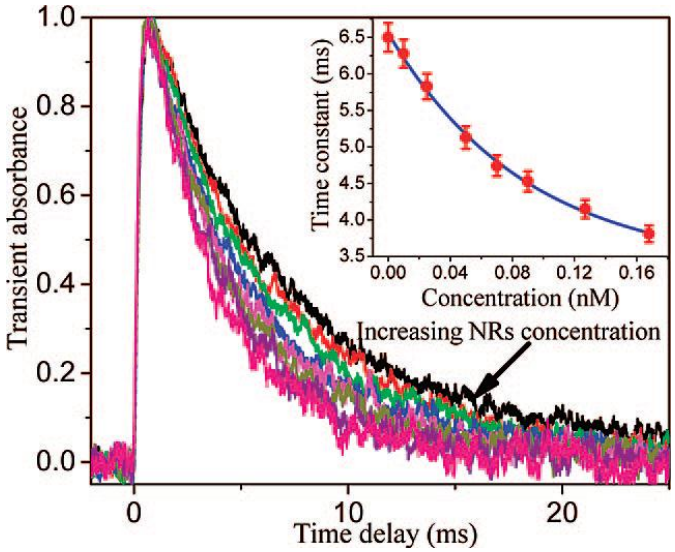

Figure 1-7: Dependence of the decay kinetics of M_{412} on gold nanorods concentration in the presence of NIR laser irradiation. Each decay lifetime value was obtained by fitting the decay kinetic with a single exponential function.[52]

Photothermal Effect

When a plasmonic metal nanoparticle absorbs light, its free electrons it are excited. Excitation at the plasmon resonance frequency causes a collective oscillation of the nanoparticles' free electrons. The excitation is converted to heat via electron-electron and electron-phonon relaxations on the time scale of picoseconds. Subsequently the heat generated from plasmonic metal nanoparticles is dissipated into the surrounding environment. This rapid photothermal conversion can be utilized for the localized heating. Plasmonic metal nanoparticles can heat the surrounding medium immediately by employing light radiation with a frequency strongly overlapping with the surface plasmon resonance absorption of plasmonic metal nanoparticles.[53,54]

The photothermal effect of plasmonic metal nanoparticles is widely applied in biological systems. Three methods of exploiting the photothermal effect are: (1) hyperthermia, (2) optically triggered bond opening, and (3) drug delivery.

Hyperthermia uses the photothermal effect of nanoparticles to induce cell death in biological system.[55-57]: Cells are very sensitive to small increases in temperature; a rise of

only few degrees in temperature can lead to cell death. The plasmonic heating of metal nanoparticles holds great promise for cancer therapy or bacterial infection. The idea is to direct plasmonic metal nanoparticles to surrounded to cancer tissues. Metal nanoparticles are targeted to cancer cells by conjugating the surface of metal nanoparticle with ligands that are specific to receptors overexpressed on cancer cells. By external irradiation with a certain wavelength of light, plasmonic nanoparticles can convert the light to heat, causing the surrounding cancer cells to be selectively killed. Thus, heat generated by plasmonic nanoparticles can destroy cancer tissues locally without exposing the entire the entire organism to elevated temperatures (Figure 1-8a).

(2) Optically triggered opening of bonds: The binding of complimentary oligonucleotides to double stranded DNA is temperature dependent. When DNA is linked to plasmonic metal nanoparticles, a local temperature increase can be induced by plasmonic nanoparticles, which can trigger the breaking of DNA bonds (Figure 1-8b).[58] (3) Drug Delivery: plasmonic nanoparticles can also be used to remotely control the release of drug from containers (Figure 1-8c).[59] The drug is embedded inside a container, which is functionalized with plasmonic nanoparticles. The wall of container breaks upon optical excitation of the plasmon nanoparticles, thus releasing the drug.

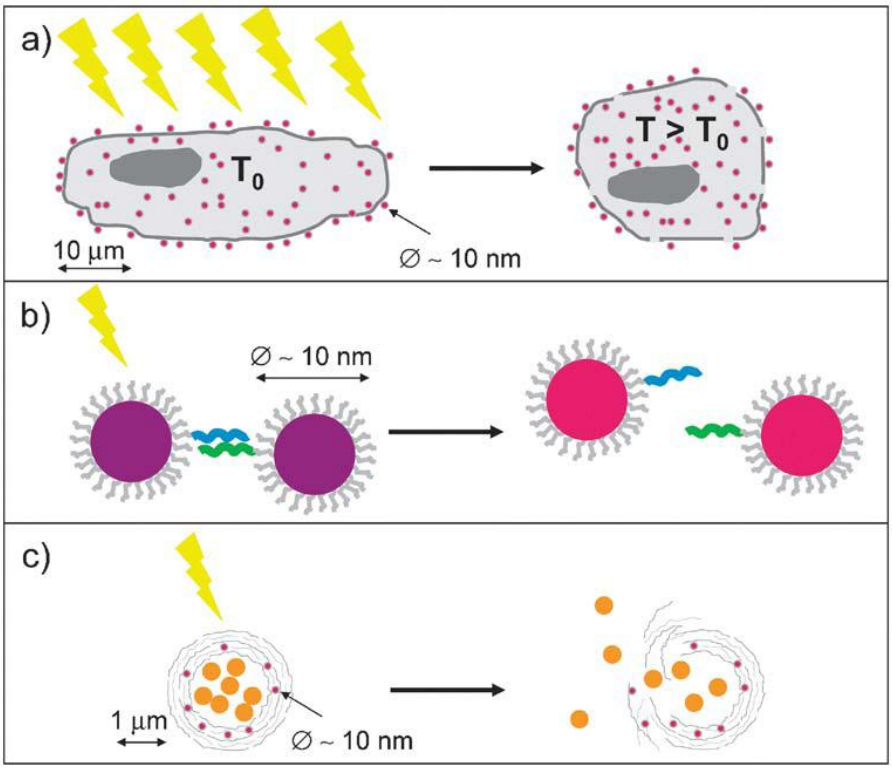

Figure 1-8: (a) Hyperthermia: the temperature inside cells (drawn in gray) is raised by illumination of plasmonic nanoparticles, leading to cell death. (b) Breaking of bonds: when plasmonic nanoparticles (core in red, stabilizing shell in grey) are conjugated with ligands (shown in green) that are specific to receptors (shown in blue) which are bound to other plasmonic nanoparticles, these two kinds of plasmonic nanoparticles will be linked to assemblies mediated by receptor–ligand binding. As the distance between the particles in such aggregates is small, their plasmon resonance is shifted to higher wavelengths and the particle solution appears violet/blue. Upon illumination the plasmonic nanoparticles get hot and the bonds of the receptor–ligand pairs melt. Therefore the assemblies are dissolved, the average distance between the particles is increased, and the particle solution appears red. (c) Drug delivery: plasmonic nanoparticles are embedded in the walls of polyelectrolyte capsules. The capsule cavity is loaded with drug (drawn in orange). Upon illumination the heat created by the nanoparticles causes local ruptures in the capsule walls and thus release the drug.

Catalysis

Until recently, noble metals have been considered among the least catalytically useful metals. However, after Haruta *et al* used gold nanoparticles supported on metal oxides and found its extremely high catalytic ability on CO oxidation in 1989, catalysis with metal nanoparticles is now an expanding area and a large number of new catalytic systems for various reactions are now being explored.

As the size of a noble metal particle decreases, its surface area increases and also allows a greater proportion of its atoms or molecules to be displayed on the surface rather than the interior of the material. Figure 1-9 shows the inverse relationship between the particle size and the number of molecules expressed on the particle surface.[60] The enormous surface-to-volume ratio of metal nanoparticles makes them attractive for catalysis.

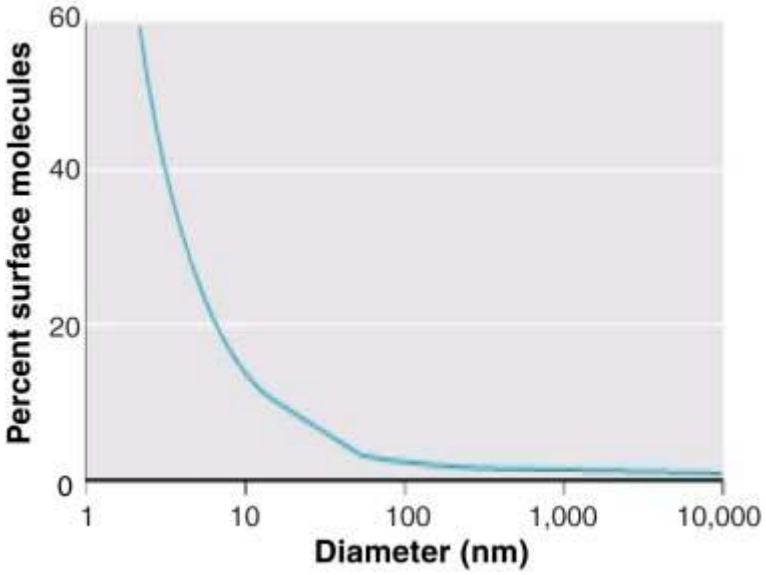

Figure 1-9: Inverse relationship between particle size and number of surface-expressed molecules. For instance, in a particle of 30 nm size, about 10% of its molecules are expressed on the surface, whereas at 10 and 3 nm size the ratios increase to 20% and 50%, respectively. The number of atoms or molecules on the surface of the particle can determine the activity of material.[60]

1.2 Basic Properties of Bacteriorhodopsin

Structure of Bacteriorhodopsin

Bacteriorhodopsin (MW=26,000) is the light transducing membrane protein usually found in two-dimensional crystalline patches (purple membrane) of *Halobacterium halobium* (Figure 1-10).[61-64] This bacterium grows in high salt conditions (4 M NaCl). The purple membrane, which contains the bacteriorhodopsin protein in a lipid matrix, is grown by the bacterium when the concentration of oxygen becomes too low to sustain the generation of ATP. Bacteriorhodopsin is a one of the nature photosynthetic system: it can convert absorbed sunlight into proton gradient (details of proton transport of bR are discussed in the next section). The bR protein is constituted of 248 amino acids, organized in 7 α-helices. The protein is about 4.7 nm long, and it traverses the entire width of the membrane. The horizontal cross-section of bR range from 2.5 to 3.5 nm in diameter, excluding its conjugated lipids.[65]

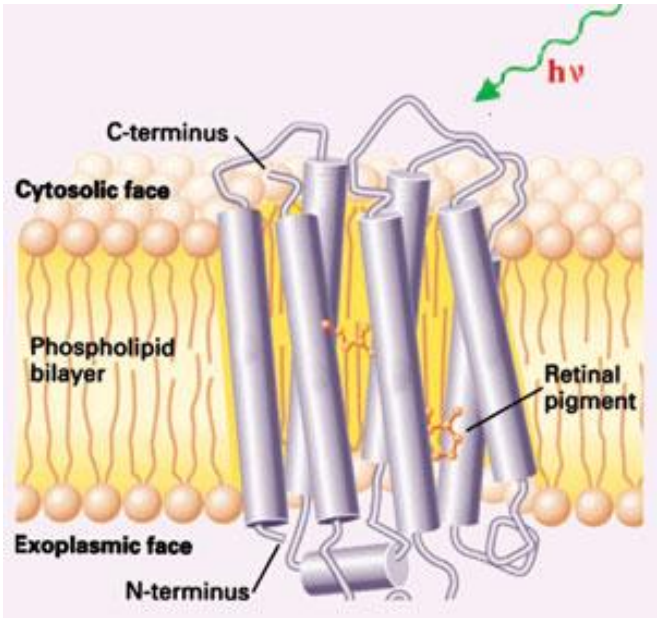

Figure 1-10: Bacteriorhodopsin consists of 249 amino acids which are arranged in seven α-helical bundles inside the lipid membrane and from a cage where retinal is in the center of it.

Surrounded by the α-helices, in a tight protein pocket, lies the retinal protonated Schiff base, which is covalently attached to the protein through the residue Lys-216 on helix G (Fig 1-11). The Schiff base is perpendicular to the helices, and is located roughly midway through the membrane thickness, at an angle of about 20 degrees with respect to the membrane plane.[66,67] To allow vectorial proton transport, deprotonation and reprotonation of the Schiff base must occur from different sides of the membrane. Thus, the accessibility of the Schiff base to its two facilitating residues, Asp96 and Asp 85, must be switched during the photocycle. The retinal divides the protein cavity into two half channels. One is the extracellular channel, which contains polar residues that from hydrogen channels with the nearby peptides and provides an overall polar environment. The other is the cytoplasmic channel, which is mostly hydrophobic. The geometry of the retinal, the protonated Schiff base, and its precise electrostatic interaction with the surrounding charges (Asp85, Asp212, and Arg82) and dipoles tune the absorption maximum to fit the protein's biological function.

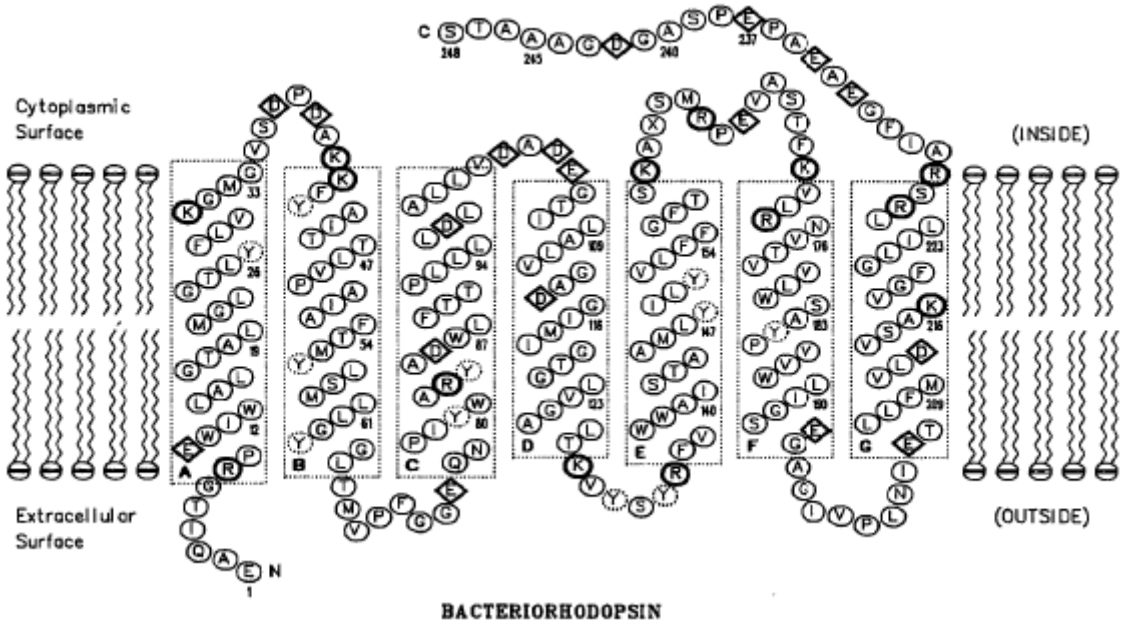

Figure 1-11: Amino acid sequences and putative membrane spanning regions of bacteriorhodopsin. Amino acids which under normal conditions carry a charge are shown in thickened circles (positively charged) or boxes (negatively charged).

Photocycle of Bacteriorhodopsin

Bacteriorhodopsin is a light-driven proton pump, which moves protons from the cytoplasmic side to the extracellular side of the membrane. This light-induced proton pumping generates a proton (electrochemical) gradient that the bacterium uses to synthesize ATP in the absence of oxygen. After bR is kept in darkness for a period of time, the retinal reaches equilibrium between two isomers: all-*trans* and 13-*cis* with a ratio of 50:50. This is known as the dark adapted state of bR, and the maximum absorption is at 560 nm.[68] After light absorption, bR converts to a light-adapted state with a maximum absorption at 568 nm (ratio of all-*trans* and 13-*cis* is 95:5).[69] The experiments of bR presented in the dissertation all used light-adapted bR.

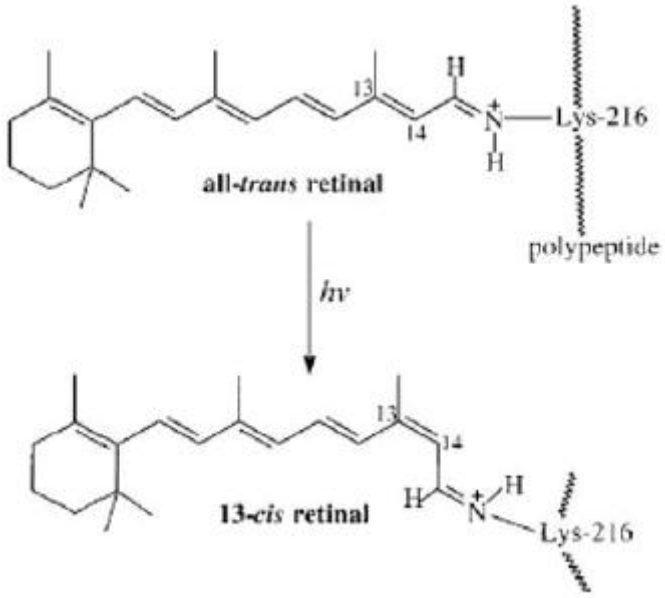

Figure 1-12: Under illumination by visible light, all-*trans* light-adapted bR is isomerized to the 13-*cis* conformation, which initiates the bR photocycle.

Light absorption triggers isomerization of the all-*trans* configuration of retinal to the 13-*cis* isomer (Figure 1-12).[70] This event initiates the photocycle of bR (Figure 1-13), a sequence of transitions through various intermediates with different spectral absorption properties (Figure 1-14). The retinal and its configurational transformations have been well characterized in a variety of spectroscopic studies using techniques ranging from X-

ray,[71] Raman,[72] FTIR,[73] and NMR spectroscopy.[74] The light-driven proton transport process is initiated by absorption of light around 560 nm, followed by an immediate charge separation step. The charge transport through the molecule is associated with deprotonation and reprotonation of the retinal Schiff base linkage.

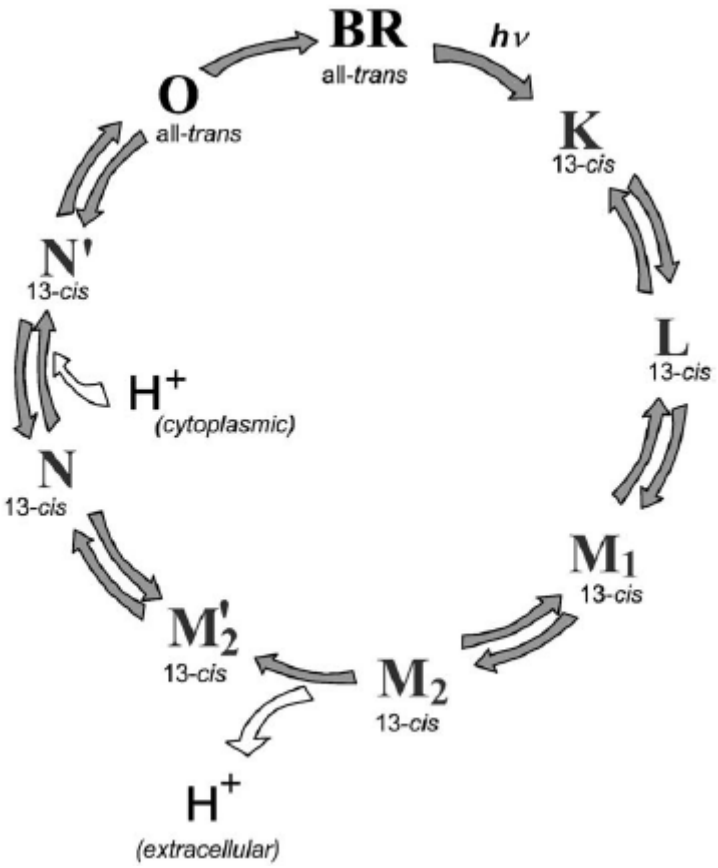

Figure 1-13: Photocycle scheme from the kinetics of bacteriorhodopsin. Only the bR and O states contain all-*trans* retinal; in all other states the retinal is 13-*cis*. Proton release to the extracellular state, occurs as the M_2 state progresses the M_2' state, and from the cytoplasmic side occurs as N progresses to N'.[75]

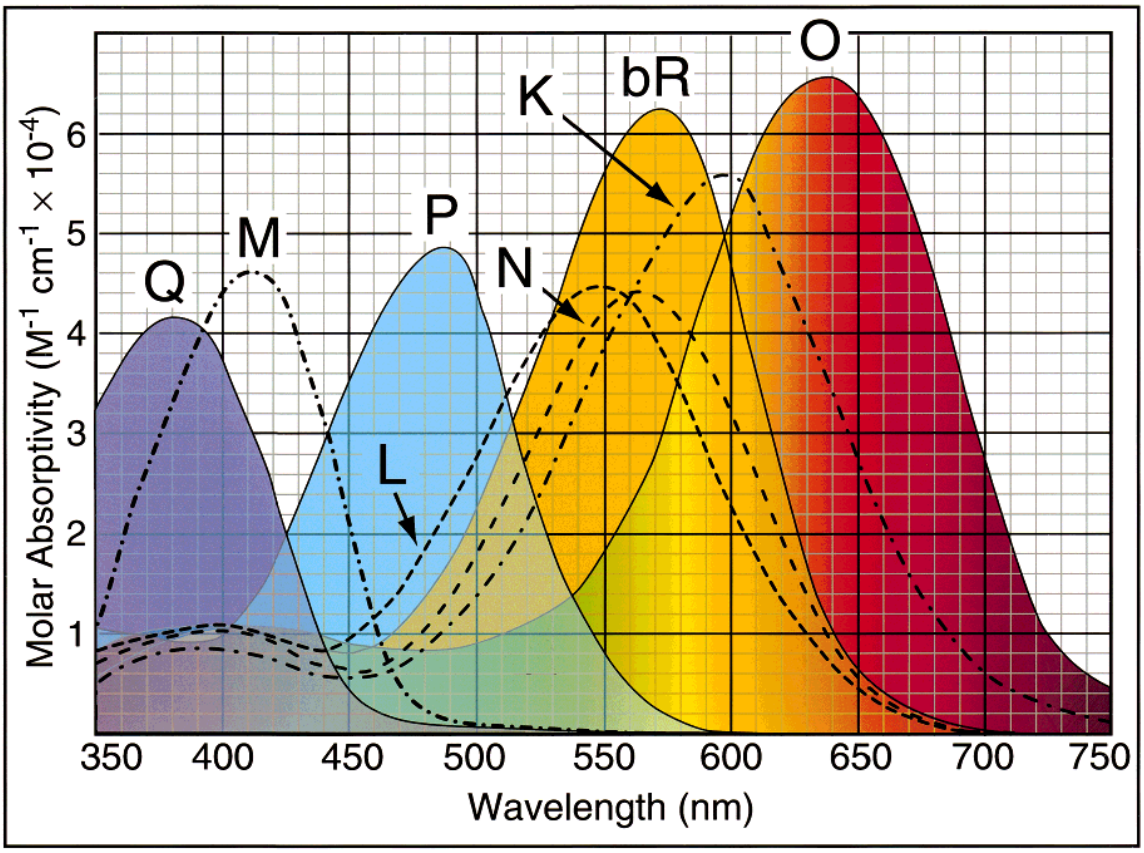

Figure 1-14: The absorption spectra of the main intermediates in the bR photocycle.[76]

The initial bR state, as well as each of the intermediates, has a single, broad and asymmetric absorption band in the visible range (Figure 1-14). The maximum absorption of most of these states lies between 550 to 620 nm, with the exception of M intermediate which has a strongly blue-shifted maximum at 410 nm. Following photoexcitation of bR, the red-shifted K intermediate builds up within a few picoseconds, followed by formation of the blue-shifted L intermediate on a microsecond time scale (Figure 1-14).

It should be emphasized that the only light dependent event in the conventional photocycle of bR is the initial isomerization of the retinal. All subsequent steps are thermal relaxation. The proton pumping cycle comprises sequential transfer steps between pairs of donor and acceptor groups extending across the protein. Three of the

groups are critical: the protonated Schiff base, the anionic Asp85 near the extracellular side, and the protonated Asp96 near the cytoplasmic side. They divide the protein into three domains, the Schiff base domain, the proton release domain, and the proton uptake domain.

The primary proton transfer event from the Schiff base to Asp85 (step 1 in Figure 1-15) defines the L-to-M spectral transition, which induces a large blue shift in the absorption maximum. Concurrent with protonation of Asp85, a proton is released to the extracellular medium with a time constant of about 50 μs on step 2 in Figure 1-15.[77] Meanwhile, a large structure rearrangement on the cytoplasmic side of the protein occurs. These arrangements open a switch of the retinal, so the Schiff base can subsequently be reprotonated from Asp96 (step 3 in Figure 1-15) on the cytoplasmic side.[78] This corresponds spectrally to the M_2 to N transition and have a time constant of about 1 ms. Asp96 is reprotonated from the cytoplasmic medium (step 4 in Figure 1-15), and the absorption peak is further red-shifted as the retinal thermally reisomerizes to recover the all-*trans* configuration. This is associated with the N to O transition and has a time constant of about 2 ms. Finally, the ground state is recovered when a proton is transferred from Asp 85 to the release group on the extracellular side via Arg82 with a time constant of about 8 ms (step 5 in Figure 1-15).

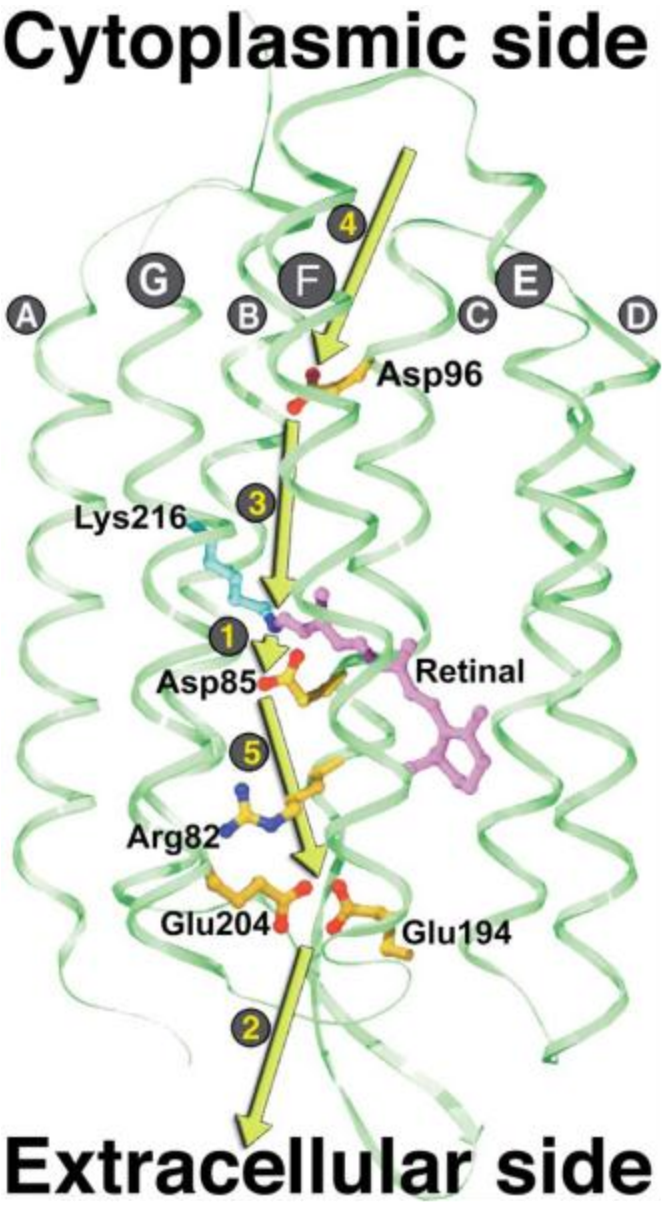

Figure 1-15: Yellow arrows show the proton transfer steps in the bR photocycle. The primary proton transfer (1) is from the Schiff base to Asp85. A proton is released to the extracellular medium (2) by the proton release group, thought to be formed by Glu194, Glu204 and water molecules. The Schiff base is subsequently reprotonated from Asp96 (3), which is then reprotonated from the cytoplasmic medium (4). The final proton transfer step (5) from Asp85 to the proton release group (via Arg82) restores the ground state.[79]

pH effect

The sequence of proton transfer reactions of bR discussed above is pertinent under normal biological conditions that is pH > 5.8. Proton transfer reactions are intrinsically dependent on the pH values and the photocycle of bR is no exception with a different pathway being followed for low and high pH (Figure 1-16). When the environmental pH is higher than 5.8, the proton release to the extracellular side occurs during the interconversion of the M state and the proton uptake occurs in the transition of N→O. The time scale of this proton release reaction proceeds in the microsecond domain. At pH < 5.8, the proton uptake occurs during the transition from N→O, prior to the proton release during the transition from O→ bR. Here, the time domain of proton release is delayed into the late millisecond range. The reason for this change is proton kinetics in the photocycle is that the p*K*a of the proton release group involved in this proton pumping cycle is 5.8.[80-83] Hence, the switch is at pH = 5.8.

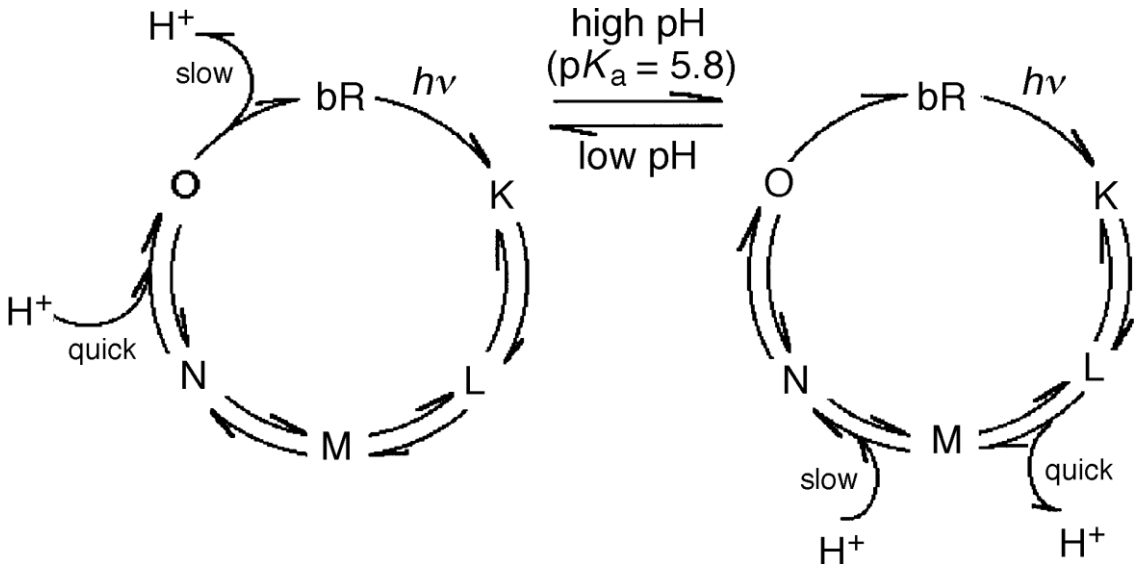

Figure 1-16: A simplified model for the bR photocycle at low and high pH. The proton pump sequence is changed by the pH due to the proton release group with a p*K*a=5.8. At high pH, proton release (through the L→M reaction) precedes uptake (through the M→N reaction), whereas at low pH, this sequence is reversed and the O intermediate is involved rather than N or M.[83]

Blue Light Effect

During the photocycle of bR, the two most interesting configurations of the proton are the bR ground state with a protonated Schiff base (λmax=570 nm) and the long-lived intermediate, M_{412}, with a deprotonated Schiff base (λmax=412 nm). The M_{412} is generated following the retinal isomerization in 70 μs and can revert to the bR ground one of two ways. The first is the traditional thermal relaxation through a number of other intermediates (M_{412}→N→O→bR_{570}), which takes 15 ms. The second is a much more rapid photochemical process that occurs upon excitation with blue light in nearly hundreds of nanoseconds. This is the known blue light effect. M_{412} can be photoexcited by applying an intense blue light and this transition from M_{412} to bR_{570} can be summarized as M→M´→bR.[84,85] The primary reaction M→M´ is attributed to a 13-*cis*→all-*trans* isomerization of retinal in picoseconds, and the M´→bR transition has been interpreted in terms of Schiff base reprotonation in 200 nanoseconds. Hessling *et al*. have demonstrated the depletion of M intermediate via this effect by an FT-IR study (Figure 1-17a).[86] Blue light effect can be applied in various fields. One of them is energy generation: since a short-cut of the photocycle is formed, the proton released rate is also enhanced. Another example is to use the switchable characteristic of bR to record negative values of light intensity. Lewis *et al* has demonstrated that the value of a pixel in an image can be represented by the concentration of the bR or M state.[87] Shining yellow light on a pixel would increase the concentration of the M state, whereas shining blue light would increase the concentration of the bR state. If a film is originally prepared with equal concentrations of bR and M, then negative and positive values can be represented as increases in the concentrations of bR or M that correspond to a surplus of blue or yellow light, respectively (Figure 1-17b). They used this characteristic of such a bR film to approximate the operation of a difference of Gaussians.

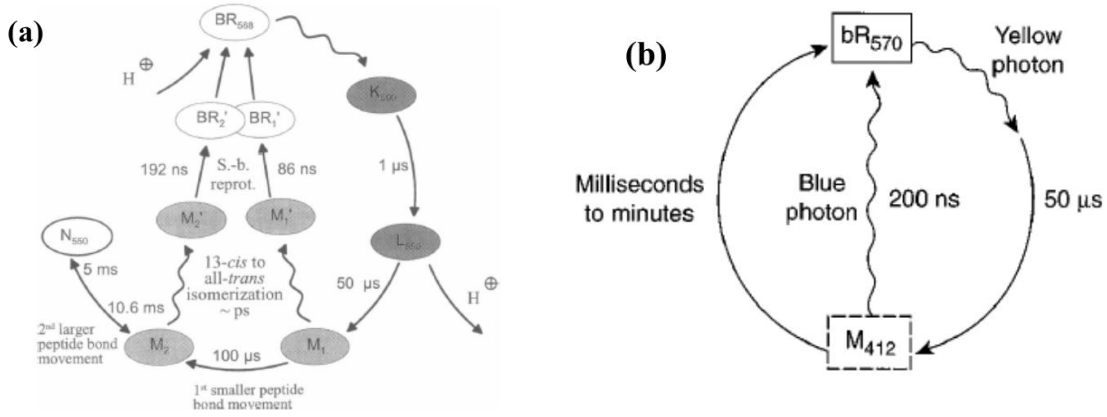

Figure 1-17: (a) Refined photocycle model considering the results of double flash experiments in the infrared spectral region. M intermediates can either be thermally relaxed through a series of intermediates change to the bR ground state with a time constant of 50 milliseconds or photochemically converted back to bR ground state with a time constant of hundreds of nanoseconds.[86] (b) Simplified photocycle model of bR considering only the initial ground state and the longest living intermediate M_{412}.[87]

Light Harvesting Proton Pumping for Bioenergy

Global demand for energy is increasing with population growth and modernization. The world energy consumption is close to 3.5 Terawatts (TW) of energy and more than 80% of it is supplied by fossil fuels. Concerns over the security of these energy sources and climate effects of carbon emission have led to interest in renewable energy, such as wind, hydrothermal, and the most promising one: solar energy. Sunlight is abundant on the Earth's surface, even after being absorbed and reflected by the atmosphere. Average solar illumination at North American latitudes is 200 watts per square meter. Using 10% of the land in the US at 2% efficiency would produce 4 TW of energy, enough to meet our current energy needs.

By continuous wavelength (cw) illumination, bR can transform light energy into electrochemical energy stored in a proton gradient across a membrane and exhibit stationary photocurrent amplitude. Moreover, bR has exceptional stability to salt concentration, high temperatures, resistance to chemical and photochemical degradation,

and preserved functionality in a wide range of pH values.[88,89] These unique characteristics of bR could make it promising for applications in solar energy. Table 1-1 summarizes the relevant results from a partial literature survey on this aspect. Although there are some differences in bR film preparations, device configuration and experimental conditions, most photocurrent values are 0.2-40 pA cm^{-2} ML^{-1}.[90]

Table 1-1: Comparison of monolayer-level photocurrent response of dry bR, deduced from the results of bR monolayers or multilayers performed in different device configurations.[90]

Circuit (open/closed)	Film	Biased	Light trigger	Photovoltage, PV (photocurrent, I_{ph})[a]	Ref.
Al/bR/–/Au[c] (open)	Sub-ML[d]	Yes	CW $\lambda > 530$ nm 28 mW cm^{-2}	~10 mV ML^{-1} (No I_{ph} [e])	25
Al/bR/–/Au (open)	Sub-ML	Yes	CW $\lambda > 530$ nm 28 mW cm^{-2}	~4 mV ML^{-1} (No I_{ph})	26
ITO/bR/Al (closed)	~1 μm OF[f]	No	Xenon arc lamp ~1 mW cm^{-2}	No PV[g] (~3 pA cm^{-2} ML^{-1})	34
ITO/bR/–/Au (open)	4 μm OF	Yes	CW $\lambda = 635$ nm 2 mW cm^{-2}	~3 mV ML^{-1} (No I_{ph})	35
ITO/bR/–/BGO/ITO[h] (open)	10 μm OF	No	CW $\lambda = 532$ nm 500 μJ cm^{-2}	No PV (No I_{ph})	36
(gate of) GaAs FET (open)	100 μm OF	Yes	CW He-Ne laser 50 μJ cm^{-2}	No PV (~100 nA ML^{-1})	37
Al/bR/Au (closed)	ML	Yes	CW $\lambda > 530$ nm 28 μJ cm^{-2}	No PV (No I_{ph})	24
ITO/bR/Al (closed)	0.5 μm OF (in polymer)	Yes	CW $\lambda = 532$ nm 2 mW cm^{-2} + chopped $\lambda = 350$–600 nm	No PV (~40 pA cm^{-2} ML^{-1}) steady-state value	38
ITO/bR/Cu[b] (closed)	PVA[i] sol–gel (~100 μm)	Yes	Square wave of $\lambda = 532$ nm at 600 mW cm^{-2}	~0.2 mV ML^{-1} at 20 V external bias (~6 nA cm^{-2} ML^{-1})	39
ITO/bR/Al (closed)	0.5 μm OF (with polymer)	Yes	CW pump source 2 mW cm^{-2}, $\lambda = 405$ nm	(~40 pA cm^{-2} ML^{-1}) steady-state value	43
ITO/bR/Au/GaAs (closed)	PVA (~100 μm)	Yes	Laser, $\lambda = 632$ nm 800 mW cm^{-2}	(~0.2 pA cm^{-2} ML^{-1}) steady-state value	44
ITO/AM/bR/AM/InGa[j]	LBL[k]	No	Laser, $\lambda = 532$ nm	~ 15 mV ML^{-1} (No I_{ph})	42

[a] The values given are those calculated per monolayer, assuming that the photo-voltage/-current response of bR is linearly proportional to the number of bR monolayers, *i.e.*, the data are normalized in terms of the bR content in the multilayers. [b] Measurement taken under an external bias of 20 V. [c] /–/ = A gap in the circuit—open circuit measurement. [d] ML = monolayer. [e] I_{ph} = photocurrent. [f] OF = electric sedimentation oriented film. [g] PV = photovoltage. [h] BGO = bismuth germanium oxide. [i] PVA = poly(vinyl alcohol). [j] AM = apomembrane. [k] LBL = layer by layer with PDAC.

1.3 Thesis Focus and Organization

The rest of the thesis is structured as follows. In **Chapter 2**, the detailed preparations of bacteriorhodopsin and synthesis/characterization methods of metal nanoparticles are described. The bacteriorhodopsin preparation includes culture conditions, extraction, and purification steps of purple membrane. Gold/silver nanospheres, silver nanocubes, gold nanocages, and TiO_2 nanotube synthesis are described in this chapter. The analytical techniques used to image the samples by spectroscopic measurement and electron microscopy are also discussed.

Chapter 3 discusses the photocatalytic activity of gold nanocages with different sizes and morphology. In this work, it is shown that the silver oxide formation is the key to perform the photodegradation of methyl orange, which is one of the azo-dyes and is toxic to the environment. The degradation rate is found to be more efficient than photodegradation reaction using semiconductor nanomaterials, such as TiO_2 and ZnO. This is because the unique hollow interior of gold nanocages can form a "cage effect", meaning that the dye molecules could be caged by surrounding hydroxyl radicals and undergo a large number of collisions per unit time to enhance the reaction rate. The observed results on the rate are discussed in terms of 1) the surface area of the inner wall covered with Ag (Ag_2O), 2) the density and size of the pores in the walls, and 3) the cavity size of the nanoparticles.

The photothermal effect is when the plasmonic energy is converted rapidly into heat that raises the temperature of the medium. This mechanism is used widely in the biological and medical fields, with the most famous application being cancer therapy. **Chapter 4** discusses the first endeavor to apply the photothermal effect to catalysis. In the designed experiments, gold nanoparticles served not only as a catalyst but also as a heat source to increase the reaction solution temperature. The rate of the catalytic reaction between hexacyanoferrate (III) and thiosulfate on gold nanoparticles is found to increase when irradiated with light in resonance with surface plasmon absorption of the gold nanoparticles. To reveal the mechanism of the photothermal effect on the electron transfer reaction, the activation energy of the reaction via two different methods: photothermal effects of surface plasmon and by direct heating in a thermostat were compared. The two activation energies are found to be the same, suggesting that the plasmonic field effect in this electron transfer reaction is thermally induced and laser exposure does not change or damage the gold nanoparticles.

Bacteriorhodopsin can transfer light energy into electrochemical energy stored in a proton gradient across the membrane and it exhibits a stationary photocurrent

amplitude. This unique characteristic of bR could make it promising for applications in solar energy. However, the photocurrent density values reported so far are around 0.2-40 pA cm-^{2} in a thin film system. In **Chapter 5**, a solution-based electrochemical cell that did not require bR thin film preparation or external bias is discussed. A superior photocurrent generation in this solution-based photochemical cell is observed compared to the thin film systems. The details of cell design and various performance conditions are discussed in this chapter.

After an appropriate cell for solution-based bR work has been constructed, the next goal was to raise the photocurrent generation of bR. The conventional photocycle takes 15 milliseconds, but it can be shortened to 70 microseconds through the absorption of an intense blue light. In **Chapter 6**, the effects on bR of Ag, Ag-Au, and Au nanoparticles having different surface plasmon resonances were compared. From the results of the photocurrent measurement, the plasmonic enhanced photocurrent can be as high as 25 nA cm^{-3}, 15 times higher than that of pure bR. This value of photocurrent density is also orders of magnitude higher than previous reports. The mechanism of the by-passed photocycle formation is revealed by kinetic measurements.

In recent years, considerable efforts have been made to improve the performance of photoactive nanostructured materials for water splitting applications. In **Chapter 7**, the assembly and use of bacteriorhodopsin (bR)/TiO_2 nanotube arrays hybrid electrode system are reported. The results demonstrate the opportunity to fabricate fairly stable bR/TiO_2 hybrid electrodes that can be used as photoanodes for photoelectrochemical water splitting. Under AM 1.5 illumination (100 mW/cm^2) (a solar mimic), the hybrid electrodes achieved a 50% increase of photocurrent density compared to that measured for pure TiO_2 nanotubes. Assorted experiments have been done to prove that the unique proton pumping ability is the key to enhanced photocurrent. Multiple scans of bR/TiO_2 hybrid electrodes have also been performed to ensure long-term stability.

1.4 References

[1] Kreibig, U.; Vollmer, M. Optical Properties of Metal Clusters; Springer: Berlin, 1995.

[2] Schmid, G. Clusters and Colloids - From Theory to Applications; VCH: Weinheim, Germany, 1994

[3] Ghosh, S. K.; Kundu, S.; Mandal, M.; Pal, T. *Langmuir* **2002**, *18*, 8756.

[4] Ghosh, S. K.; Pal, T.; Kundu, S.; Nath, S.; Pal, T. *Chem. Phys. Lett.* **2004**, *395*, 366

[5] Ghosh, S. K.; Pal, A.; Kundu, S.; Nath, S.; Panigrahi, S.; Pal, T. *Chem. Phys. Lett*. 2005, 412, 5.

[6] Kubo, R. *J. Phys. Soc. Jpn.* **1962**, *17*, 975

[7] Jackson, J. D. *Classical Electrodynamics*; Wiley: New York, 1975; p 98.

[8] Freeston, I.; Meeks, N.; Sax, M.; Higgitt C. *Gold Bulletin* **2007**, *40*, 270.

[9] Barber, D. J.; Freestone, I. C. *Archaeometry* **1990**, *32*, 33.

[10] Faraday, M., *Philos. Trans. R. Soc. London, A* **1857,** 147, 145.

[11] Mie, G., *Annalen Der Physik* **1908,** 25, 377.

[12] Alvarez, M. M.; Khoury, J. T.; Schaaff, T. G.; Shafigullin, M. N.; Vezmar, I.; Whetten, R. L. *J. Phys. Chem. B* **1997**, *101*, 3706.

[13] Van Duyne, R. P. *Science* **2004**, *306*, 985.

[14] Haes, A. J.; Haynes, C. L.; McFarland, A. D.; Zou, S.; Schatz, G. C.; Van Duyne, R. P. *MRS Bull*. **2005**, *30*, 368.

[15] Kelly, K. L.; Coronado, E.; Zhao, L.; Schatz, G. C. *J. Phys. Chem. B* **2003**, *107*, 668.

[16] Moores, A.; Goettmann, F. *New J. of Chem*. **2006**, *30*, 1121.

[17] Jensen, T. R.; Malinsky, M. D.; Haynes, C. L.; Van Duyne, R. P., *J. Phys. Chem. B* **2000,** *104*, 10549.

[18] Link, S.; El-Sayed, M. A., *Int. Rev. Phys. Chem.* **2000,** *19*, 409.

[19] Haes, A. J.; Van Duyne, R. P., *J. Am. Chem. Soc.* **2002,** *124*, 10596.

[20] Turkevitch, J.; Stevenson, P. C.; Hillier, *Discuss. Faraday Soc*. **1951**, *11*, 55.

[21] Frens, G. *Nature: Phys. Sci.* **1973**, *241*, 20.

[22] Li, Y.; El-Sayed, M. A. *J. Phys. Chem. B*, **2001**, *105*, 8938.

[23] Tamura, M.; Fujihara, H., *J. Am. Chem. Soc.*, **2003**, *125*, 15742.

[24] Zhao, M.; Sun, L.; Crooks, R. M., *J. Am. Chem. Soc.* **1998**, *120*, 4877.

[25] Crooks, R. M.; Zhao, M.; Sun, L.; Chechik, V.; Yeung, L. K. *Acc. Chem. Res.* **2001**, *34*, 181.

[26] Mayer, A. B. R.; Hausner, S. H.; Mark, J. E. *Polym. J.* **2000**, *32*, 15.

[27] Teranishi, T.; Miyake, M. *Chem. Mat.*, **1998**, *10*, 594.

[28] Li, Y.; Boone, E.; El-Sayed, M. A. *Langmuir* **2002**, *18*, 4921.

[29] Narayanan, R.; El-Sayed, M. A. *J. Am. Chem. Soc.*, **2003**, *125*, 8340.

[30] Chen, C. W.; Akashi, M., *Langmuir*, **1997**, *13*, 6465.

[31] Adlim, M.; Abu Bakar, M.; Liew, K. Y.; Ismail, J., *J. Molec. Catal. A: Chem.*, **2004**, *212*, 141.

[32] Bonet, F.; Delmas, V.; Grugeon, S.; Herrera Urbina, R.; Silvert, P.-Y.; Tekaia-Elhsissen, K. *Nanostruct. Mater*. **2000**, *11*, 1277.

[33] Ahmadi, T. S.; Wang, Z. L.; Green, T. C.; Henglein, A.; El-Sayed, M. A. *Science*, **1996**, *272*, 1924.

[34] Narayanan, R.; El-Sayed, M. A. *J. Phys. Chem. B*, **2004**, *108*, 5726.

[35] Aiken, J. D., III; Finke, R. G. *J. Am. Chem. Soc.* **1999**, *121*, 8803.

[36] Michaelis, M.; Henglein, A. *J. Phys. Chem.* **1992**, *96*, 4719.

[37] Toshima, N.; Takahashi, T. *Bull. Chem. Soc. Jpn.* **1992**, *65*, 400.

[38] Fujimoto, T.; Mizukoshi, Y.; Oshima, R.; Nagata, Y.; Maeda, Y. *Trans. Mater. Res. Soc. Jpn*. **2000**, *25*, 95.

[39] Fujimoto, T.; Terauchi, S.; Umehara, H.; Kojima, I.; Henderson, W. *Chem. Mater*. **2001**, *13*, 1057.

[40] Esumi, K.; Tano, T.; Meguro, K. *Langmuir* **1989**, *5*, 268.

[41] Son, S. U.; Jang, Y.; Park, J.; Na, H. B.; Park, H. M.; Yun, H. J.; Lee, J.; Hyeon, T., *J. Am. Chem. Soc.*, **2004**, *126*, 5026.

[42] Giersig, M.; Mulvaney, P *Langmuir* **1993**, *9*, 3408.

[43] Brust, M.; Fink, J.; Bethell, D.; Schiffrin, D. J.; Kiely, C. J. *J. Chem. Soc., Chem.* **1995**, 1655-1656.

[44] Andres, R. P.; Bielefeld, J. D.; Henderson, J. I.; Janes, D. B.; Kolagunta, V. R.; Kubiak, C. P.; Mahoney, W. J.; O. R. G. *Science* **1996**, *273*, 1690.

[45] Templeton, A. C.; Hostetler, M. J.; Kraft, C. T.; Murray, R. W. *J. Am. Chem. Soc.* **1998**, *120*, 1906.

[46] Krenn, J. R.; Dereux, A.; Weeber, J. C.; Bourillot, E.; Lacroute, Y.; Coadonnet, J. P. *Phys. Rev. Lett.* **1999**, *82*, 2590.

[47] Elghanian, R.; Storhoff, J. J.; Mucic, R. C.; Letsinger, R. L.; Mirkin, C. A. *Science* **1997**, *277*, 1078

[48] Schatz, G. C. In *Surface Enhanced Raman Scattering*; Chang, R. K., Furtak, T. E., Eds.; Plenum: New York, 1982; p 35.

[49] Maier, S. A.; Kik, P. G.; Attwater, H. A. *Phys. Rev. B* **2003**, *67*, 205402.

[50] Biesso, A.; Qian, W.; El-Sayed, M. A. *J. Am. Chem. Soc.* **2008**, *130*, 3258.

[51] Huang, X.; Neretina, S.; El-Sayed, M. A. *Adv. Mater*. **2009**, *21*, 4880.

[52] Biesso, A.; Qian, W.; Huang, X.; El-Sayed, M. A. *J. Am. Chem. Soc.* **2009**, *131*, 2442.

[53] Ralph, A.; Sperling, P. R. G.; Zhang, F.; Zanella, M.; Parak, W. J. *Chem. Soc. Rev*. **2008**, *37*, 1896.

[54] Jain, P. K.; Huang, X.; El-Sayed, I. H.; El-Sayed, M. A. *Acc. Chem. Res.* **2008**, *41*, 1578.

[55] Huang, X.; Jain, P. K.; El-Sayed, M. A. *Lasers Med. Sci.* **2008**, *23*, 217.

[56] Huang, X.; Jain, P. K.; El-Sayed, I. H.; El-Sayed, M. A. *Photochem. Photobiol*. **2006**, *82*, 412.

[57] Huff, T. B.; Tong, L.; Zhao, Y.; Hansen, M. N.; Cheng, J. X.; Wei, A. *Nanomedicine* **2007**, *2*, 125.

[58] Hamad-Schifferli, K.; Schwartz, J. J.; Santos, A. T.; Zhang, S.; Jacobson, J. M. *Nature*, **2002**, *201*, 420.

[59] Angelatos, A. S.; Radt, B.; Caruso, F. *J. Phys. Chem. B* **2005**, *109*, 3071.

[60] Nel, A.; Xia, T.; Madler, L.; Li, N. *Science* **2006**, *311*, 622.

[61] Oesterhelt, D.; Stoeckenius, W. *Nature New Biol.* **1971**, *233*, 149.

[62] Oesterhelt, D.; Schuhmann, L. *Methods Enzymol* **1974**, *31*, 667.

[63] Oesterhelt, D.; Schuhmann, L. *FEBS Lett* **1974**, *44*. 262.

[64] Stoeckenius, W.; Bogomolni, R. A. *Annu. Rev. Biochem*. **1982**, *51*, 587.

[65] Korenbrot, J. I. *Ann. Rev. Physiol*. **1977**, *39*, 19.

[66] Mathies, R. A.; Lin, S. W.; Ames, J. B.; Pollard, W. T. *Ann. Rev. Biophys. Chem.* **1991**, *20*, 491.

[67] Lin, S.W.; Mathies, R. A. *Biophys. J.* **1989**, *56*, 653.

[68] Smith, O.S.; Pardoen, A. J.; Lugtenburg, J.; Mathies, R. *J. Phys. Chem*. **1987**, *91*, 804.

[69] Smith, O.S.; Braiman, M. S.; Myers, A. B.; Pardoen, A. J.; Courtin, J. M.; Winkel, C.; Lugtenburg, J.; Mathies, R. *J. Am. Chem. Soc*. **1987**, *109*, 3108.

[70] Balashov, S. P.; Imasheva, E. S.; Govindjee, R.; Sheves M.; Ebrey, T. G. *Biophys. J.* **1996**, *71*, 1973.

[71] Lanyi, J. K. *J. Phys. Chem. B* **2003**, *104*, 11441.

[72] Althaus, T.; Eisfeld, W.; Lohrmann, R.; Stockburger, M. *Isr. J. Chem*. **1995**, *35*, 227.

[73] Kandori, H. *Biochim. Biophys. Acta* **2000**, *1460*, 177.

[74] Herzfeld, J.; Tounge, B. *Biochim. Biophys. Acta* **2000**, *1460*, 95.

[75] Lanyi, J. K. *Biochim. Biophys. Acta* **2006**, *1757*, 1012.

[76] Birge, R. R.; Gillespie, N. B.; Izaguirre, E. W.; Kusnetzow, A.; Lawrence, A. F.; Singh, D.; Song, Q. W.; Schmidt, E.; Stuart, J. A.; Seetharaman, S.; Wise, K. J. *J. Phys. Chem. B* **1999**, *103*, 10746.

[77] Cao, Y.; Brown, L. S.; Sasaki, J.; Maeda, A.; Needleman, R.; Lanyi, J. K. *Biophys. J.* **1995**, *68*, 1518.

[78] Miller, A.; Oesterhelt, D. *Biochim. Biophys. Acta* **1990**, *1020*, 57.

[79] Neutze, R.; Pebay-Peyroula, E.; Edman, K.; Royant, A.; Navarro, J.; Landau, E. M. *Biochim. Biophys. Acta* **2002**, *1565*, 144.

[80] Lanyi, J. K. *Biochim. Biophys. Acta* **1993**, *1183*, 241.

[81] Zimányi, L.; Váró, G.; Chang, M.; Ni, B.; Needleman, R.; Lanyi, J.K. *Biochemistry* **1992**, *31*, 8535.

[82] Heberle, J. *Biochim. Biophys. Acta* **2000**, *1458*, 135.

[83] Lu, T.; Li, B. F.; Liang, L.; Rothe, U.; Bakowsky, U. *J. Chem. Soc. Faraday Trans* **1998**, *94*, 79.

[84] Nagy, K. Biochem. *Biophys. Res. Commun* **1978**, *85*, 383.

[85] Hampp, N. *Chem. Rev.* **2000**, *100*, 1755.

[86] Hessling, B.; Herbst, J.; Rammelsberg, R.; Gerwert, K. *Biophys. J.* **1997**, *73*, 2071.

[87] Lewis, A.; Albeck, Y.; Lange, Z.; Benchowski, J.; Weizman, G. *Science*, **1997**, *275*, 1462.

[88] Shen, Y.; Safinya, Liang, K. S.; Ruppert, A. F.; Rothschild, K. J. *Nature*, 1993, 366, 48.

[89] El-Sayed, M. A. *Acc. Chem. Res.* **1992**, *25*, 279.

[90] Jin, Y.; Honig, T.; Ron, I.; Friedman, N.; Sheves, M.; Cahen, D. *Chem. Soc. Re*v. **2008**, *37*, 2422.

CHAPTER 2

PREPARATION OF BACTERIORHODOPSIN AND SYNTHESIS OF PLASMONIC NANOMATERIALS

Abstract

The experimental details are described in this chapter, including the procedure used to prepare/purify bR and the synthesis protocol of nanomaterials (gold/silver nanospheres, silver nanocubes, gold nanocages, and TiO_2). The techniques for characterization of nanomaterials are also elucidated in this chapter.

2.1 Preparation of Bacteriorhodopsin

A standard procedure for growing bR by Oesterhelt *et al* published in 1974 is modified.[1]

Preparation of Growth Medium

The recipe for 1 liter of growth medium of *Halobacterium halobium* is:

2g	KCl
10g	$MgSO_4$
0.26g	$CaCl_2$
238g	NaCl
3.42g	Sodium citrate
10g	Oxoid L37 bacteriological peptone

The salts are dissolved in high purity D.I. water by use of a magnetic stirrer. The peptone is always added last, after the other salts have been dissolved. All media are autoclaved before inoculation.

Preparation of Cultures

A) New petri dish colonies are prepared by adding Bactro-Agar to the desired amount of culture medium. Autoclave, then pour into petri dishes while still hot and let them gel. To inoculate, sterilize a nichrome wire in a burner flame, and then dip it into a culture and streak the loop across the plate. The plate is placed in the lighted incubator until good-sized colonies are visible. The plate may then be stored until needed.

B) Initially, 5 mL of medium in a 50 mL flask is autoclaved for 60 min. After cooling to room temperature, the flask is inoculated by selecting a single colony from a petri dish and transferring it to the flask with a sterile scalpel. The flask is then put in a 37 ℃ incubator shaker. When the culture becomes turbid, it is ready to be used in the next step.

C) Autoclave 1 L of culture medium in a 2.5 L flask and inoculate with the 5 mL of culture from the last step. Place on the incubator shaker at 37 ℃ for about 5 days.

Purification of Bacteriorhodopsin

A) Fill centrifuge tubes with culture medium containing bacteria cell. Spin at 8,000 rpm at 4 ℃ for 10 min. Pour off the supernatant, but leave the pellet of cells at the bottom of the bottle. Refill the centrifuge tubes with culture medium, and repeat this process until the entire medium has been centrifuged.

B) Transfer the cells to a 500 mL flask using 4 M NaCl to clean out the centrifuge tubes. Add 3 mg of deoxyribonulease to the mixture. Stir mixture at room temperature overnight.

C) Load the cell suspension into dialysis tubes (membrane tubing, molecular weight cutoff: 12,000-14,000). Wet the tubing thoroughly, tie a knot in one end, and then pour in the suspension using a long-stem funnel. Tie off the other end, trying to minimize air bubbles.

D) Dialyze against 0.1 M NaCl for 2 days in the refrigerator. Change the NaCl solution after the first day of dialysis. The drop in salt concentration from 4 to 0.1 M will cause sufficient osmotic pressure inside the cells to rupture their membranes.

E) Collect the lysed cells and centrifuge the lysate at 19,000 rpm for 30 min at 4℃. Carefully pour off the supernatant and collect the pellets. Homogenize them (using tissue grinder) and divide the suspension into centrifuge tubes.

F) Spin again at 19,000 rpm for 30 min at 4 ℃. Repeat until the supernatant is clear. A slight pink color is also acceptable.

G) Collect the pellets and resuspend in D.I. water. Spin as above and repeat washing until supernatant is clear. The purity is determined by the ratio of intensity of the absorption at 280 nm and that at 568 nm. The value should be smaller than 1.8 to ensure the purity of sample (Figure 2-1).

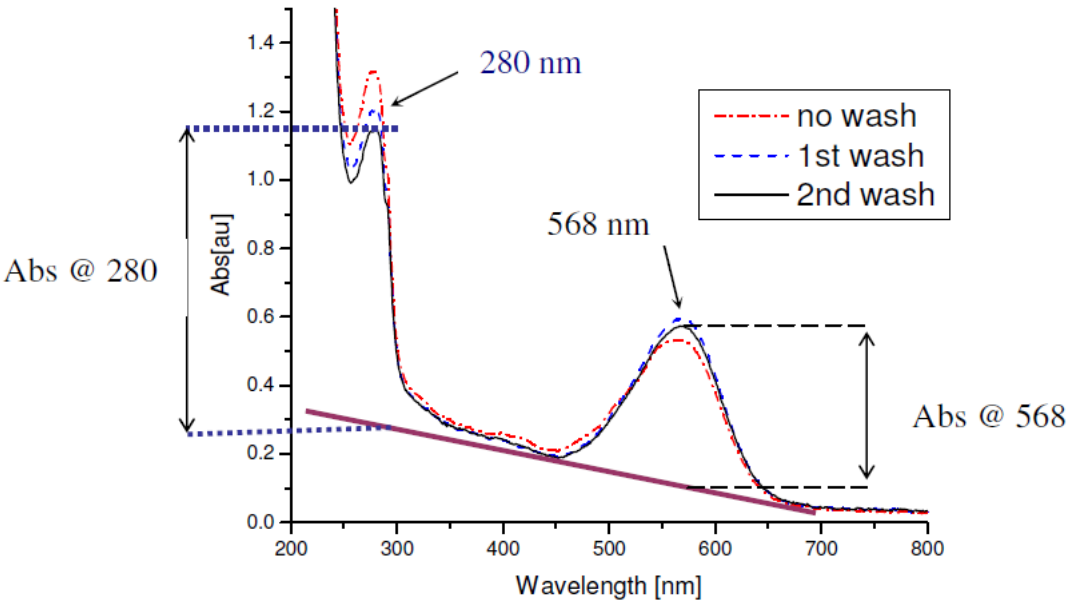

Figure 2-1: Absorption spectra of bR after two consecutive washes with D.I. water. *Figure adopted from Dr. Arianna Biesso's dissertation.

2.2 Synthesis of Nanomaterials

Synthesis of Gold/Silver Spheres

A modified version of the gold nanoparticle synthesis by Freund *et al* published in 1985 was used.[2,3] The 0.01% gold salt ($HAuCl_4$) and trisodium citrate solutions are made up in D.I. water. Generally, 25 mL of the $HAuCl_4$ was brought to boiling and 0.5 mL of the citrate solution of the appropriate concentration (Table 2-1) was added under continuous stirring. Boiling and stirring were continued for 20 min. The redshift of surface plasmon resonance peak can be observed with the increasing size of gold nanospheres (Figure 2-2). The solution was cooled in a bath at 25 ℃ and stored in a 25 mL volumetric flask. The colloids were indefinitely stable when stored at 5-10 ℃.

Table 2-1: Characteristics of citrate-stabilized gold nanospheres.[2]

colloid name	[citrate],[a] %	particles counted	r,[b] Å	β[c]
Z	2.00	66	77	1.12
A	1.00	184	82	1.13
B	0.70	173	113	1.21
C	0.50	155	175	1.26
D	0.35	165	312	1.41

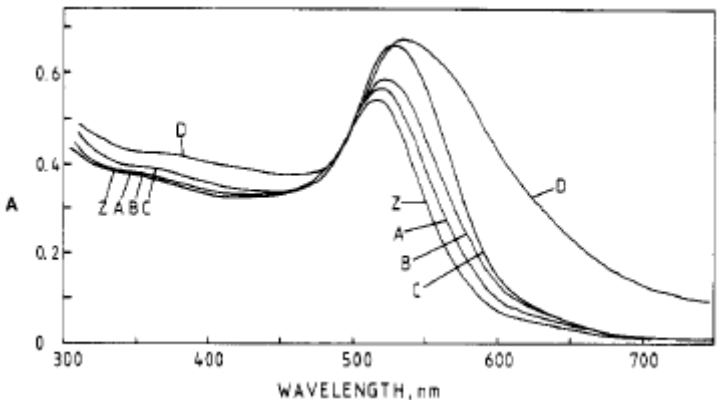

Figure 2-2: Absorption spectrum of gold nanosphers with various sizes.

The silver nanospheres are prepared by the same method, except for the silver nanospheres less than 10 nm in size. The small silver nanospheres were prepared by the following recipe:

A 100 mL solution of 0.25 mM $AgNO_3$ and 0.6 mM sodium citrate were mixed at room temperature for 20 min. Next, 0.5 mL of freshly prepared 50 mM $NaBH_4$ was added all at once with vigorous stirring and a distinct yellow color occurred immediately. The solution was continuously stirred for another 30 min for more stable nanoparticles.

Synthesis of Silver Nanocubes

The synthesis of silver nanocubes followed the method of Xia *et al*.[4] In this method, ethylene glycol serves as both solvent and reducing agent. A trace amount of Na_2S is added to catalyze the reduction of $AgNO_3$. The rapidly of the reduction effectively limits the formation of twinned Ag seeds, thus promoting silver nanocube formation. Moreover, the addition of polyvinyl pyrrolidone (PVP), which selectively binds to {100} silver facets, further facilitates the formation of a cubic shape.

An oil bath is heated to 150 ℃. Once a stable temperature is reached, 6 mL of ethylene glycol is pipetted into vial and placed in the oil bath for 1 h to remove any possible moisture. A cap is loosely placed on the top of vial to allow water vapor to escape.

Next, the PVP (M.W.=55,000), Na_2S and $AgNO_3$ solutions are added into the pre-heated ethylene glycol solution. A series of color changes should be observed: Trace purple, transparent bright yellow (within 1 min), yellow-orange (within 2-3 min), and opaque ruby (within 7-10 min) (Figure 2-3). Larger silver nanocubes can be prepared by increasing the heating time. To quench the reaction, remove the reaction vials from the heated oil bath and place them in a water bath held at room temperature.

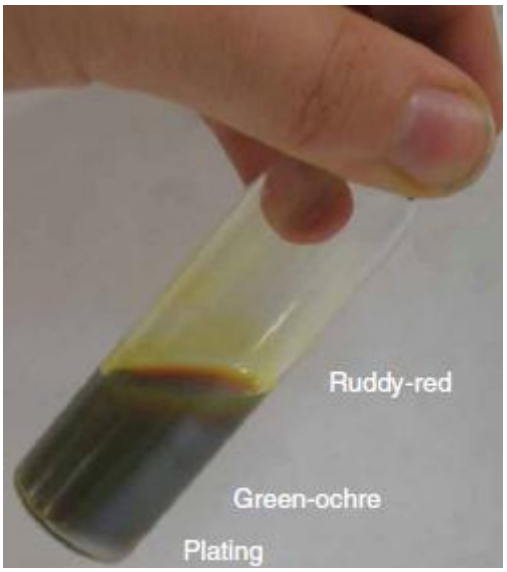

Figure 2-3: Photograph of silver nanocubes. The reaction media of as-synthesized silver nanocubes appears ruby-red when viewed from the top.

Once the reaction vials have cooled, transfer the contents are transferred into centrifuge tubes. Each vial is rinsed with acetone and the product is spun down at 2,000 *g* for 20-30 min. The supernatant is discarded and D.I. water is added to each centrifuge tube. The particles are washed and centrifuged at 9,000 *g* for 10 min twice. The silver nanocubes are stored in D.I. water and ready for use (Figure 2-4).

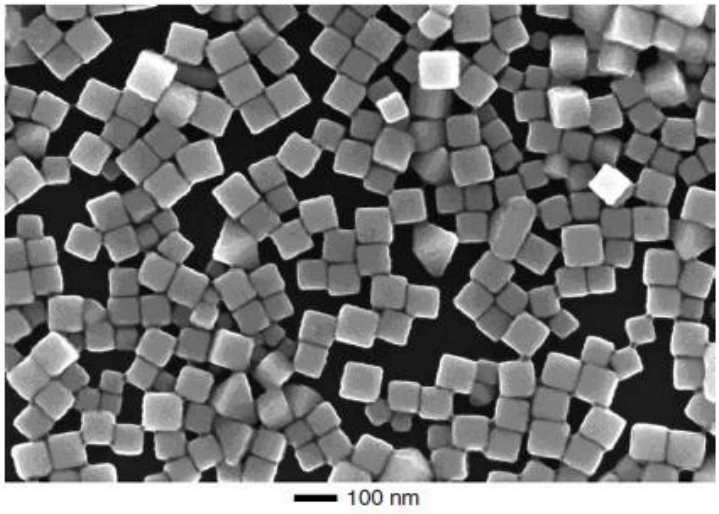

Figure 2-4: Scanning electron microscope image of silver nanocube.

Synthesis of Gold Nanocages

The prepared silver nanocubes can be used as sacrificial templates to prepare hollow and porous gold nanocages via a galvanic replacement reaction. An illustration of the galvanic replacement reaction between silver nanocubes and a $HAuCl_4$ solution is shown in Figure 2-5. The replacement reaction is initiated at the cube surface of highest energy and then continues to form a partially hollow, homogeneous wall composed of an Au/Ag alloy. After box formation, the continued addition of $HAuCl_4$ solution facilitates dealloying and corner reconstruction of the Au/Ag nanobox to form porous gold nanocages. With further addition of $HAuCl_4$, gold nanoframes can be formed.

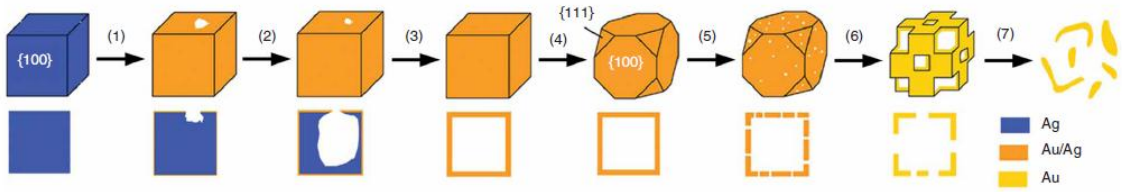

Figure 2-5: Mechanism of gold nanocage formation. The addition of $HAuCl_4$ can greatly affect the morphology of gold nanocages.

First, a 10 mL of 9 mM PVP (M.W.=55,000) and 10 mL of 0.1 mM $HAuCl_4$ in D.I. water are prepared. Next, 5 mL of the PVP solution is added to a round bottom flask followed by 100 uL of the as-synthesized silver nanocubes. The solution is heated to a mild boil and then the $HAuCl_4$ solution is added into the reaction flask. As the $HAuCl_4$ solution is added to the reaction flask, a series of color changes will be observed, which can be used to estimate the position of the surface plasmon resonance peak of gold nanocages (Figure 2-6). The gold nanocages are isolated by centrifugation, followed by decantation twice (Figure 2-7).

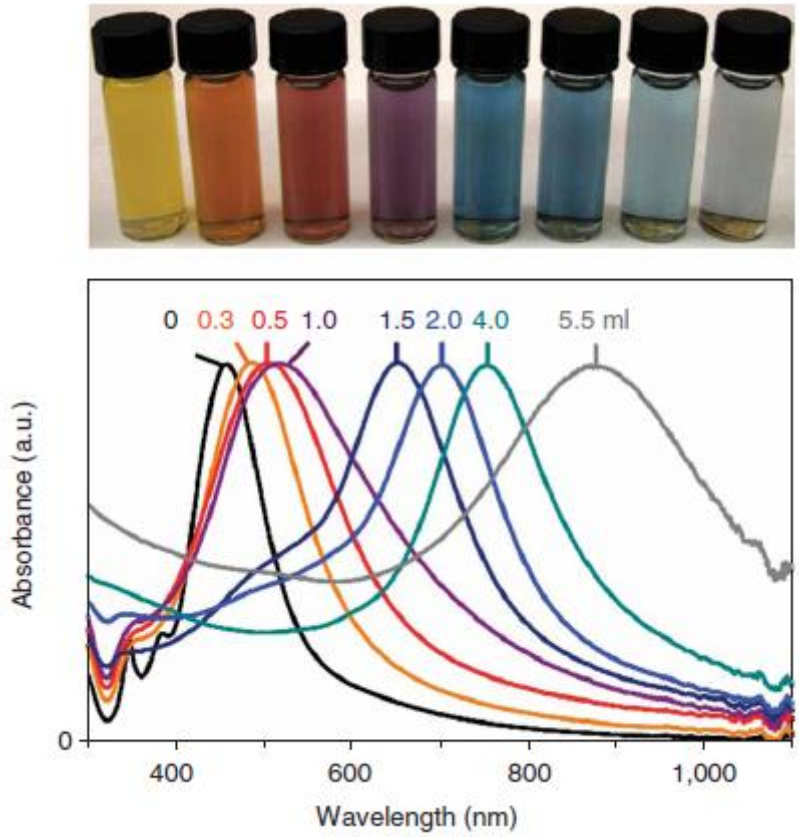

Figure 2-6: (Top) Vials containing gold nanocages prepared with the different volumes of $HAuCl_4$ solution added. From left to right, 0, 0.3, 0.5, 1.0, 1.5, 2.0, 4.0 and 5.5 mL. (Bottom) The corresponding UV-visible absorbance spectrum of the gold nanocages. The SPR peak of the gold nanocages is tunable throughout the visible to near-IR regions by varying the volume of $HAuCl_4$ solution added.

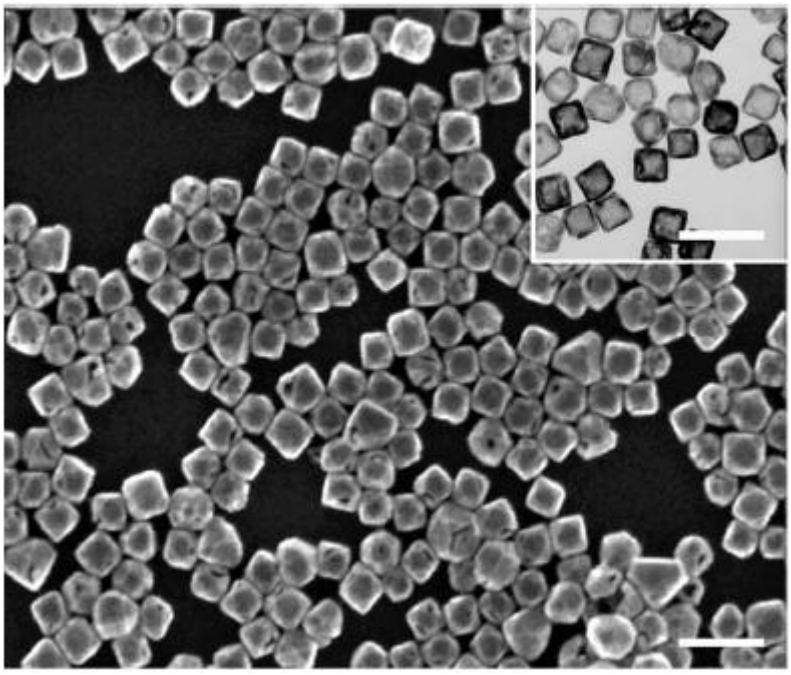

Figure 2-7: A scanning electron microscope image of gold nanocages (scale bars are 100 nm for both images.)

Synthesis of TiO_2 Nanotubes

Pure titanium foil is ultrasonically cleaned with acetone then rinsed with D.I. water. The anodization was performed in a two-electrode electrochemical cell with titanium foil as the working electrode and platinum foil as the counter electrode under constant applied voltage at room temperature in chloride containing electrolytes (Figure 2-8). A DC power supply was used for the potentiostatic anodization. After anodization, the samples were rinsed thoroughly with D.I. water and then dried with pure nitrogen.

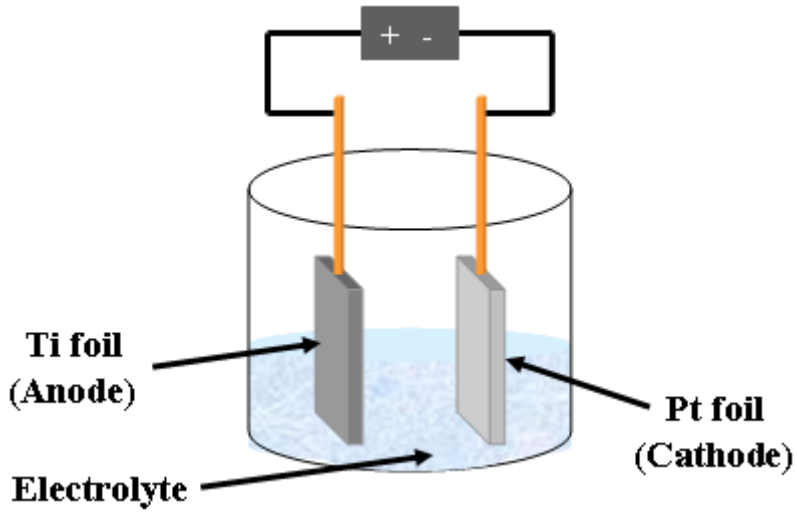

Figure 2-8: Schematic of the anoization set up for TiO_2 nanotube preparation

2.3 Other Instrumentation used in this Dissertation

Electron and Surface Probe Microscopes

The nanomaterials were imaged using several microscopy methods. The formed morphology of nanomaterials was analyzed by scanning electron microscopy (LEO 1530 Thermally-Assisted Field Emission SEM, Zeiss/LEO). All images were taken using a secondary electron detector and an accelerating voltage from 1-10 kV.

The transmission electron microscope (TEM) images were obtained using a JEOL 100CX-2 TEM. The TEM images provide information on the structure and size distribution of nanomaterials. The TEM grids used for imaging are coated copper grids purchased from Ted Pella.

Absorption Spectroscopy

The UV-visible extinction spectroscopy of nanomaterials was performed using Oceanoptics (DH 2000). The Raman experiments were performed on a Kaiser Optical System coupled to an Olympus microscope. The excitation wavelength was 785 nm and

the power was tunable from 10-35 0mW. The signal collection was taken at 180° through a chilled CCD camera.

2.4 References

[1] Oesterhelt, D.; Schuhmann, L. *Methods Enzymol.* **1974**, *31*, 667.

[2] Freund, P. L.; Spiro, M. *J. Phys. Chem.* **1985**, *89*, 1074.

[3] Turkevich, J.; Stevenson, P. C.; Hiller, J. *Discuss. Faraday Soc.* **1951**, *11*, 55.

[4] Skrabalak, S. E.; Au, L.; Li, X.; Xia, Y. *Nature Protocols* **2007**, *2*, 2182.

CHAPTER 3

PHOTOCATALYSIS IN GOLD NANOCAGE NANOREACTORS

Abstract

The photo-degradation of methyl orange was found to take place very efficiently using hollow Au nanocages which are known to have remaining Ag on their interior walls which can be oxidized to Ag_2O. The degradation rate is found to be more efficient than photodegradation reaction using semiconductor nanomaterials, such as TiO_2 and ZnO. The reaction rate is found to increase by increasing the degree of Ag oxidation on the interior wall of the nanocages prior to the reaction and is a function of the nanocavity size and the pore density of the nanocage walls. As the cage size varies, it is found that the photocatalytic rate increases then decreases with a maximum rate at a nanoparticle size of 75 nm with a medium pore density in the walls. All these results suggest that the catalysis is occurring inside the cavity, whose interior walls are covered with the Ag_2O catalysts. Similar to the mechanism proposed in the degradation by the other semiconductors, we propose that the photo-degradation mechanism involves the formation of the hydroxyl radical resulting from the photo-excitation of the Ag_2O semiconductor. The observed results on the rate are discussed in terms of 1) the surface area of the inner wall covered with Ag (Ag_2O), 2) the density and size of the pores in the walls, and 3) the cavity size of the nanoparticles.

3.1 Introduction

Nanomaterials with hollow structure are promising, due to their unique optical and catalytical properties.[1-7] Due to the larger surface to volume ratios; they are expected to be more effective in catalysis. Gold nanocages were first synthesized by Xia and et al.[8] They have developed a facile way to synthesize nanoparticles of uniform shape and size with hollow interiors and have demonstrated that hollow nanocages have high catalytic activity, similar to Pd nanotubes for Suzuki coupling reaction[9] and Pd-Au-Ag nanocages for methyl red hydrogenation.[10] Hollow gold nanocages that are very stable and have a novel layered structure have never been used as a novel photocatalyst.[11] In this work we used them in the photodegradation of methyl orange (MO) dye and found them to be more efficient than TiO_2[12-14] and ZnO[15] in the photodegradation of azo dyes.

The most common reported photocatalyst for the photocatalytic oxidative degradation of azo-dyes is semiconductor materials, such as TiO_2[12-14] and ZnO[15]. The basic photocatalytic principle of semiconductor materials (usually metal oxides) is photogenerated electrons (from the conduction band) and holes (from the valance band) migrating to the metal oxide surface and reacting with adsorbed O_2/H_2O to generate reactive radicals which can attack the azo-dyes and lead to their photodegradation.[12]

The method of galvanic replacement transform the silver nanocubes into gold nanocube shells with pores in the walls whose number increases with the nanocube shell size and their inside wall are coated with the remaining silver. In the present work, we examine the effect of cavity size on the rate of the photodegradation of the methyl orange dye by using the Ag walls of the Au nanocavity. It is known that silver is easily oxidized to silver oxide solution even at 300 K and the formation of silver oxide (Ag_2O) is extremely stable in ambient condition.[16] The reported band gap of silver oxides is $\sim$2.5 eV (400 nm-500 nm) and it can therefore be an analogous to the other semiconductor materials.[17] Upon the absorption of the light energy, it produces radicals that could perform oxidative degradation of MO.

We prepared gold nanocages of various sizes and different cavity volumes to serve as nanoreactors. The photodegradation reaction of MO demonstrates that the oxygen treatment is the key point for nonreactors to become a good photocatalyst for this reaction. We found that the catalytic activity increases then decreases as the nanocavity becomes larger. This is explained by the fact that increasing the cavity size first increases then decreases the cavity surface area. The smaller surface area at the large cavity proposed to result from the increase in its surface pores.

3.2 Experimental Section

Gold nanocages (AuNCs) of various sizes and wall thickness were prepared from silver nanocube template nanoparticles via the galvanic replacement method.[18] Silver nanocubes (AgNCs) were prepared by heating 30 mL of ethylene glycol (EG) at 150 ℃ for 1 hour, followed by the addition of 0.2 g of polyvinyl pyrrolidone (PVP, MW 55k) dissolved in 10 mL EG. The resulting solution was heated until the temperature reached 150 ℃. A solution of 0.4 mL sodium sulfide dissolved in ethylene glycol (3 mM) was added. Three sizes of AgNCs were prepared (50, 75, and 100 nm) by slowly injecting various amounts of silver nitrate (2.5, 3, and 3.5 ml of 282 mM dissolved in EG, respectively) into the reaction mixture. The silver ions were reduced completely after 15 minutes, producing AgNCs. Diluting 10 mL of AgNC solution with acetone and subsequently centrifuging purified the AgNCs. The particles were then re-dispersed in deionized water. The solution of purified AgNCs was brought to a boil and a 10 mg/L solution of hydrogen tetrachloroaurate was injected slowly. This mixture was continuously refluxed until its color remained constant. Vigorous magnetic stirring was maintained throughout the synthesis. The thickness and porosity of the AuNC's walls were controlled by the amount of gold salt added to the solution.[19] Eight individual colloidal solutions of AuNCs were prepared from the three sizes of AgNCs (50nm, 75nm, and 100 nm). From the 50nm AgNCs, three AuNC samples were synthesized of different

wall thickness (samples I, II, and III). From the 75 nm AgNCs, three AuNC samples were synthesized of different wall thickness (samples IV, V and VI), and from the 100 nm AgNCs, two samples were synthesized of different wall thickness (samples VII and VIII). As the shape of the nanocages was varied through additional $AuCl_4^-$, the surface plasmon resonance was red-shifted, due to the further loss of silver atoms in the alloy structure. Oxygen treatment of the AuNCs was performed prior to the photocatalysis experiments. An aliquot of 50 mL of the AuNC solution was stirred in the cylinder and oxygen gas was bubbled through the solution at a rate of 30 mL/min for six hours to oxidize the silver atoms of the AuNCs to silver oxide (Ag_2O). The photocatalysis reactions were carried out in a quartz cell containing the reaction mixture irradiated by a 50W high-pressure Xe-Hg lamp. The reaction temperature was held constant at room temperature to reduce thermal effects on the catalytic rate. The reaction mixture was composed of 2 mL of the nanocube solution and 200 μL of methyl orange (MO) (20 mg/L). Optical measurement of the characteristic peak of MO (~480 nm) was used to monitor the changes in the concentration of the MO reactant during the photocatalytic experiments. All optical measurements were collected using an Ocean optics UV-Vis spectrometer HR4000Cg-UV-NIR.

The 50 nm AuNCs with surface plasmon peaks at 650, 700, and 800 nm had optical densities (ODs) of 1.5, 2.6, and 2, respectively. The 75 nm AuNCs had ODs of 1.8, 2.3, and 2, respectively. The 100 nm AuNCs with plasmon peaks at 700 and 800 nm had ODs of 1.5 and 1.4 respectively. A Holoprobe Raman microscope (Kaiser Optical Systems) with 785 nm laser excitation was used for Raman measurements.

3.3 Results and Discussions

Preparation of Silver Nanocages

To prepare various sizes of AuNCs, one must synthesize AgNCs first for use as a sacrificial template during the galvanic replacement reaction. Here, three different sizes of AgNCs were prepared (50, 75, and 100 nm). The synthetic approach of AuNCs is based on the galvanic replacement reaction between AgNCs and the gold salt solution. The gold ions are reduced at the expense of silver atoms that compose the nanocubes, which are oxidized via the following equation:[19]

$$3Ag_{(s)} + AuCl_{4\,(aq)}^{-} \rightarrow Au_{(s)} + 3Ag_{(aq)}^{+} + 4Cl_{(aq)}^{-} \qquad (1)$$

The first stage of this synthesis is a solid silver-gold alloy wall formed when a relatively small amount of gold salt is added to the template solution. Their box-like and solid Au/Ag alloy wall characterizes the particles in this stage and the SEM images show the uniformity and closed wall structures (See Figure 3-1 I, IV, and VII).[18-20] In the later stage of synthesis, as more gold salt is added to the box-like AuNC solutions, some silver atoms undergo a de-alloying process from the Au/Ag alloy walls. Numerous pores within the walls are formed by selectively extracting silver atoms and porous AuNCs are generated from the box-like AuNCs. The continuous etching of the silver core leads to an increase in the void size and causes the SPR peak to red-shift compared to the corresponding solid box-like AuNC structure (Figure 3-2). In the final stage of synthesis, when the amount of gold salt added to the porous AuNCs was further increased, Au atoms were simultaneously reduced, inducing changes in the porosity. According to equation (1), one gold cation (Au^{3+}) is reduced by three silver atoms, thus resulting in a continuous etching of the silver core producing nearly an empty AuNC (Figure 3-1 III and VI). Because of the loss of the silver atoms, AuNCs in the final stages were transformed into frame-like AuNCs producing vacant cavities of AuNCs. By increasing

the pore sizes in the walls and thinning the wall thickness caused a shift in the SPR peak of the frame-like AuNCs from the visible to the near-IR range (800 nm, Figure 3-2A, B). In summary, the synthetic steps based on galvanic replacement are a simple and versatile method to make gold nanostructures with a specific porosity of the wall, a precise volume of the cavity, and a desired position of the SPR band.[18-20]

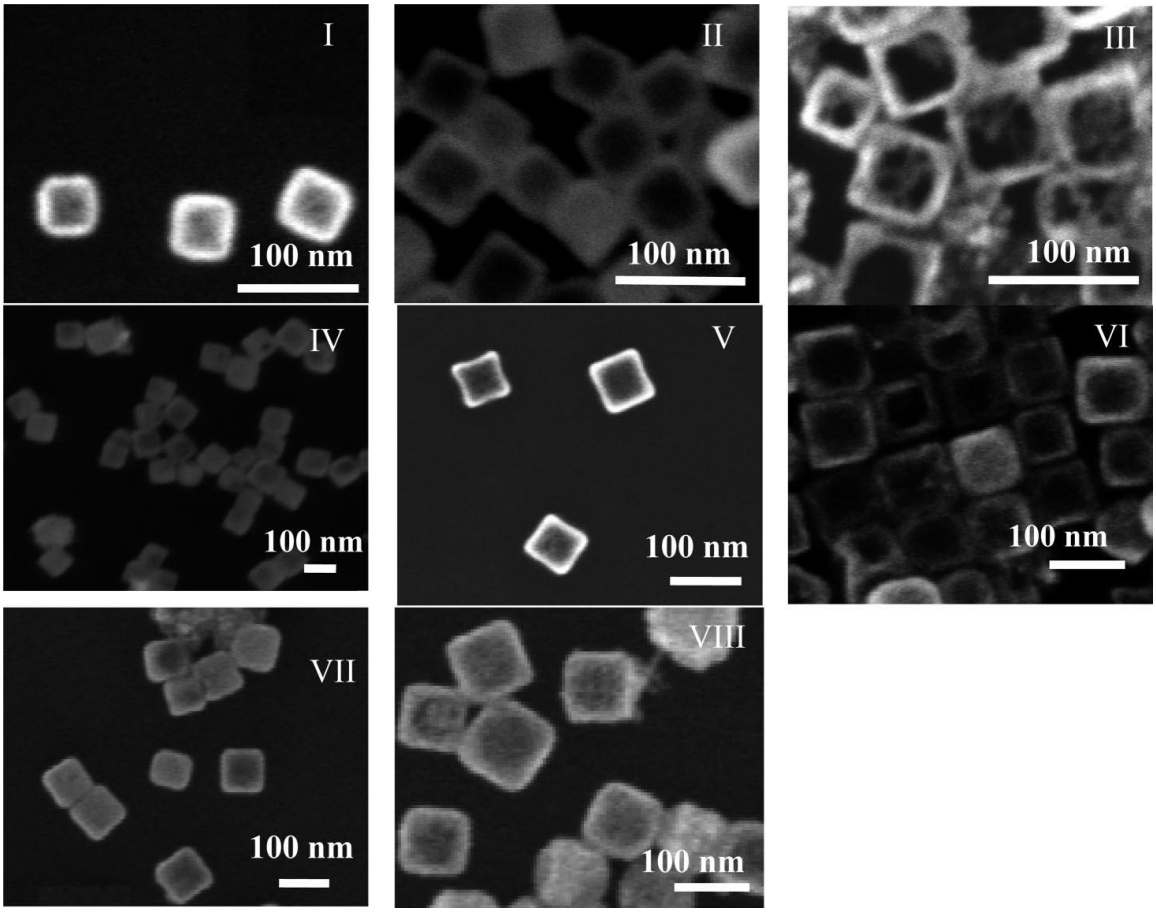

Figure 3-1: SEM images of AuNC samples. I, II, and III are the 50 nm AuNCs. IV, V, and VI are the 75 nm AuNC samples. VII and VIII are the 100 nm AuNC samples. I, IV, and VII are the boxlike AuNCs. II, V, and VIII are the porous AuNCs. III and VI are the framelike AuNCs.

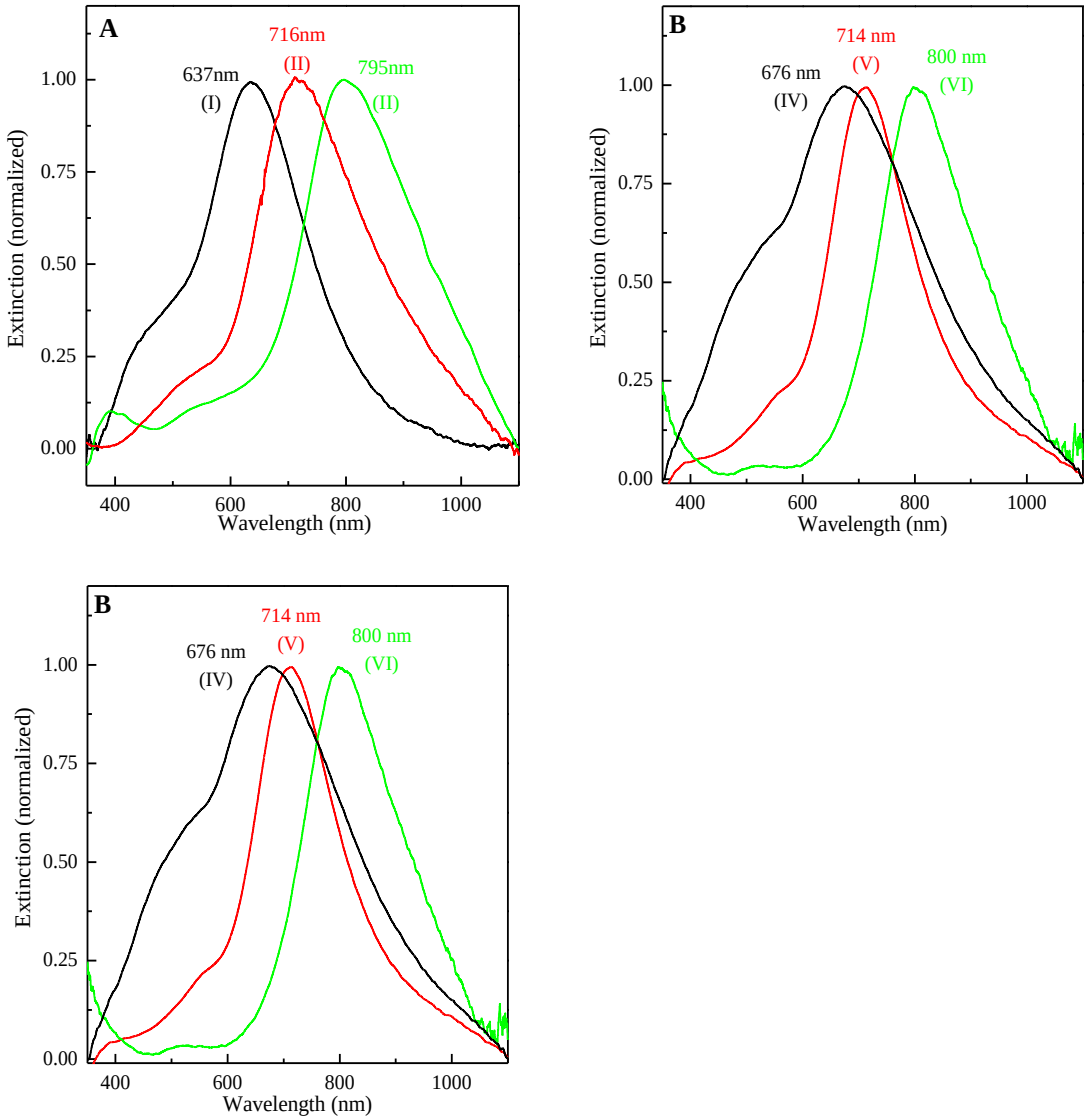

Figure 3-2: Normalized SPR extinction spectra of (A) 50 nm size AuNCs, (B) 75 nm size AuNCs, and (C) 100 nm size AuNCs. By varying the volume of HAuCl4 solution added to the AgNCs, the SPR band of the AuNCs was tuned from the visible to the near-IR region due to changes in porosity and volume of the cavity of the particles. The particles are divided into three groups: (1) poreless Au/Ag alloy walls, boxlike AuNCs (samples I, IV, and VII), (2) enlarged pores in the Au/Ag alloy walls, porous AuNCs (samples II, V, and VIII), and (3) nearly empty interiors, framelike AuNCs (samples III and VI).

Characterization of Silver Oxide Formation

To activate the AuNCs as photocatalysts, the remaining silver atoms on the inside walls of the cavity of the AuNCs were oxidized into silver oxides (Ag_2O). The silver oxide is capable of adsorbing the energy from light at a frequency between 400-500 nm to produce radicals that perform oxidative degradation of azo-dyes. Silver atoms can be efficiently converted into silver oxides upon oxygen treatment by bubbling oxygen gas into the solution. The oxidation of silver into silver oxide by oxygen gas is thermodynamically and electrochemically allowed at room temperature.[16, 21] Oxygen gas oxidizes silver atoms according to the following equation:

$$4Ag + 2H_2O \rightarrow 2Ag_2O + 4H^+ + 4e^- \qquad E^o = -1.173\,V$$
$$O_2 + 4H^+ + 4e^- \rightarrow 2H_2O \qquad E^o = +1.229\,V$$
$$4Ag + O_2 \rightarrow 2Ag_2O \qquad \Delta E = +0.056\,V$$

Figure 3-3A shows the surface plasmon spectra of AuNCs before and after oxygen treatment. The surface plasmon resonance red-shifts upon oxidation, which is in agreement with the results of other groups. [22-24] In addition, the comparison of the Raman spectra of the fresh and oxygen-treated AuNCs shows a large increase in the silver oxide (Ag_2O) peak at 525 cm^{-1} in oxygen-treated samples (Figure 3B). [25-26]

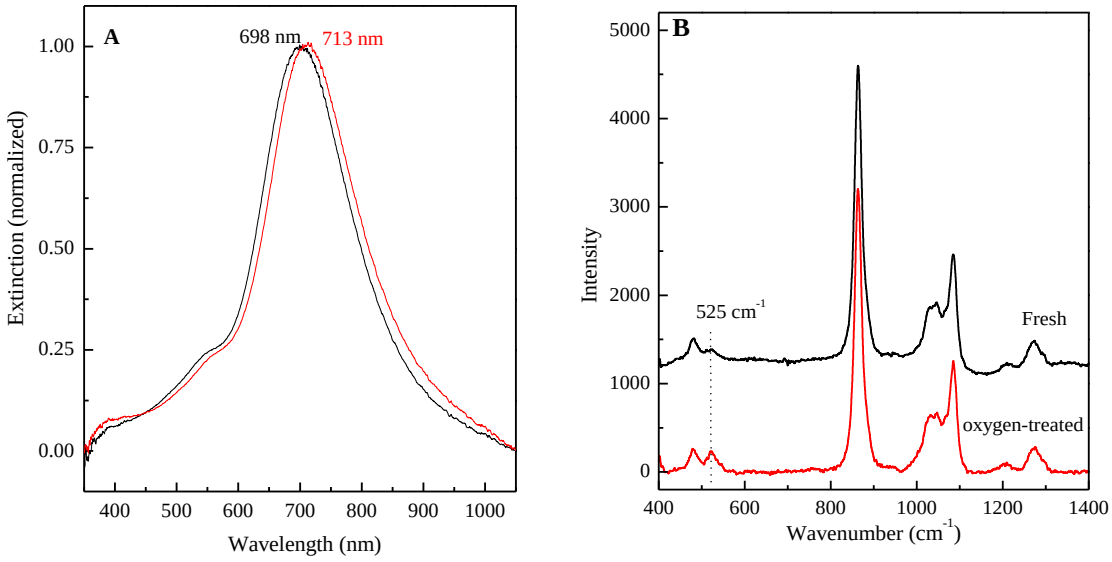

Figure 3-3: (A) Surface plasmon resonance spectra of 75 nm AuNCs before (black) and after (red) treatment with oxygen gas. (B) Raman spectrum of AuNCs before (black) and after (red) oxygen treatment. Shift in surface plasmon spectrum and the increases in intensity of the 525 cm^{-1} Ag_2O Raman band both support the formation of Ag_2O by oxygen treatment

Photocatalytic Ability of Silver Nanocages

Different Treatment Step

In order to test the active source of the Ag dependent photoreduction (Ag or AgOx), we treated three colloidal solutions of nano-cages (originally from the same batch) in the following manner: (1) as-synthesized (no-treatment), (2) aged for one month, and (3) oxygen purged. The data from UV-vis and Raman spectroscopy gave us powerful evidence of silver oxide formation in the oxygen-purged and one-month-old nanocages.

The change in MO concentration was quantitatively monitored during the reaction by monitoring the optical absorption peak intensity located around 480 nm. This peak is sensitive to the changes in pH of the medium and red-shifts with decreasing pH. In the absence of the photocatalyst, the MO itself is stable for several hours upon irradiation

with the Xe-Hg lamp (data not shown). Therefore, the observed rapid decrease of the MO absorbance peak in the presence of AuNCs results from the catalyzed photo-degradation. The absorbance intensity at 480 nm of MO is measured in intervals of ten minutes and the reaction rate was obtained by calculating the absorbance change of MO as a function of time.

The AuNCs performed well as photocatalytic degradation on the MO agents after being activated through oxygen treatment. Prior to oxygen treatment, the AuNCs lacked photocatalytic activity in the catalytic degradation of MO. The photodegradation reaction of MO demonstrated that the oxygen treatment is the key point for nanocages to form a good photocatalyst; the photoactivity will be largely affected by the silver oxide formation (Figure 3-4) and both of these two samples showed much better reaction rates (Table 3-1).

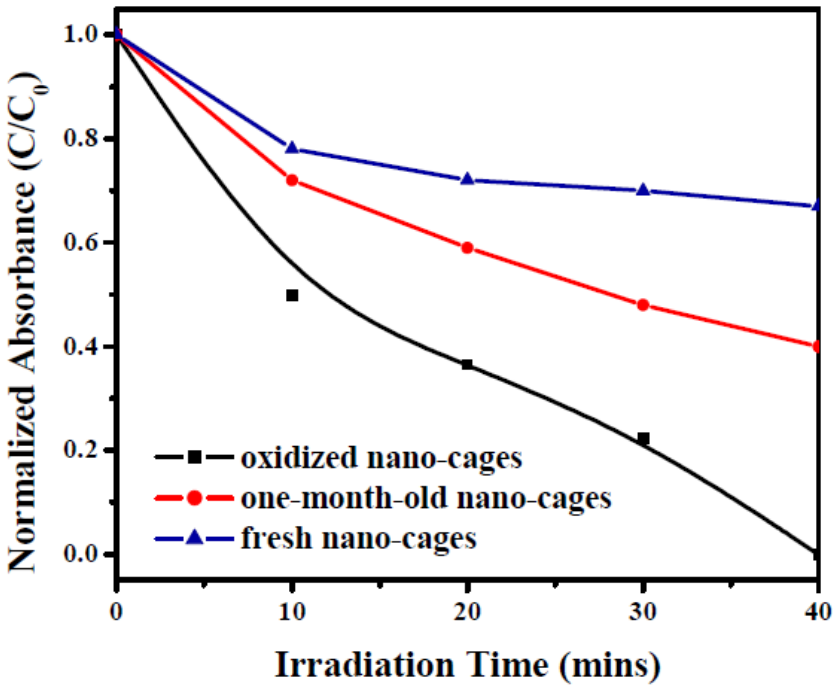

Figure 3-4: Photocatalytic activities of Au-Ag nanocages with different treatments.

Generally, AuNCs exhibit a much higher photocatalytic activity compared to TiO_2 (Table 3-1) under superior reaction conditions (higher MO concentration, less catalysts amount and weaker lamp intensity). However, the high photocatalytic ability of the AuNCs is not solely due to the silver oxides. The unique hollow interior of the AuNCs increases the contact between the active catalyst sites and the reactants. To verify the significance of the hollow cavity in AuNCs, we prepared the particles of commercial bought silver oxide and the silver oxide nanoparticles by citrated acid reduction. The activity of AuNCs was compared to those of the two silver oxides solutions without hollow interiors, and AuNCs were found to have a much higher reaction rate of MO decolorization compared with the two silver oxide particles (Figure 3-5). The results suggest that the unique structure of the AuNCs serves as a good nano-reactor to confine the reactants inside the particles' cavity, resulting in an enhancement of their photocatalytic activity.

Table 3-1: Comparison of reaction rate over different catalysts

Catalysts	**λ max (nm)**	**Au/Ag ratio***	**k (min^{-1})**	**MO concentration**	**Catalysts Concentration**
NC	703	1/3.5	0.40	20mg/L	0.07g/100ml
NC	785	1/1	0.08	20mg/L	0.07g/100ml
NC(O_2-purged)	848	2/1	0.04	20mg/L	0.07g/100ml
NC (one-month)	847		0.02	20mg/L	0.07g/100ml
NC(as-synthesized)	810		0.01	20mg/L	0.07g/100ml
Ag@citrate acid			0.02	20mg/L	0.15g/100ml
Ag_2O powder			0.02	20mg/L	0.25g/100ml
Anatase TiO_2			0.04	10mg/L	0.3g/100ml
3 wt %Ag/Bi_3O_4Cl			0.09	10mg/L	0.3g/100ml

*determined by ICP-mass

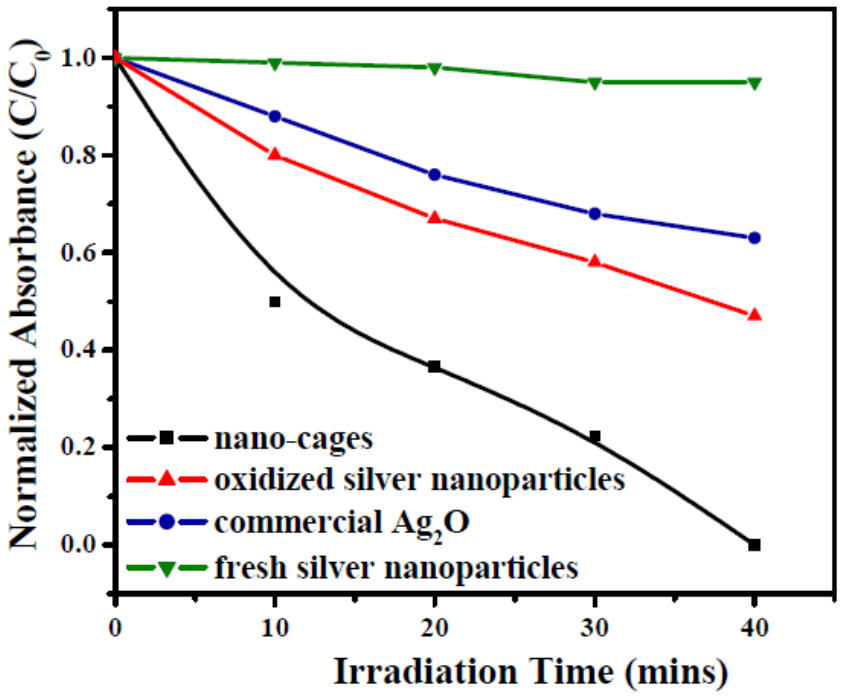

Figure 3-5: Photocatalytic activities of AuNCs, commercial Ag_2O, Ag@citrate acid before and after oxygen treatment

Size and Structure

The photocatalytic activity of three different sizes of AuNCs (50, 75, and 100 nm) having the same SPR band position (around 700 nm) under the same conditions were compared. During the sixty minutes photocatalytic reactions, the photo-degradation process of MO was almost complete when catalyzed by 75 nm-AuNCs (Figure 3-6B). However, thirty and sixty percent of the MO remained when the degradation catalysis was carried out by the 50 nm and 100 nm AuNCs, respectively (Figure 3-6A and C). All eight AuNCs samples synthesized here were used as photocatalysts and their activities were studied. The reaction rates of these eight catalysts all obeyed first-order kinetics as shown in A, B and C of Figure 3-7. The time-dependent extinction spectra of MO catalyzed by three samples are shown in Figure 3-6.

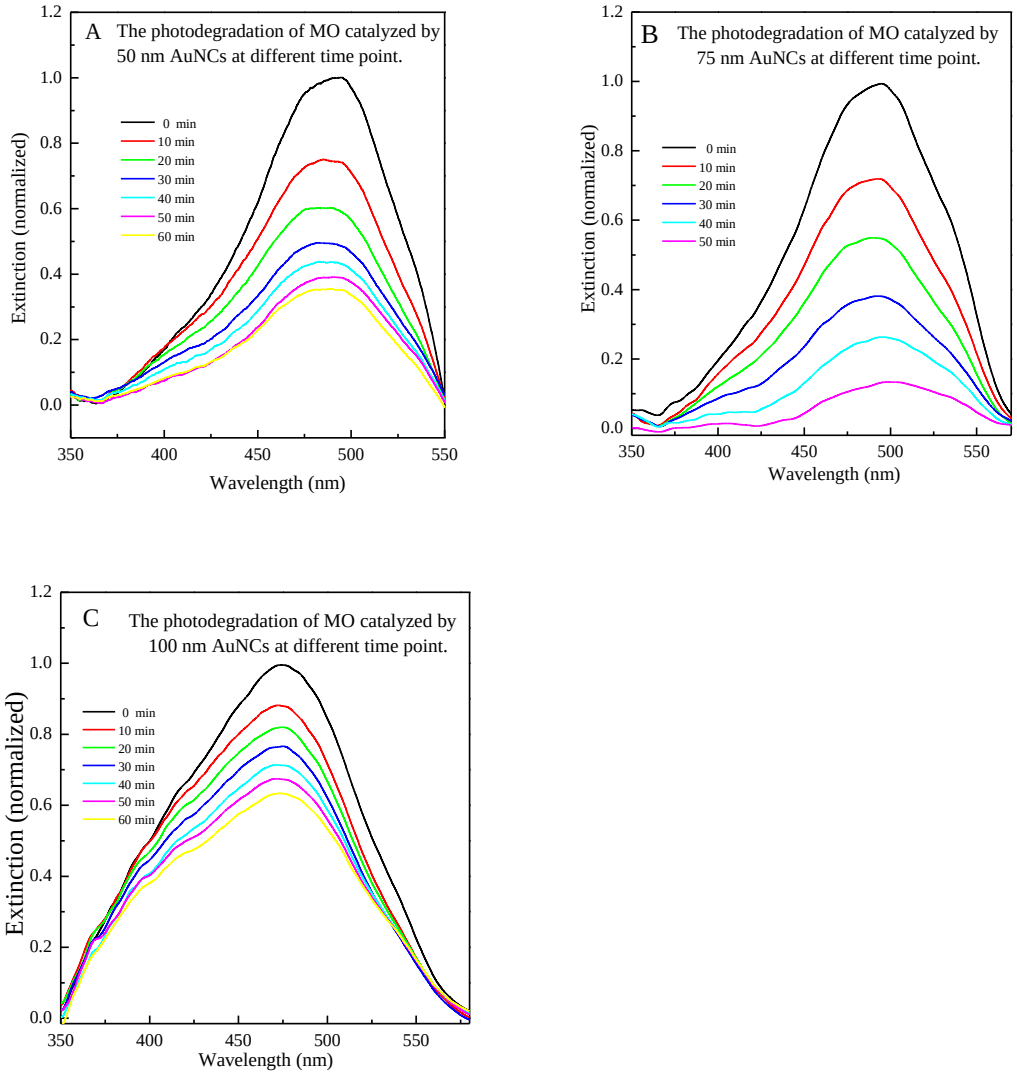

Figure 3-6: Time-dependent extinction spectra of methyl orange catalyzed by AuNCs with similar SPR bands at 700 nm but of different sizes: (A) 50 nm (sample II), (B) 75 nm (sample V), and (C) 100 nm (sample VII). The photodegradation experiment took 1 h, and absorbance of MO was measured every 10 min. All three experiments were performed under the same conditions.

The photocatalytic ability of AuNCs and solid AgNCs were compared. There is no hollow cavity inside the AgNCs because they are solid nanostructures. For AgNCs (fresh and oxygen treated ones), the photocatalytic activity was significantly non-existent,

as indicated by no measurable change in the MO absorption peak during the reaction. Although the absorption peak of MO and the SPR band of pure AgNCs were close to one another, the change of the MO absorption peak can still be monitored during the photocatalytic reactions. During the one-hour reaction time, there was only a slight change of the MO absorbance (results not shown).

There are a number of observations that strongly suggest that the catalysis occurs within the cage cavity of these particles. 1) The observation that oxidized Ag (which is only present on the inside walls of the cavity) is required for the catalytic process; 2) the dependence of the catalytic rate on the cavity size; 3) the fact that solid Ag cubes have no significant catalytic activity.

The photocatalytic activity of the three classifications of AuNCs (box-like, porous, and frame-like) can be distinguished from one another. Among these three different categories, the most inactive one is the box-like AuNCs (samples I, IV, and VII) and the most active one is the porous AuNCs (samples II, V, and VIII). The rate constants for the photo-degradation of MO by samples I, IV, and VII (box-like) were found to be 0.002, 0.002, and 0.007 min^{-1} of cage sizes of 50, 75, and 100 nm, respectively (slope of black data points in Figure 3-7). The rate constants for the photo-degradation of MO by samples II, V, and VIII (porous) were all far beyond 0.010 min^{-1}, (slope of the red data points in Figure 3-7) with the highest rate of 0.034 min-1 for the 75nm size porous cages (sample V). The reaction rate constants of frame-like AuNCs (slope of the blue data points in Figure 3-7) were all in-between the box-like and porous AuNC rates.

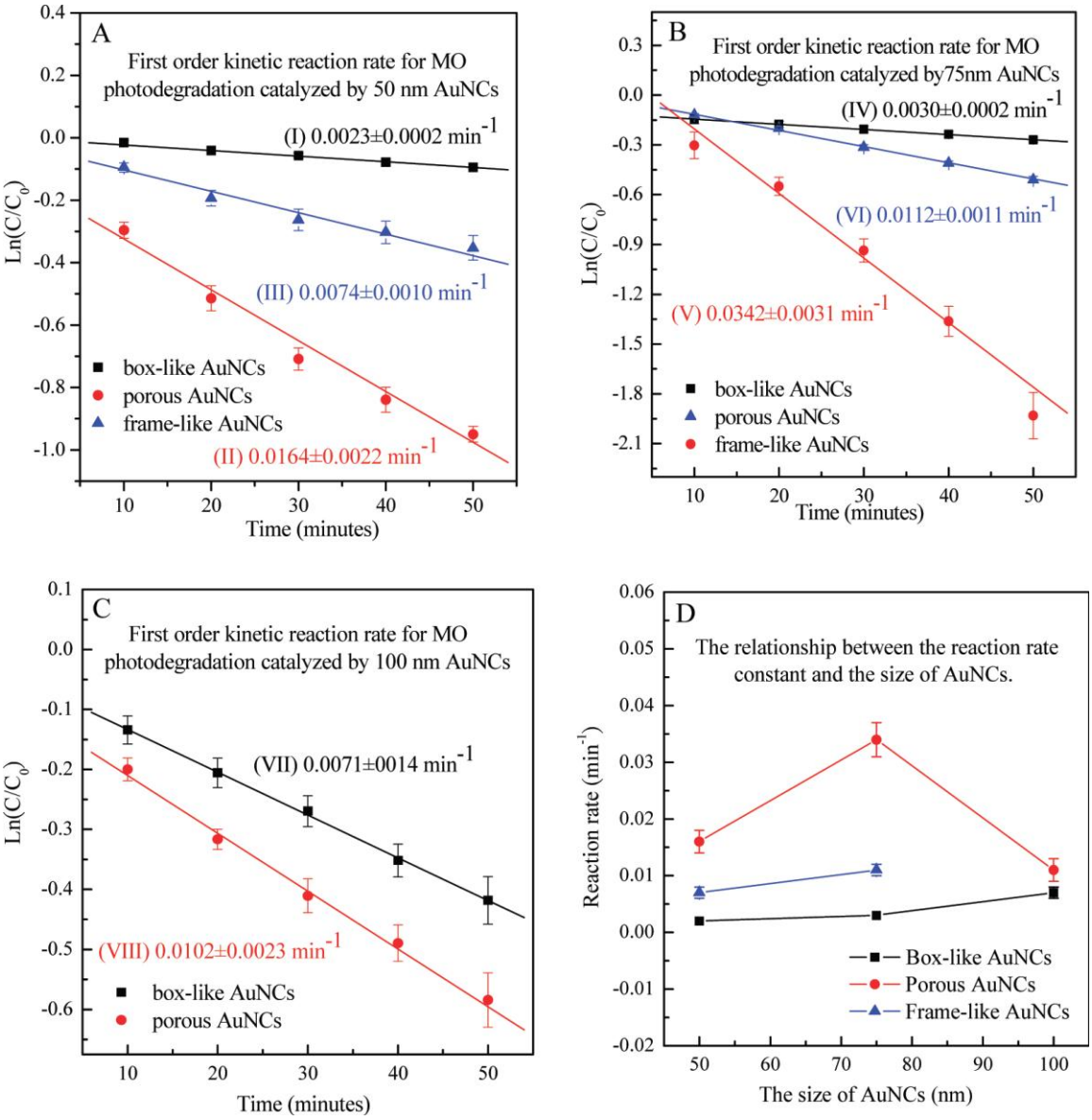

Figure 3-7: First-order relationship for the photocatalytic degredation of methyl orange by AuNCs of different cage sizes: (A) 50, (B) 75, and (C) 100 nm. Three different colors represent different groups of AuNCs: black is the boxlike AuNCs, red is the porous AuNCs, and blue is the framelike AuNCs. (D) The correlation between the size of AuNCs and the reaction rate and the comparison of three different kinds of AuNCs.

3.4 Possible Mechanism

Upon excitation of silver oxide above the band-gap energy, electrons are excited from the valence band to the conduction band, generating a hole in the valence band. Water molecules in the solution are oxidized into hydroxyl radicals and protons by the holes in the valence band [27-28] while the electrons in the conduction band reduce oxygen in the presence of water molecules into hydroxyl and peroxide radicals. Those generated radicals react with the MO molecules, resulting in MO radicals. MO radicals undergo intramolecular fragmentation and the two MO radicals may be combined together to form dimer molecules. It is necessary to continuously produce hydroxyl radicals to continue the photo-degradation reactions. The hydroxyl radical generation process is depicted in Figure 3-8A and B.

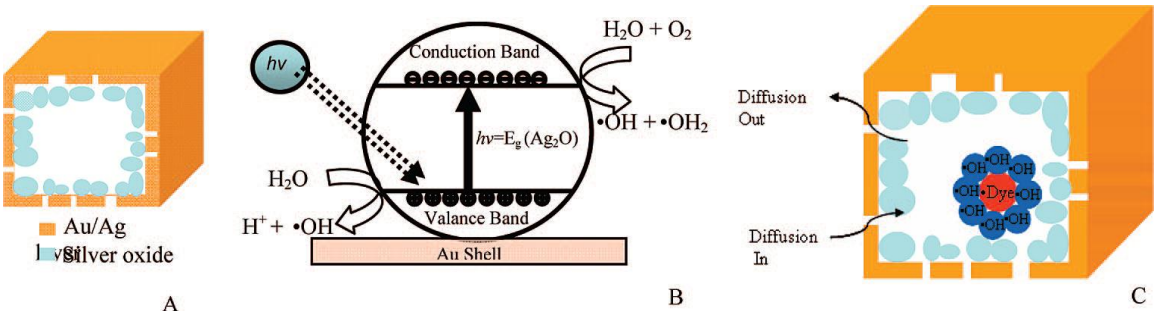

Figure 3-8: Schematic diagrams of (A) the oxygen-treated gold nanocage; (B) the photochemical generation of hydroxyl radical by silver oxide; (C) pores in the walls allowing solution to diffuse into the cavity where photodegradation takes places. When the size of the cage reaches a certain size, it could create a cage effect that confines the hydroxyl radicals inside the cavity.

There are three factors affecting the rate of the reaction. The first factor is the surface area of the Ag_2O covered wall inside the cavity. Since the inner walls of the AuNCs are coated with Ag_2O, the hydroxyl radicals are generated on the inner surface of the cavity. The increased surface area inside the cavity of the particle contributes to the increase in the concentration of the hydroxyl radical as well as an increase in the collision

probability. The second factor is the pore size of the AuNCs. The pore size in the wall of the cage could affect the rate of the photocatalytic reactions. The reactant dyes and the product photofragments diffuse in and out through the pores of the cage. Thus the pore size on the particle walls serves to regulate the flux of molecular species and thus maintains the steady state concentration during the reaction. The third factor is the size of the cage in which the hydroxyl radicals and the MO collide with each other. The cavity size thus controls the collision rate between the hydroxyl radicals and the MO dye molecules.[29]

There are three different cube sizes of AuNCs and the cavity sizes can be controlled by adding various amounts of gold salt. For the particles with the smallest cavity, the box-like AuNCs (samples I, IV, and VII), the reaction rate of all three sizes are the slowest (under 0.007 min^{-1}). Previously it was mentioned that the most significant reason for the low activity of box-like AuNCs is because they lack pores in their walls. The dye molecules could not diffuse easily and rapidly due to the pore-less walls of box-like AuNCs. This means the reactants could not be catalyzed effectively. However, this could also be attributed to the high surface coverage of the capping material to the external surface of the solid cube, which prevents molecular species from reacting with the surface. However, the reaction rate of the frame-like AuNCs is not relatively large either (under 0.012 min^{-1}), even though there are numerous pore channels on the walls for the reactants to diffuse inside the cavity. In this case, the determining factor is the small Ag_2O surface area inside the cavity. In preparation of frame-like AuNCs, hollow structures and pores are routinely produced. While this results in the formation of large pore channels, it also causes the decrease in the silver layers on the inner surface areas. This insufficient surface area of silver oxides could be the reason for the low activity of frame-like AuNCs.

Therefore, achieving the optimum reaction rate requires (1) that there be a high surface area of Ag (which is oxidized to Ag_2O) on the inner wall of the cage to generate

sufficient hydroxyl radicals, (2) that the channel (pore) sizes are sufficiently large enough to allow the reactants and products to diffuse into and out of the cavity but small enough to keep the radical steady state concentration high, and (3) that the cavity size inside the cage is appropriately sized to allow for an optimum collision rate between the reactants. When the pore sizes and surface area of silver oxide achieve a good balance, the cavity forms a "cage effect", meaning that the dye molecules could be caged by surrounding hydroxyl radicals and undergo a large number of collisions per unit time to enhance the reaction rate (Figure 3-8C). In our case, the cavity size of 75 nm AuNCs results in a reaction rate of 0.034 min^{-1}, which is twice as large as the rate with our other AuNCs catalysts.

3.5 Conclusion

Quantitative comparison can be made with other non nanocage oxide catalysts, such as TiO_2[14] and ZnO[15]. The specific reaction rate constant is 0.034, 0.040, and 0.010 min^{-1} for the AuNCs, TiO_2[14] and ZnO[15], respectively. The reaction rate constant of TiO_2 is larger than that of AuNCs. However, the concentration of the catalysts used in TiO_2 (0.3 g/100 mL) is 15 times larger than that used in our experiment (0.02 g/100 mL). Furthermore, the strength of lamp used in the TiO_2 experiment is 500 W, while that used in our system is only 50 W. Thus one could conclude that the Ag_2O within the cavity of the AuNCs seems to be a more efficient photocatalyst. The explanation for the extremely high activity of the AuNCs is that it has an optimum balance of the three properties listed above, namely, a cavity with high Ag concentrations with pore sizes that allow the reactants and products to diffuse in and out without restrictions while confining the reactants in a small region that optimizes the collision frequency with hydroxyl radicals. The surface area of the silver oxides, pore channel sizes, and cavity sizes seem to be the crucial factors that determine the AuNCs activity, and these three factors can be

easily tuned by the galvanic synthetic method to allow for the largest enhancement of the nanoreactor.

3.6 References

[1] Li, Y.; Kunitake, T.; Fujikawa, S. *J. Phys. Chem. B* **2006**, *110*, 13000.

[2] Ng, Y. H.; Ikeda, S.; Harada, T.; Higashida, S.; Sakata, T.; Mori, H.; Matsumura, M. *Adv. Mater.* **2007**, *19*, 597.

[3] Yin, Y. D.; Rioux, R. M.; Erdonmez, C. K.; Hughes, S.; Somorjai, G. A.; Alivisatos, A. P. *Science* **2004**, *304*, 711.

[4] Su, F. B.; Lee, F. Y.; Lv, L.; Liu, J. J.; Tiax, X. N.; Zhao, X. S. *Adv. Funct. Mater.* **2007**, *17*, 1926.

[5] Zhou, S. H.; Varughese, B.; Eichhorn, B.; Jackson, G.; Mcllwrath, K. *Angew. Chem., Int. Ed.* **2005**, *44*, 4539.

[6] Chen, J.; Wiley, B.; Li, Z.; Campbell, D.; Saeki, F.; Cang, H.; Au, L.; Lee, J.; Li, X.; Xia, Y. *Adv. Mater.* **2005**, *17*, 2255.

[7] Lee, J.; Park, J. C.; Song, H. *Adv. Mater.* **2008**, *20*, 1523.

[8] Sun, Y.; Xia, Y. *Science* **2002**, *298*, 2176.

[9] Sun, Y.; Mayers, B.; Xia, Y. *Adv. Mater*. **2003**, *15*, 641.

[10] Cobley, C. M.; Campbell, D. J.; Xia, Y. N. *Adv. Mater.* **2008**, *20*, 748.

[11] Sun, Y.; Mayers, B.; Xia, Y. *Nano Lett.* **2002**, *2*, 481.

[12] Hoffmann, M. R.; Martin, S. T.; Choi, W.; Bahneman, D. *Chem. Rev.* **1995**, *95*, 69.

[13] Hachem, C.; Bocquillon, F.; Zahraa, M. B. *Dyes Pigments* **2001**, *49*, 117.

[14] Lin, X.; Huang, T.; Huang, F.; Wang, W.; Shi, J. *J. Phys. Chem. B* **2006**, *110*, 24629.

[15] Wu, J.; Tseng, C. *Appl. Catal., B* **2006**, *66*, 51.

[16] Rehren, F.; Muhler, M.; Bao, X.; Schlogl, R.; Ertl, G. Z. *Phys. Chem., Bd*. **1991**, *174*, 11.

[17] Strehlow, W. H.; Cook, E. *J. Phys. Chem. Ref. Data* **1973**, *2*, 163.

[18] Skrabalak, S. E.; Au, L.; Li, X.; Xia, Y. *Nat. Protocols* **2007**, *2*, 2182.

[19] Sun, Y.; Xia, Y. *Nano Lett.* **2003**, *3*, 1569.

[20] Lu, X.; Au, L.; McLellan, J.; Li, Z.; Marquez, M.; Xia, Y. *Nano Lett.* **2007**, *7*, 1764.

[21] Banerjee, S.; Maity, A. K.; Chakravorty, D. *J. Appl. Phys*. **2000**, *87*, 8541.

[22] Yin, Y.; Li, Z.; Zhong, Z.; Byron, G.; Xia, Y.; Venkateswaran, S. *J. Mater. Chem.* **2002**, *12*, 522.

[23] Kapoor, S. *Langmuir* **1998**, *14*, 1021.

[24] Chen, M.; Wang, L.; Han, J.; Zhang, J.; Li, Z.; Qian, D. *J. Phys. Chem. B* **2006**, *110*, 11224.

[25] Watehouse, G. I.; Bowmaker, G. A.; Metson, J. B. *Phys. Chem. Chem. Phys*. **2001**, *3*, 3838.

[26] Pettinger, B.; Bao, X.; Wilcock, I.; Muhler, M.; Schlogl, R.; Ertl, G. *Angew. Chem. Int. Ed. Engl.* **1994**, *33*, 85.

[27] Comparelli, R.; Fanizza, E.; Curri, M. L.; Cozzoli, P. D.; Mascolo, G.; Passino, R.; Agostiano, A. *Appl. Catal. B* **2005**, *55*, 81.

[28] Bahr, Y.; Mahmoud, M. A. *J. Phys. Chem. Solids* **2007**, *68*, 413.

[29] Braden, D. A.; Parrack, E. E.; Tyler, D. R. *Coord. Chem. Rev.* **2001**, *211*, 279.

CHAPTER 4

PLASMONIC FIELD EFFECT ON THE HEXACYANOFERRATE – THIOSULFATE ELECTRON TRANSFER CATALYTIC REACTION ON GOLD NANOPARTICLES

Abstract

The rate of the catalytic reaction between hexacyanoferrate (III) and thiosulfate on gold nanoparticles is found to increase when irradiated with light in resonance with surface plasmon absorption of the gold nanoparticles. Turning on the plasmonic field by turning on light at the surface plasmon extinction band could increase the rate by one of two possible mechanisms. In the first one, the electromagnetic field could change its radiative or nonradiative electron transfer process (Mechanism Ⅰ). In the other mechanism (Mechanism Ⅱ), the strongly absorbed light by the gold nanoparticles is rapidly converted from light energy into heat energy that increases the temperature of the medium and increases the reaction rate. In order to determine which mechanism the plasmonic catalytic effect follows, we determined the activation energy of the reaction by heating the reaction solution via two different methods: irradiation at the surface plasmon resonance of the gold catalyst and by direct heating in a thermostat. The two activation energies are found to be the same, suggesting that the plasmonic field effect in this electron transfer reaction is thermally induced.

4.1 Introduction

Nanoscale metallic particles have been the subject of intense study in recent years because of their unique catalytic and optical properties.[1-5] Surface plasmon resonance (SPR) is an interesting optical phenomenon induced by the coupling of the incident electromagnetic wave of light with the conduction band electrons in the metal. This induces a coherent electronic oscillation of the free electrons of the metal with respect to the positive metallic lattice as a result of the oscillating electromagnetic field. This electronic oscillation can be simply visualized as a photon confined to the size of the nanostructure, constituting an intense surface electromagnetic field that is detected over distances comparable to the size of the nanoparticle.[6]

There is a rich variety of applications utilizing the SPR property of gold nanoparticles, including optical energy transport,[7,8] chemical and biological sensors,[9-12] surface-enhanced Raman scattering (SERS),[13-15] and the photothermal effect in which the plasmonic energy is converted rapidly into heat that raises the medium temperature.[16,17] This mechanism is used in photothermal cancer therapy by gold nanoparticles.[18-20] The plasmonic field's effect has been observed on the rate of the non-radiative electronic relaxation in CdTe-Au core-shell semiconductor.[21] The mechanism was found to result from radiative coupling between the plasmonic field and the electrons in the semiconductor. The effects of the plasmonic field on the rate of retinal photoisomerization and the reprotonation of the Schiff base in the photocycle of *bacteriorhodopsin* has also recently been reported.[22]

In the present paper, we examine the effect of exciting the gold SPR on the rate of an electron transfer reaction where the gold nanoparticles serve as the catalyst. The catalytic reaction studied here is the reduction of ferricyanide by thiosulfate: [23-25]

$$2Fe(CN)_6^{3-}{}_{(aq)} + 2S_2O_3^{2-}{}_{(aq)} \rightarrow 2Fe(CN)_6^{4-}{}_{(aq)} + S_4O_6^{2-}{}_{(aq)} \qquad (1)$$

The catalyst used here is 25 nm gold nanospheres with an SPR band at 527 nm and 75 nm gold nanocages with an SPR band at 796 nm. Exciting the surface plasmon resonance during the catalytic process could accelerate the rate of the reaction by a number of mechanisms: 1) electronic density exchange between the excited gold nanoparticle and nearby reactants; [26] 2) the plasmonic near field on electron transfer process itself; [21,27,28] or 3) the rapid conversion of the excited SPR into heat , rising the solution temperature and thermally accelerating the chemical reaction. [29,30] If it is the third mechanism that is accelerating the rate of the chemical reaction, the activation energy measured by changing the solution temperature by increasing the light intensity should be the same as that determined by raising the reaction temperature in thermostatic water bath.

The value of the activation energy for this electron transfer reaction is found to be similar when measured either by thermostatic water bath or by plasmonic photothermal reactor. This observed result supports the conclusion that the conversion of the excited SPR into heat is the dominant effect and other possible processes involving the surface plasmon field on the electronic dynamics during the reaction are negligible.

4.2 Experimental Section

Synthesis of Gold Nanocages:

In each synthesis, 5 mL ethylene glycol (EG) was first heated in an oil bath at 150 $^{\circ}$C for 4 h to remove trace amounts of water. Then two solutions, one containing 0.94 M of silver nitrate and another containing 0.375 M poly-(vinyl pyrrolidone) (PVP, Mw: 55,000) and 0.22 mM NaCl were injected into treated EG at the same time. In a typical synthesis, the solution underwent a number of color changes before the color became stable after approximately 46 hr. The samples were washed with acetone and then with water to remove excess EG and PVP. A 5-ml aliquot of the aqueous dispersion

containing silver cores was refluxed for 10 min. Aliquots (15mL) of 1 mM $HAuCl_4$ aqueous solution were added drop-wise to the refluxing solution. This mixture was continuously refluxed until its color became stable. Vigorous magnetic stirring was maintained throughout the synthesis.[31,32]

Synthesis of Gold Nanospheres:

A 50 mL solution of 0.25 mM $HAuC1_4$ was brought to a boil and 0.40 mL of the 1% citrate solution by weight was added under continuous stirring. This protocol is based on the reduction of $HAuCl_4$ by citrate, which serves both as a reducing agent and an anionic stabilizer through the following reaction:

$$6AuCl^{-}_{4\,(aq)} + C_6H_8O_{7(aq)} + 5H_2O_{(aq)} \rightarrow 6CO_{2(g)} + 24Cl^{-}_{(aq)} + 6Au_{(S)} + 18H^{+}{}_{(aq)} \qquad (2)$$

Boiling and stirring were continued for several minutes and a brilliant red color appeared. The solution was cooled in a bath at 25 ℃ and stored at 5-10 ℃.[33,34] The final concentration was adjusted to be 2.0 mM before as a catalyst. The concentration was determined by ICP-MS (VG PlasmaQuad 3).

Electron Transfer Reaction:

A 0.1 M stock solution of hexacyanoferrate (III) was prepared using the potassium hexacyanoferrate (III) salt. A 1.0 M stock solution of thiosulfate was prepared using the sodium thiosulfate salt. The pH of both stock solutions was adjusted to 7.0 in order to carry out the reaction at a pH of 7.0. The electron transfer reaction between hexacyanoferrate (III) ions and thiosulfate ions was carried out by adding 20 μL of 0.1 M potassium hexacyanoferrate (III) ions and 20 μL of 1 M sodium thiosulfate to 2.0 mL of gold nanospheres or gold nanocages solutions.

Kinetics of the Electron Transfer Reaction

The kinetics of the electron transfer reaction was monitored by using absorption spectroscopy with an Ocean Optics UV-vis spectrometer HR4000Cg-UV-NIR. The intensity of the hexacyanoferrate (III) absorption peak at 420 nm was monitored as a function of time every 10 minutes for 50 min. The rate constant of the reaction was determined from the slope of the graph of –ln A vs. time, assuming that the reaction is first order, since thiosulfate concentration was kept high (1.0 M). The rate constant of the reaction was determined at five different temperatures. In order to carry out the reaction at different temperatures, two different heating methods were used. In the first one, the water thermostat method, the quartz cell was placed into a circulator (Neslab, RTE-110) that was heated to the desired temperature by water circulation.

The other method was the gold plasmonic photothermal method. Two kinds of laser have been used and compared:

Continuous Wavelength Laser

An argon ion laser (Coherent, Innova 300, 514 nm) was used to irradiate a gold nanosphere solution and a diode laser (Power Technology, 808 nm) was used to irradiate the gold nanocage solution. The solution temperature was measured by using a handheld infrared thermometer (Omega) with careful calibrations. The activation energy of the reaction was determined from the slope of the graph of ln k vs. 1000/T.

Pulsed Laser

The amplified Ti-Sapphire femtosecond laser system (Clark-MXR CPA 1000) was employed to irradiate gold nanocage solutions. Briefly, the Ti:Sapphire Oscillator (Clark -MXR NJA-5) was pumped by a frequency-doubled Nd:Vanadate laser (Coherent Verdi) with an output power of 3.5 W at 532 nm, generating laser pulses of 100 femtosecond duration with a 90 MHz repetition rate at 800 nm (Scheme 4-1). A

frequency-doubled Nd:YAG laser (GCR-2, Spectral Physics, 532 nm with a bandwidth of 10 ns) was used to irradiate gold nanospheres (Scheme 4-2).

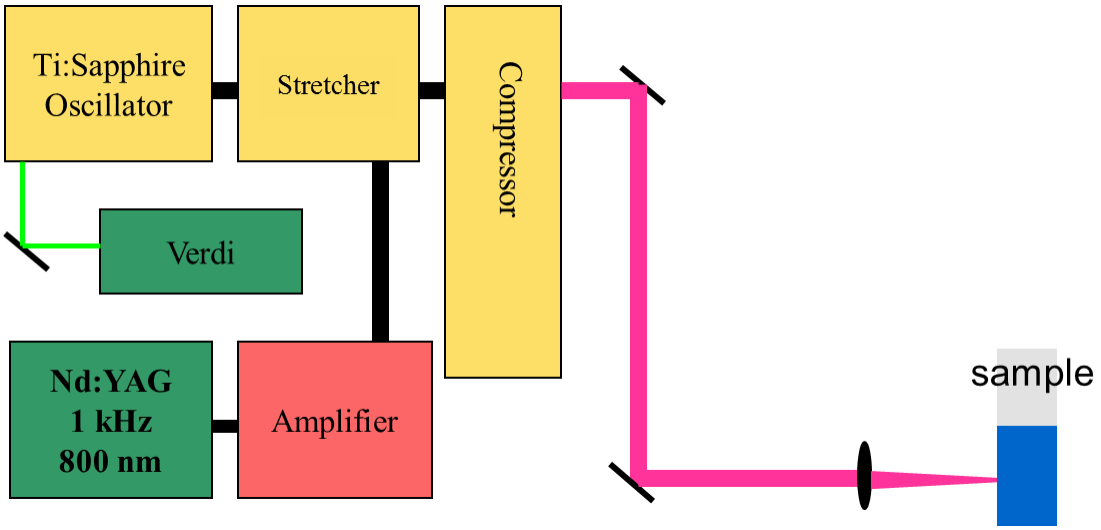

Scheme 4-1: Experimental setup of the femto second laser (800 nm). Photoexcitation of gold nanocages to catalyze electron transfer reaction

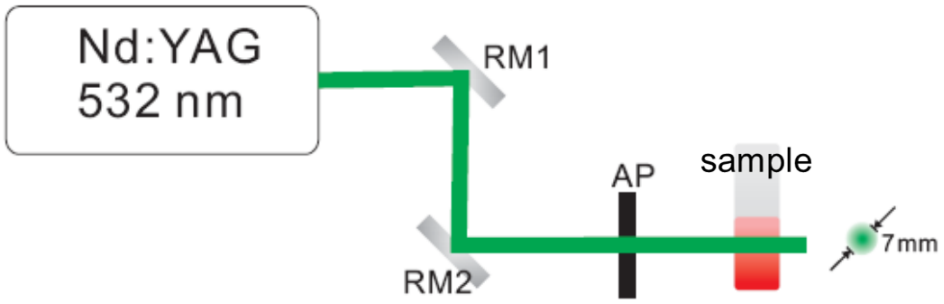

Scheme 4-2: Experimental setup of the nanosecond laser (532 nm). Photoexcitation of gold nanospheres to catalyze electron transfer reaction

Recycling the Electron Transfer Reaction:

In order to test the recyclability of the gold nanocatalysts, the same particles were used to catalyze multiple cycles of the electron transfer reactions. The absorption spectra were measured to make sure that all of the hexacyanoferrate (III) ions were used up, signaling that the first cycle of the reaction was over. After the first cycle of the electron transfer reaction was completed, the second cycle of the electron transfer reaction was initiated by adding 2.0μL of 1 M potassium hexacyanoferrate (III) and 2.0μL of 1 M sodium thiosulfate to the solution. Both the 1.0 M potassium hexacyanoferrate (III) stock solution and the 1.0 M sodium thiosulfate stock solution are adjusted to a pH of 7.0 prior to their use. Then the stability and catalytic activity of the nanoparticles was compared between the first and second cycle.

4.3 Results and Discussions

Preparation of Gold Nanospheres and Gold Nanocages

Two gold nanostructures were synthesized and used to investigate their catalytic activity on the electron transfer reaction. One is the gold nanosphere which was synthesized by Freund's method.[33] By fixing the ratio of citrate to $HAuCl_4$ at 0.7 this yielded 25±4 nm gold nanospheres with a surface plasmon resonance (SPR) band at 527 nm (Figure 4-1A). The other shape is the gold nanocage (AuNC). The synthetic approach of AuNCs is based on the galvanic replacement reaction between the silver core and the gold ion salt solution. The gold ions are reduced at the expense of silver atoms, which are oxidized via the following equation:

$$3Ag_{(s)} + AuCl^-_{4\,(aq)} \rightarrow Au_{(s)} + 3Ag^+_{(aq)} + 4Cl^-_{(aq)} \qquad (3)$$

The SPR band of AuNCs can be tuned by adding various amount of $HAuCl_4$ to generate different thickness of the walls at various porosities. The morphology of the AuNCs used in this paper is almost hexagonal structures of 75±6 nm sizes and with the SPR band at 796 nm (Figure 4-1B).

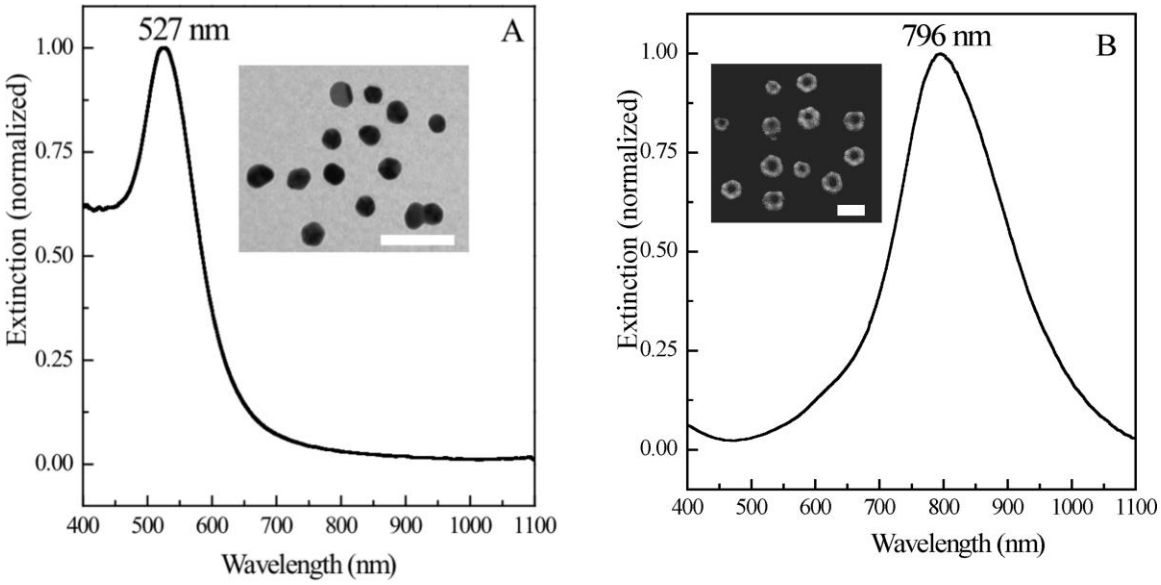

Figure 4-1: Normalized surface plasmon resonance spectra of (A) the gold nanospheres, and (B) the gold nanocages; the scale bar of both insets is 75 nm.

Electron Transfer Catalytic Reactions on Gold Nanoparticles

Continuous Wavelength Laser

The electron transfer reaction between hexacyanoferrate (Ⅲ) ions and thiosulfate ions is catalyzed by the gold spheres or the gold nanocages. The reaction was carried out at different temperatures and the kinetics of the reaction was monitored by using absorption spectroscopy. The disappearance of the hexacyanoferrate (Ⅲ) absorbing at 420 nm was monitored for every 10 min during the first 50 min of the reaction. Figure 4-2A-C shows the catalytic reaction that was carried out in the presence of gold spheres. The two peaks, one at 420 and the other at 530 nm, are a result of the hexacyanoferrate (Ⅲ) species and the SPR band of gold spheres, respectively. The electron transfer reaction

was compared at two different temperatures. The normalized optical density value (O.D.) of hexacyanoferrate (Ⅲ) at the end of the reaction performed at room temperature was 0.65. (22 ℃, Fig 4-2A) However the final O.D. value was only 0.49 for the reaction performed at 40 ℃ (Fig 4-2B), where the temperature was controlled by a water bath. This temperature dependent phenomenon also occurs when the reaction is catalyzed by the gold nanocages. The O.D. value of hexacyanoferrate (Ⅲ) at the end of the reaction was 0.85 at room temperature (22 ℃, Fig 4-2D) and 0.47 at 40 ℃ (Fig 4-2E).

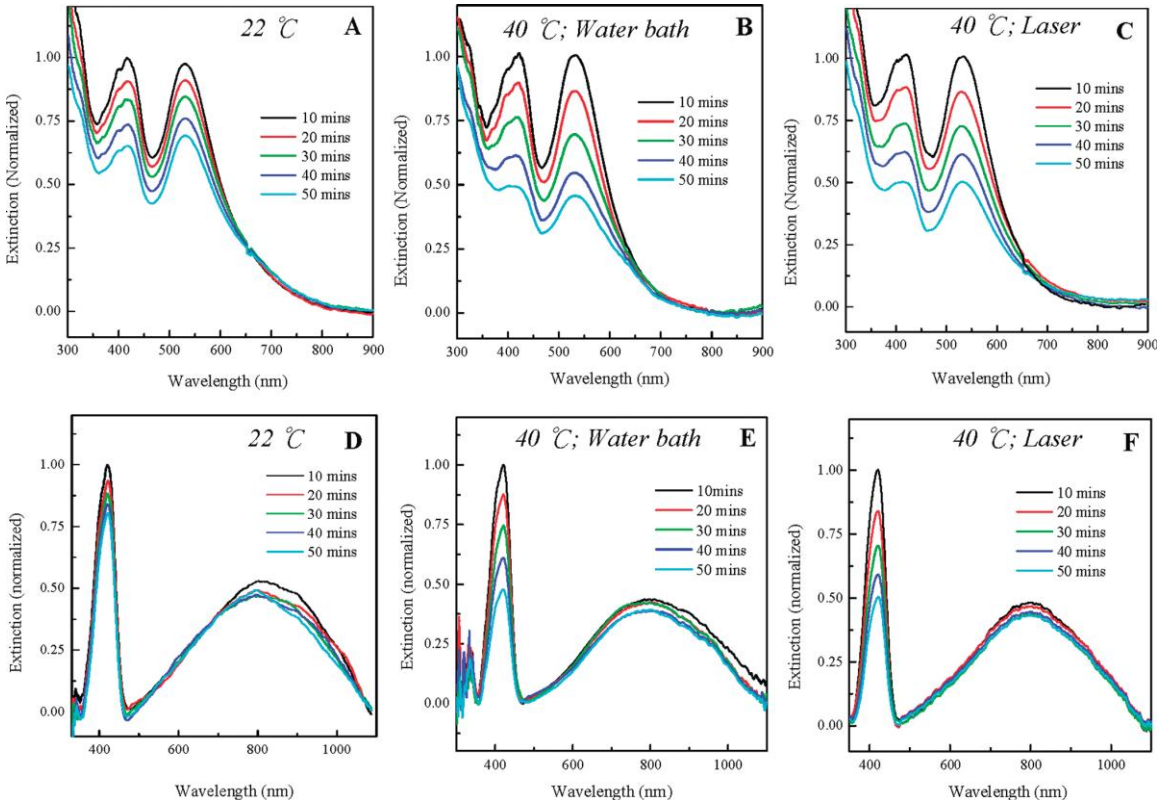

Figure 4-2: The electron transfer reactions catalyzed by the gold nanospheres (A-C) and by the gold nanocages (D,E). (A and D) The reaction is operated at room temperature (22 ℃). (B and E) The reaction is operated at 40 ℃ heated by water bath. (C and F) The reaction is operated at 40 ˚C heated by CW laser.

The dissimilarity between reactions catalyzed by gold nanospheres and gold nanocages is because the extinction value of SPR band of gold nanospheres at 530 nm

decreased with the decrease in concentration of hexacyanoferrate (Ⅲ), whereas the SPR band value of gold nanocages at 800 nm remained unchanged with time. This phenomenon can be explained by the difference in the synthetic method of these two catalysts. The gold nanospheres were stabilized by citrate and the gold nanocage was capped by ethylene glycol and PVP. Citrate is a small molecule and its ability to stabilize gold nanoparticles is not as good as polymers. Moreover, one reactant of this electron transfer reaction is thiosulfate. It is known that sodium thiosulfate is able to extract gold from minerals and form strong complexes $[Au(S_2O_3)_2]^{3-}$.[35,36] The gold atoms on the gold nanospheres dissolve after mixing with thiosulfate ions because of the poor protection of the citrate capping material. The dissolution process of gold and the loss of the weak citrate capping agent also caused a serious aggregation of gold nanospheres. The radius of diffusion of the gold nanospheres was measured by the Dynamic Light Scattering (DLS) technique. The radius of pure gold nanospheres was around 30 nm and the radius increased greatly to 700 nm after mixing with thiosulfate solutions (Fig 4-3A). On the contrary, the radius of diffusion of the gold nanocages increased slightly from its original value of 80 nm to 114 nm after adding the thiosulfate solutions (Fig 4-3B). The aggregation of gold nanospheres after mixing with the thiosulfate solutions was also observed by the TEM images (Fig 4-3A). The results from DLS and TEM images both showed that the gold nanocages are better protected by polymers than the gold nanospheres protected by citrate.

Those stabilizing polymers not only prevent the gold from leaching during the reactions but also maintained the catalytic ability of gold nanocages. The reaction rate constant of gold nanocages during the first cycle was 0.0076 min^{-1} and 0.0062 min^{-1} during the second cycle. However, the reaction rate constant of gold nanospheres was 0.011 min^{-1} for the first cycle and 0.0042 min^{-1} for the second cycle. The recycling experiment showed the second cycle activity of gold nanocages was at 85 % compared to the first cycle, while it dropped to 32 % for gold nanospheres. The structure of the gold

nanospheres was essentially destroyed, leading to aggregation due to the effects of the thiosulfate. Thus their catalytic ability was not preserved for the recycling experiment. On the other hand, the gold nanocages were stabilized well by the polymer capping material during the reactions, and the conservation of structure helped maintain their catalytic activity.

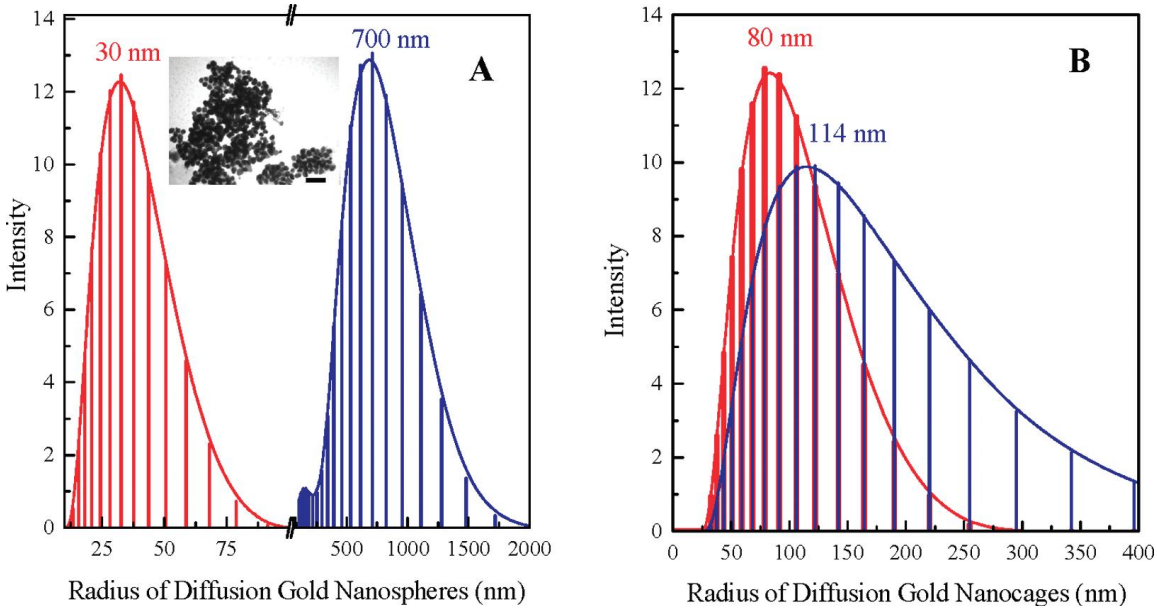

Figure 4-3: The results of hydrodynamic radius of diffusion species as measured by dynamic light scattering. (A) The average radius of diffusion of pure gold nanospheres is 30 nm shown in red lines. After 10 min of mixing with thiosulfate solutions (1.0 M, 20 μL), the average radius of diffusion of gold nanospheres increases to 700 nm shown in blue lines. The inset TEM image is the gold nanospheres after mixing with thiosulfate solutions showing aggregated form of the gold nanospheres and the scale bar is 100 nm. (B) The average radius of diffusion of pure gold nanocages is 80 nm, shown in red lines. After 10 min of mixing with thiosulfate solutions (1.0 M, 20 μL), the average radius of diffusion of gold nanocages increases slightly to 114 nm shown in blue lines. The changes in the radius of diffusion for gold nanospheres and gold nanocages after mixing with hexacyanoferrate (0) were also measured by DLS. No change in the radius of diffusion is observed by hexacyanoferrate (III) for both gold nanospheres and gold nanocages (data not shown here).

Pulsed Laser

In addition to the continuous wavelength laser, pulsed lasers were also used as irradiation sources. A femtosecond laser (wavelength=800 nm) and nanosecond laser (wavelength=532 nm) were used to irradiate gold nanocages and gold nanospheres, respectively. The electron transfer reaction under pulsed laser was shown in Figure 4-4 and 4-5. There were two main drawbacks of using a pulsed laser as the irradiation source. First, the temperature of the reaction solution was in flux. The irradiated solution could not be stabilized at a specific temperature due to the instantaneous irradiation by the pulsed laser. Since the temperature of solution was not stable, the activation energy of reaction could not be measured. The other drawback was that the intense irradiation of the pulsed laser was shown to damage the structure of gold nanospheres. In the absence of reactants, the plasmonic absorption peak of gold nanospheres was decreased under nanosecond laser irradiation with intensity above 2W (Figure 4-6). The color of the gold nanospheres was changed from the original ruby to orange (Figure 4-7), demonstrating that the structure of the gold nanospheres was damaged under nanosecond laser irradiation.

The instantaneous irradiation of a pulsed laser can not be adopted as an appropriate irradiation source in this experiment. The aim of this experiment is to use gold nanoparticles as catalysts and as a heating source to increase the catalytic efficiency of electron transfer reactions. If the structure of the gold nanoparticles is damaged, this affects the catalytic ability of the gold nanoparticles, and the generated heat generated from the gold nanoparticles will be less due to the decreased plasmonic absorption peak. In the next section, the activation energy of plasmonic heating method and thermostatic methods will be compared. The activation energy data is all obtained using a continuous wavelength laser as an irradiation source.

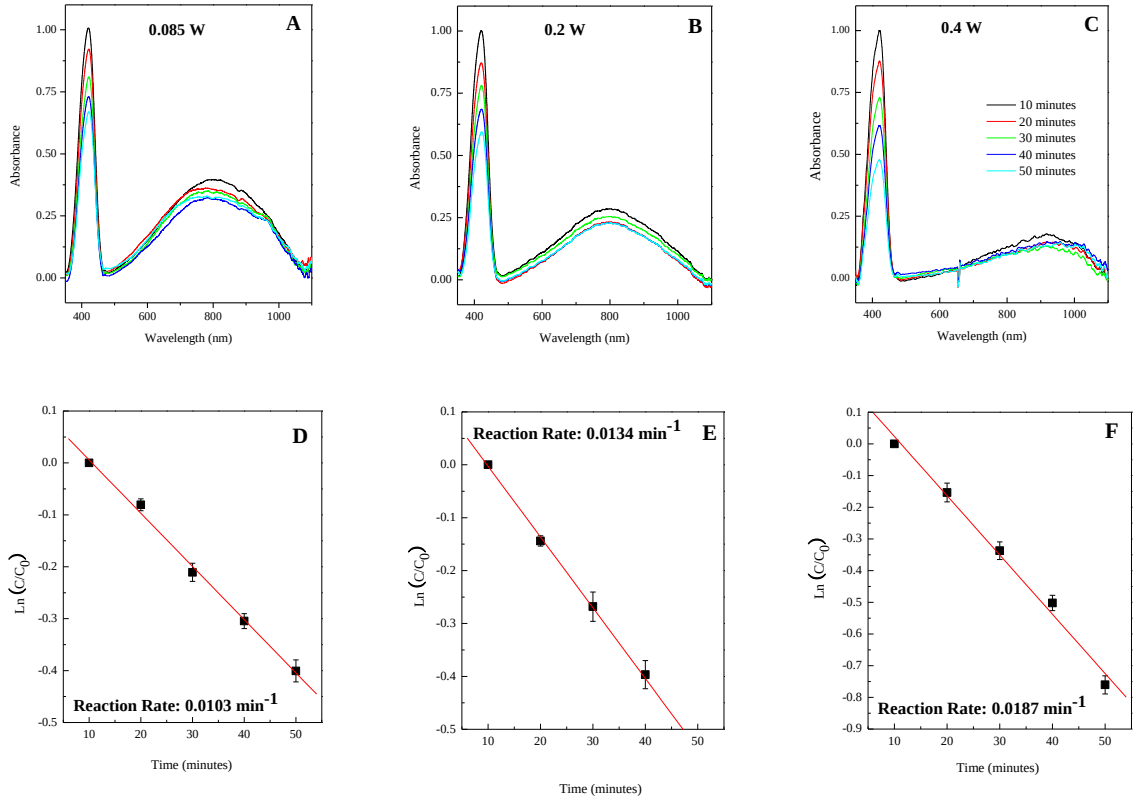

Figure 4-4: (A-C) Absorbance plots of the electron transfer reactions catalyzed by gold nanocages femto second laser irradiation (λirradiation=800 nm) with various irradiation powers. (D-F) Determination of the catalytic rate constant using gold nanocages under femtosecond laser irradiation with 0.085W, 0.2W, and 0.4W laser power, respectively.

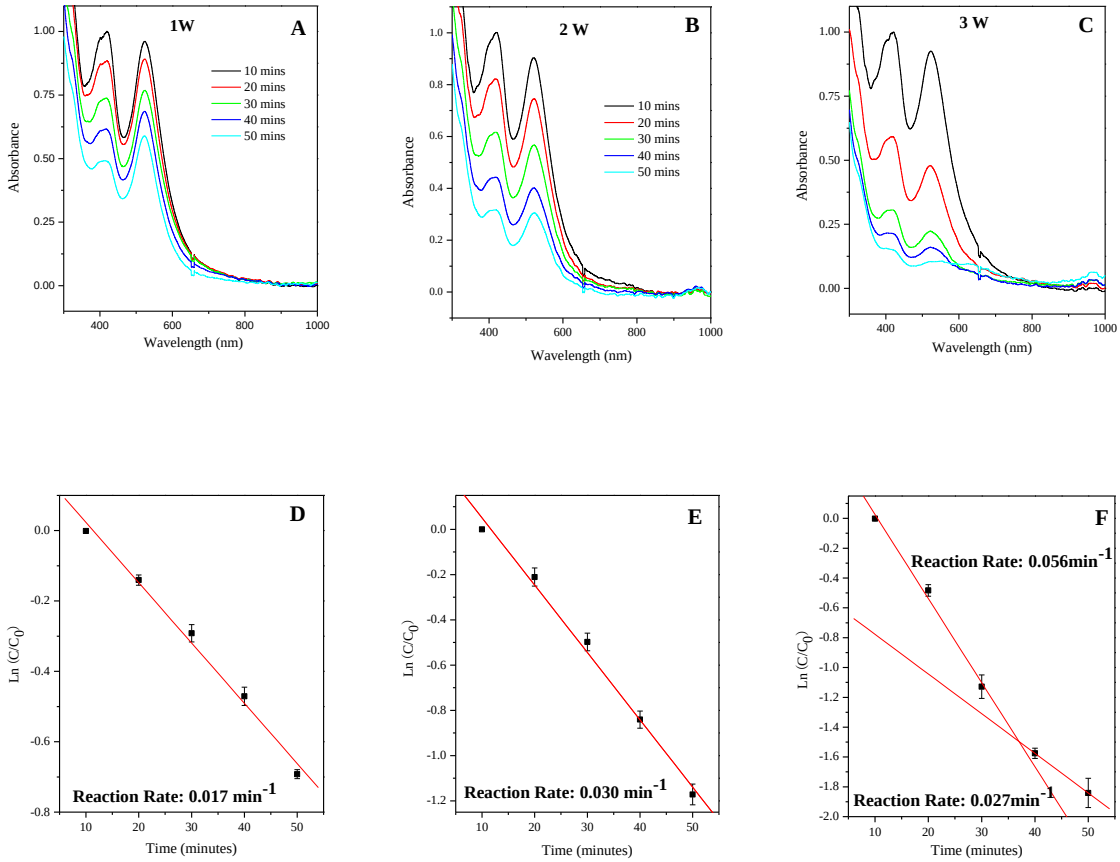

Figure 4-5: (A-C) Absorbance plots of the electron transfer reactions catalyzed by gold nanospheres nano second laser irradiation (λirradiation=532 nm) with various irradiation powers. (D-F) Determination of the catalytic rate constant using gold nanospheres under nano second laser irradiation with 1W, 2W, and 3W laser power, respectively.

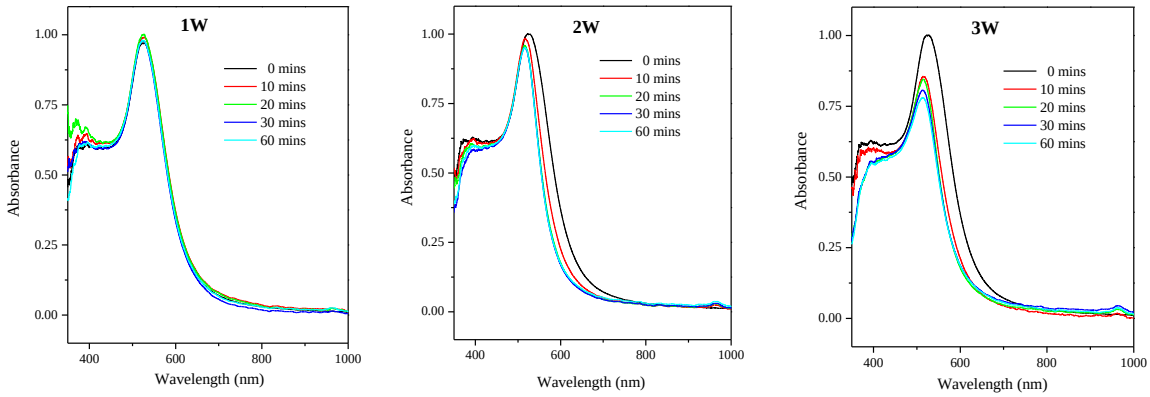

Figure 4-6: (A-C) Gold nanospheres irradiated with nanosecond laser (λirradiation=532 nm) with various irradiation intensity. With the increased laser power, the absorption peak of gold nanospheres is decreased over time.

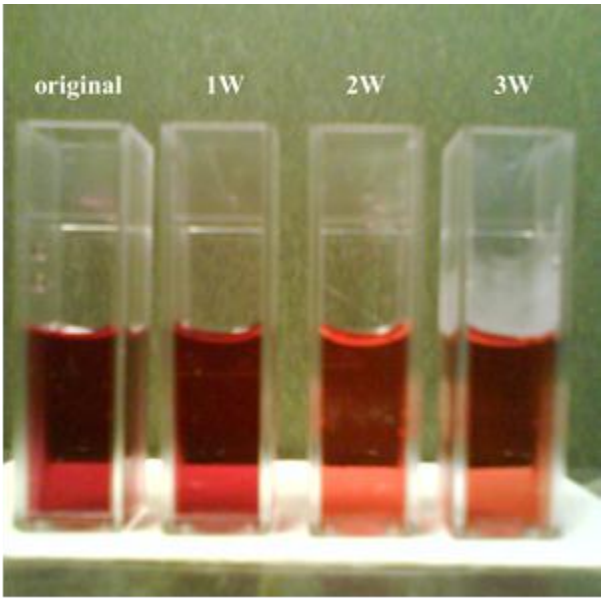

Figure 4-7: The color of gold nanospheres is altered from the original ruby to orange when the intensity of nanosecond laser irradiation is above 2W.

Activation Energy Determination from Thermostatic Water Bath

The activation energies for the electron transfer reaction catalyzed by gold nanospheres and gold nanocages were measured by thermostatic method. The rate constant of the reaction was determined at five different temperatures (22, 30, 35, 40, 50 ℃ for the gold nanospheres; 22, 30, 43, 50, 60 ℃ for the gold nanocages) and the temperature was controlled by the thermostat water bath method. The activation energy was obtained from the slope of the linear Arrhenius plot of ln k vs 1000/T (slope = -Ea/R). The activation energy of the gold nanocages was found to be 24±1 kJ/mole and the gold nanosphere was 29±2 kJ/mole (Figure 4-8A). The lower activation energy of gold nanocages could either be due to differences between the surface gold atomic structure and the internal core atoms or to the presence of the remaining Ag atoms on the cage internal surface. In addition, the gold nanocage with a strong protective polymer surfactant can serve as a more robust and suitable catalyst when a reaction component is harmful to gold, like thiosulfate.

Activation Energy Determination from Photothermal Heating of the Gold Nanoparticles

We found that exposing the reaction mixture with the gold catalyst to light at a frequency resonant with the surface plasmon band raises the solution temperature. In order to examine if the change in the reaction rate by exciting the surface plasmon excitation is a result of thermal effects, we need to measure the activation energy photothermally and compare it with that measured thermally.

We used a laser to irradiate and heat the solution to the desired temperature by adjusting the laser intensity. When gold nanoparticles absorb light, the free electrons in the gold nanoparticles are excited. Excitation at the surface plasmon resonance frequency

causes a collective oscillation of the free electrons. As the electrons cool and interact with the positively charged crystal lattice of the gold nanoparticles, energy is transferred as heat. According to calculations and the photothermal application for cancer therapy, the gold nanoparticles can be regarded as a thermal agent and rapidly convert the light energy into heating the lattice as a result electron-phonon and relaxation process.[37, 38] Subsequently the heat from the gold nanoparticles lattice dissipates into the surrounding environment by phonon-phonon relaxation and the temperature of the surrounding medium is raised.

Two CW laser wavelengths were used here, 514 nm and 808 nm, to irradiate gold nanospheres solution (SPR band at 527 nm) and gold nanocages solution (SPR band at 798 nm), respectively. The gold nanosphere and gold nanocage solutions were homogeneously heated by absorbing the radiation from the continuous lasers. The temperature of the gold nanospheres solution was raised to 40 ℃ and kept constant after 20 min of argon ion laser (1.9 W/cm^2, 514 nm) exposure. Hexacyanoferrate (Ⅲ) and thiosulfate solutions were then added into this gold nanosphere solution to start the catalytic reaction. The solution was under laser irradiation throughout the reaction period to maintain constant temperature. The changes in the optical density of the hexacyanoferrate (Ⅲ) absorption band and SPR band of gold nanospheres were quite similar to the changes occurring at 40 ℃ heated by thermostatic method (Figure 4-2C). The same result of gold nanocages was also observed when the diode laser (2.48 W/cm^2, 808 nm) was used for the irradiation (Figure 4-2F).

The control of temperature in the gold nanocage system was more precise than that in the gold nanospheres system. The temperature was maintained during the entire reaction time (50 minutes) for the gold nanocages while the temperature was only maintained for the first thirty minutes and dropped one to two Celsius degrees in the final twenty minutes for the gold nanospheres. The temperature drop is due to large decrease

in the gold nanospheres concentration during the reaction, as determined from the decrease of the intensity of the SPR band (Figure 4-2C). Although the temperature was changing, the drop was small enough (1-2 ℃) to be acceptable for the reaction rate constant determination of this reaction. Each rate constant was averaged by repeating the experiment five times to diminish the error. The reaction rate constant was obtained for both gold nanospheres and gold nanocages at five different temperatures (22, 32, 36, 42, 50 ℃ for gold nanospheres; 22, 29, 38, 43, 51 ℃ for gold nanocages) by modifying the intensity of laser power and the activation energy was also calculated. The activation energy of the reaction catalyzed by the gold nanospheres was 29±3 kJ/mole and it of gold nanocages was 24±1 kJ/mole (Figure 4-8B). The activation energy observed by using the gold plasmonic heating method for both gold nanospheres and gold nanocages was quite similar to the activation energy obtained by thermostat method (29±2 kJ/mole for the gold nanospheres and 24±1 kJ/mole for the gold nanocages). This demonstrates that the mechanism of how gold nanoparticles catalyze the electron transfer reaction by two different methods is the same and laser exposure does not change or damage the gold nanoparticles.

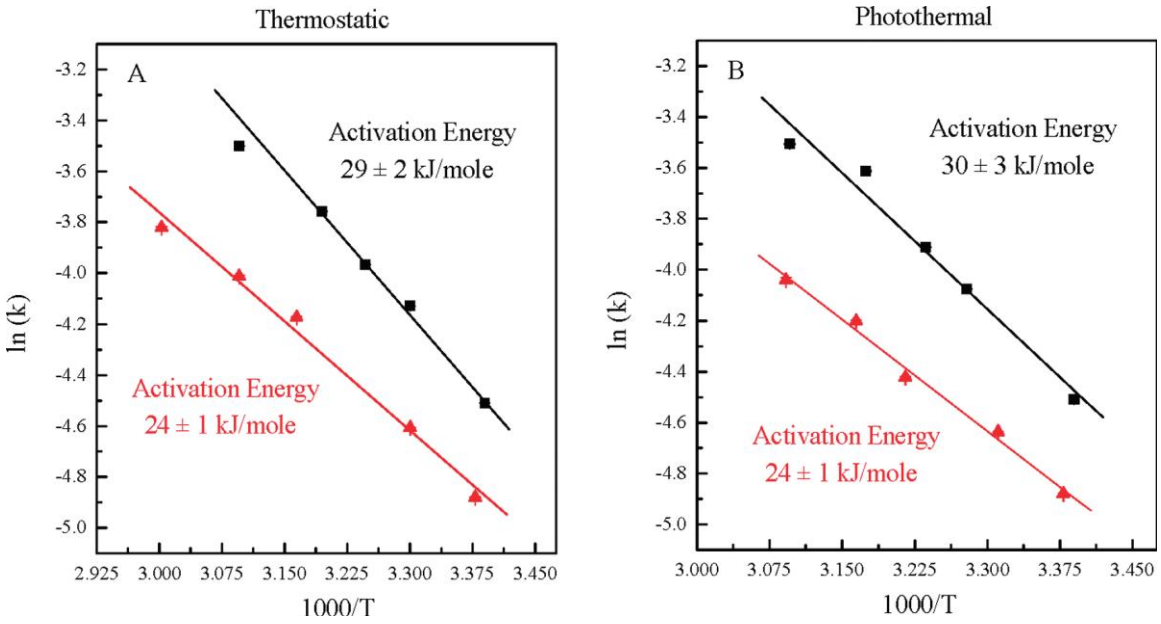

Figure 4-8: The activation energy of the reaction catalyzed by gold nanospheres (9) and gold nanocages (2). The activation energy of the reaction was determined from the slope of the graph of ln k vs 1000/T. (A) The temperature was controlled by a thermostat water bath; (B) the temperature was controlled by a CW laser.

Photothermal Effect on Catalysis

The dependence of the temperature change of the solutions of gold nanoparticles in the absence of any reactant with the strength of the laser power is shown in Figure 4-5. The trend of the temperature change of gold nanospheres resembled that for gold nanocages. Also, the temperature increased slowly with weaker intensity of laser power and then increased rapidly at stronger power. A control experiment was carried out using pure water, instead of gold nanospheres or gold nanocages, under the same light intensity and time of laser exposure. There was no temperature change observed without adding the gold nanocatalysts. One difference between the gold nanosphere and gold nanocage was that the gold nanocage required higher laser intensity compared to gold nanospheres for the same degree of temperature change. The maximum of temperature rise was 30 ℃

for both the gold nanospheres and the gold nanocages. However, the laser intensity requirement for gold nanospheres was 3.04 W/cm^2 while the requirement for gold nanocages was 4.40 W/cm^2 with the same optical density of gold nanoparticles (Figure 4-9). The SPR spectra of the gold nanospheres or gold nanocages were both unchanged after laser irradiation (data not shown).

The difference of the laser power strength used in each case is due to the size difference of the gold nanospheres and the gold nanocages. It is known that the SPR extinction of the gold nanoparticles varies as a function of size and shape. A combination of experimentally measured spectra and computed results using the DDA method both show that the light scattering efficiency is strongly dependent on the gold nanostructure size.[39,40] The scattering efficiency is enhanced with increasing size, so the scattering efficiency of gold nanocages is higher than gold nanospheres. Due to the sharp corners of the cage, the extinction is also expected to be higher. For these two reasons, the amount of light absorbed by the spheres is expected to be higher. The rapid conversion of the absorbed light into heat leads to the spheres to be more effective heating agents than the cages. Furthermore, the gold nanosphere is capped with citrate molecules while the gold nanocage is surrounded by the much larger PVP or ethylene glycol polymers. More heat is transferred to the solution through small molecules than for the nanoparticle with the larger polymers, whose complex vibrations retain a large fraction of the energy and act as an efficient sink.

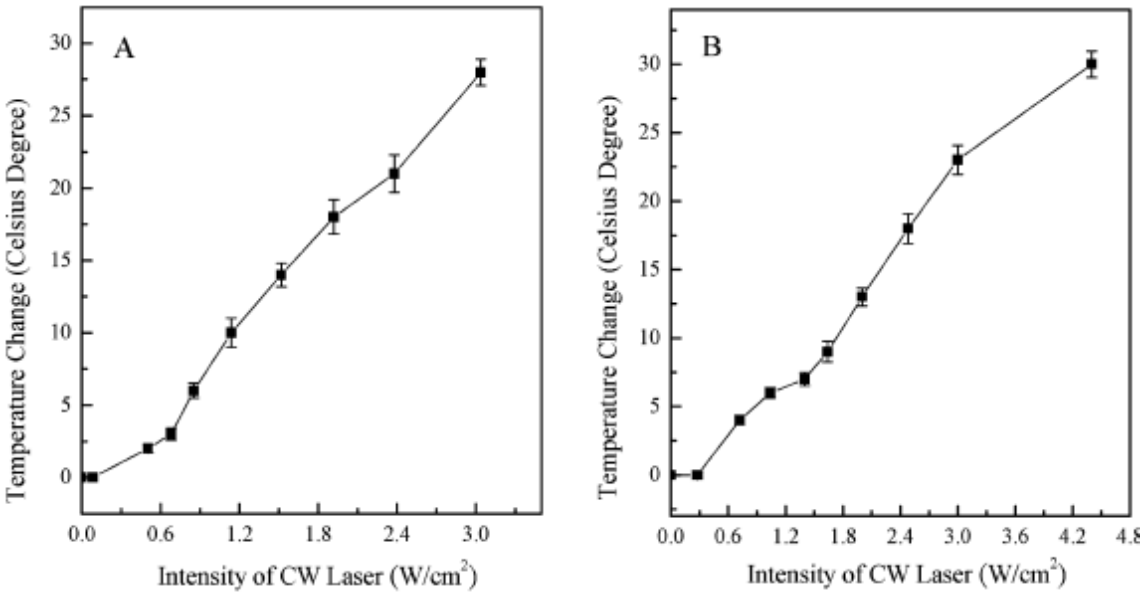

Figure 4-9: Measured temperature plotted as a function of intensity of the laser used. (A) Gold nanospheres (OD λ=514 nm=3.0, 2.0 mL) illuminated by the Argon laser (514 nm). (B) Gold nanocages (OD λ=808 nm)=3.0, 2.0 mL) illuminated by the diode laser (808 nm). Each measurement of temperature change is taken after 20 min fixed strength of laser irradiation.

4.4 Conclusions

The above observations suggest the potential use of plasmonic nanoparticle as photothermal heating elements. Instead of using the cumbersome technique of a thermostatic water bath or an oil bath, the reaction temperature can be controlled by a cw (continuous wavelength) laser beam or a strong cw Xenon or mercury lamp. The total heat mass generation in the thermostatic method is larger than the photothermal one because the heat transfer loss from the bulk equipment to catalysts is larger than photothermal systems which the plasmonic nanoparticle heats inside the solutions.
In this system, gold nanoparticles served not only as a catalyst but also as heating source to increase the reaction solution temperature. The properties of gold nanospheres or gold nanocages remain unchanged with long time exposure to the laser. Other reactions in

which gold is not a catalyst can also use gold nanoparticles as photothermal heaters when placed in a jacket surrounding the reaction mixtures. This technique can be used for accelerating thermal or photochemical reactions. The application of this conclusion in industry could be useful in heating and accelerating product formation by using solar energy and recyclable gold nanoparticles.

4.5 References

[1] Kelly, K. L.; Coronado, E.; Zhao, L. L.; Schatz, G. C. *J. Phys. Chem. B* **2003**, *107*, 668.

[2] Kreibig, U.; Vollmer, M. Optical Properties of Metal Clusters, Springer, Berlin, 1995.

[3] Link, S.; El-Sayed, M. A. *Annu. Rev. Phys. Chem*. **2003**, *54*, 331.

[4] Moores, A.; Goettmann, F. *New J. Chem*. **2006**, *30*, 1121.

[5] Ghosh, S. K.; Pal, T. *Chem. Rev.* **2007**, *107*, 4797.

[6] Jain, P. K.; Huang, W.; El-Sayed, M. A. *Nano Lett.* **2007**, *7*, 2080.

[7] Krenn, J. R.; Dereux, A.; Weeber, J. C.; Bourillot, E.; Lacoute, Y.; Coudonnet, J. P. *Phys. Rev. Lett*. **1999**, *82*, 2590.

[8] Pendry, J. B. *Science* **1999**, *285*, 1687.

[9] Rosi, N. L.; Mirkin, C. A. *Chem. Rev.* **2005**, *105*, 1547.

[10] Mirkin, C. A.; Letsinger, R. L.; Mucic, R. C.; Storhoff, J. J. *Nature* **1996**, *382*, 607.

[11] Lin, S. Y.; Liu, S. W.; Lin, C. M.; Chen, C. H. *Anal. Chem.* **2002**, *74*, 330.

[12] Sun, Y. G.; Xia, Y. N. *Anal. Chem*. **2002**, *74*, 5297.

[13] Gersten, J. I.; Nitzan, A. *J. Chem. Phys*. **1980**, *73*, 3023.

[14] Nie, S.; Emory, S. R. *Science* **1997**, *275*, 1102.

[15] Baker, G. A.; Moore, D. S. *Anal. Bioanal. Chem*. **2005**, *382*, 1751.

[16] Hu, M.; Chen, J.; Li, Z.-Y.; Au, L.; Hartland, G.. V.; Li, X.; Marquez, M.; Xia, Y. *Chem. Soc. Rev*. **2006**, *35*, 1084.

[17] Jain, P. K.; Huang, X.; El-Sayed, I. H.; El-Sayed, M. A. *Acc. Chem. Res.* **2008**, *41*, 1578.

[18] Hirsch, L. R.; Stafford, R. J.; Bankson, J. A.; Sershen, S. R.; Rivera, B.; Price, R. E.; Hazle, J. D.; Halas, N. J.; West, J. L. *Proc. Natl. Acad. Sci*. **2003**, *100*, 13549.

[19] Dickerson, E. B.; Dreaden, E. C.; Huang, X.; El-Sayed, I. H.; Chu, H.; Pushpanketh, S.; McDonald, J. F.; El-Sayed, M. A. *Cancer Lett*. **2008**, *269*, 57.

[20] Liu, H.; Chen, D.; Tang, F.; Du, G.; Li, L.; Meng, X.; Liang, W.; Zhang, Y.; Teng, X.; Li, Y. *Nanotechnology* **2008**, *19*, 455101.

[21] Neretina, S.; Qian, W.; Dreaden, E. C.; Hughes, R. A.; Preston, J. S.; Mascher, P.; El-Sayed, M. A. *Nano Lett*. **2008**, *8*, 2410.

[22] Biesso, A.; Qian, W.; El-Sayed, M. A. *J. Am. Chem. Soc*. **2008**, *130*, 3258.

[23] Narayanan, R.; El-Sayed, M. A. *J. Phys. Chem. B* **2003**, *107*, 12416.

[24] Narayanan, R.; El-Sayed, M. A. *Nano Lett.* **2004**, *4*, 1343.

[25] Narayanan, R.; El-Sayed, M. A. *J. Phys. Chem. B* **2005**, *109*, 18460.

[26] Kelly, K. L.; Coronado, E.; Zhao, L. L.; Schatz, G. C. *J. Phys. Chem. B* **2003**, *107*, 668.

[27] Bauer, C.; Abid, J.-P.; Girault, H. H. *J. Chem. Phys*. **2004**, *120*, 9302.

[28] Novo, C.; Funston, A. M.; Mulvaney, P. *Nature Nanotechnology* **2008**, *3*, 598.

[29] Gobin, A. M.; Lee, M. H.; Halas, N. J.; James, W. D.; Drezek, R. A.; West, J. L. *Nano Lett.* **2007**, *7*, 1929.

[30] Tabor, C.; Qian, W.; El-Sayed, M. A. *J. Phys. Chem.* **2007**, *111*, 8934.

[31] Wiley, B.; Herricks, T.; Sun, Y.; Xia, Y. *Nano Lett*. **2004**, *4*, 1733.

[32] Sun, Y.; Xia, Y. *Science* **2002**, *298*, 2176.

[33] Freund, P. L.; Spiro, M. *J. Phys. Chem.* **1985**, *89*, 1074.

[34] Turkevich, J.; Stevenson, P. C.; Hiller, *J. Discuss. Faraday Soc*. **1951**, *11*, 55.

[35] Aylmore, M. G.; Muir, D. M. *Miner. Eng*. **2001**, *14*, 135.

[36] Arslan, F.; Sayiner, B. Miner.l *Process Extr. Metal. Rev*. **2008**, *39*, 68.

[37] Link, S.; El-Sayed, M. A. *Int. Rev. Phys. Chem*. **2000**, *19*, 409.

[38] Govorov, A. O.; Zhang, W.; Skeini, T.; Richardson, H.; Lee, J.; Kotov, N. A. *Nanoscale Res. Lett.* **2006**, *1*, 84.

[39] Lee, K.-S.; El-Sayed, M. A. *J. Phys. Chem. B* **2005**, *109*, 20331.

[40] Jain, P. K.; Lee, K. S.; El-Sayed, I. H.; El-Sayed, M. A. *J. Phys. Chem. B* **2006**, *110*, 7238.

CHAPTER 5

BACTERIORHODOPSIN-BASED PHOTO-ELECTROCHEMICAL CELL

Abstract

A simple solution-based electrochemical cell has been constructed and successfully employed in the detection of the photoelectric response upon photoexcitation of bacteriorhodopsin (bR) without external bias. Commercially-available indium tin oxide (ITO) glasses served as the optical windows and electrodes. Small amounts of bR suspensions were utilized as the photovoltaic medium to generate the proton gradient between two half-cells separated by a molecular porous membrane. Continuous broadband visible light ($\lambda > 380$ nm) and a short-pulse 532-nm laser were employed for the photoexcitation of bR. Upon the modulated cw broadband irradiation, an instantaneous rise and decay of the current was observed. Our observations of the pH-dependent photocurrent are consistent with previous reports in a bR thin film configuration, which also showed a polarity inversion at pH 5–6. This is due to the change of the priority of the proton release and proton uptake in the photocycle of bR. Studies on the ionic strength effect were also carried out at different KCl concentrations, which resulted in the acceleration of the rise and decay of the photoelectric response. This was accompanied by a decrease in the stationary photocurrent at higher KCl concentrations in the broadband excitation experiments. The solution-based electrochemical cell uses aqueous medium, which is required for the completion of the bR proton pumping function. Due to the generation of the stationary current, it is advantageous to convert solar energy into electricity without the need of film-based photovoltaic devices with external bias.

5.1 Introduction

Recently, the need for alternative and sustainable energy sources has been discussed widely. In terms of the natural photosynthesis systems, bacteriorhodopsin (bR) has been regarded as a candidate for solar energy conversion due to its proton pumping function upon photoexcitation in the visible region. Bacteriorhodopsin, the only protein in the purple membrane (PM) of *Halobacterium salinarium*, is composed of seven helices and one interior retinal chromophore in a two-dimensional hexagonal structure.[1-3] The photoexcitation of bR initiates a photocycle, which involves a proton transport process and a series of intermediates that can be characterized spectrally.[4,5]

$$bR \xrightarrow{h} K \rightarrow L \rightarrow M1 \rightarrow M2 \rightarrow N \rightarrow O \rightarrow bR \quad (1)$$

The isomerization of the retinal occurs in the transition of bR→K upon photoexcitation. Following isomerization, a series of proton transport through the bR protein, involving several amino acid residues and internalH_2O, has been reported.[4-6] The proton release complex (PRC) is believed to be composed of Arg82, Glu204, Glu194, and internal H_2O.[7,8] The proton migration process has been investigated using a pH-sensitive dye as an indicator, due to its transient absorption change in different protonated conditions [9-12] and time-resolved infrared spectroscopic methods.[6,8] Recent studies showed that the PRC deprotonation, corresponding to the proton release from bR, does not take place in the L→M transition. The PRC deprotonation is delayed relatively to Asp85 protonation and occurred in the M substates also demonstrated that proton release occurred in the transition of M substates, followed by the proton reuptake, which occurred in the transition of N→O when the environmental pH is larger than the p*K*a of PRC.[6,11] With an environmental pH smaller than the p*K*a of PRC, proton uptake occurred in the transition of N→O, which is prior to the proton release in the transition of O→bR.

Upon photoexcitation of bR, the proton transport can bring about an electric response. In most bR-based photovoltaic devices, the photoelectric response has been investigated in a bR thin film configuration.[13] The notion was to establish the anisotropy of bR between the reference and working electrodes, resulting in non-averaged signals. Miscellaneous methods, such as Langmuir–Blodgett deposition, electric field sedimentation, self-assembled monolayer by chemisorption layer-by-layer assembly, and antigen–antibody molecular recognition, have been employed to immobilize and orient bR on thin films.[14-17] Due to the short distance between the bR thin film and electrode, the photo-induced electric signal can be recorded as an electromotive force or current. Three components make up this photoelectric response.[10,18] Upon short-pulse irradiation, the first fast photoelectric response, B1 (1.7 ps), reflects the isomerization of the chromophore in the first event of the photocycle, coupled with Arg82 motion.[19-22] A consequential B2 component is presumably attributed to the transition of L→M.[10] The polarity of B1 and B2 are not affected by pH. Over longer times (milliseconds), the B3 component has been observed.[23-26] Upon long-duration modulated broadband irradiation, D1 and D2 have been observed when incident light is turned on and off, respectively.[23,24] B3 and D1 were believed to occur upon the net proton release and uptake through the protein.[27,28] The polarity and rise of B3 and D1 components can be altered with changing the.[10,23,27] It is well-correlated to the abovementioned mechanism that the proton release occurred prior to the proton reuptake at pH> 5.8, whereas the opposite proton transport priority at pH< 5.8.[11]

In most bR-based thin-film devices, the observed photovoltage values are in the range of 0.2–15mV per bR monolayer and stationary photocurrent values are less than 40 $pAcm^{-2}$ per bR monolayer, in the presence of an external bias.[13,29] Horn *et al* developed a solid-supported, bR-deposited, black lipid membrane and obtained a relatively large stationary photocurrent density of 3 nA cm^{-2} (about 2% in comparison with the peak current) without applying an external bias.[30] The photoexcitation of a polymer-

immobilized bR film gave rise to an extremely high current density of 120 μAcm^{-2} in the presence of a 20V external bias.[31] However, the dehydrated environment will result in the accumulation of M intermediate, which slows down or inhibits the proton pumping cycle.[32] A possible bias-induced electron movement in the circuit can be attributed to the highly improved photoelectric response.

In this work, studies of the photo-induced electric response of bR have been carried out with an easily-constructed electrochemical cell in aqueous solution. The working half-cell is composed of PM suspensions, without defining the electrode polarity by applying an external bias. The indium tin oxide glasses served both as optical windows and electrodes. The pH-dependence and ionic strength effects on the photocurrent have been studied and found to be consistent with previous reports.[11,23,27] Our method is advantageous in utilizing bR for solar energy conversion due to the convenient method used to make the electrochemical cells. In addition, our design offers an appropriate tool to study the excitation of other photo-induced ionic pumping system, such as the chloride pump of halorhodopsin.[33]

5.2 Experimental Section

Preparation of Bacteriorhodopsin

A standard method for preparation of native bR in the purple membrane from H. salinarium was described by Oesterhelt *et al.*[34] Strain S-9, with a higher PM yield and an absence of carotenoids, was chosen for these experiments.[35] The concentrated PM suspension was stored at −10 ◦C for further use. Eight buffer solutions were used for subsequent mixing with bR: pH 9 (100mM, boric acid, BDH), pH 8 and 7(100mM, phosphate, BDH), pH 6 (100mM, citrate, TEKnova), pH 5, 4 and 3 (100mM, phthalate, BDH), and pH 2 (100mM, HCl/glycine, VWR). Concentrations were controlled such that the buffer solution and the bR suspension remained at 1mM and 26 µM, respectively, in

each sample. The mixtures were irradiated with white light to generate light-adapted bR. KCl (Fisher Scientific Co., laboratory grade) was used to study the ionic strength effect on the photocurrent.

Design of bR-based Electrochemical Cell

Modified from the electrochemical cell design by Horn *et al*[25] and Robertson *et al*,[27] a non-bR film configuration was constructed for the electrochemical cell, as shown in Fig. 5-1(A). The working electrodes are two pieces of 25mm×50mm×1.1mm soda–lime glass, coated on one surface with transparent indium tin oxide (ITO) (150 nm thickness) exhibiting a surface resistance of 4–8Ω (CG-40IN-1115, Delta Technologies). An O-ring (7.6 mm inside diameter, 1.8 mm cross section), placed on the coating-up ITO glass (mounted on the bottom), was constructed to serve as the working half-cell, in which the mixture of bR and buffer solution was added (~80 μL). A Teflon spacer (7 mm inside diameter, 2 mm thickness), adherent to a molecular porous membrane (MWCO: 12,000–14,000, Spectrum Medical Industries) on one side, was used to separate the half-cells and was placed in contact with the working half-cell. The buffer solution of equivalent concentration was added into the volume defined by the Teflon spacer (~80 μL) to serve as the reference half-cell and placed in contact with the coating-up ITO glass (placed on the top). No external bias was applied in any measurements.

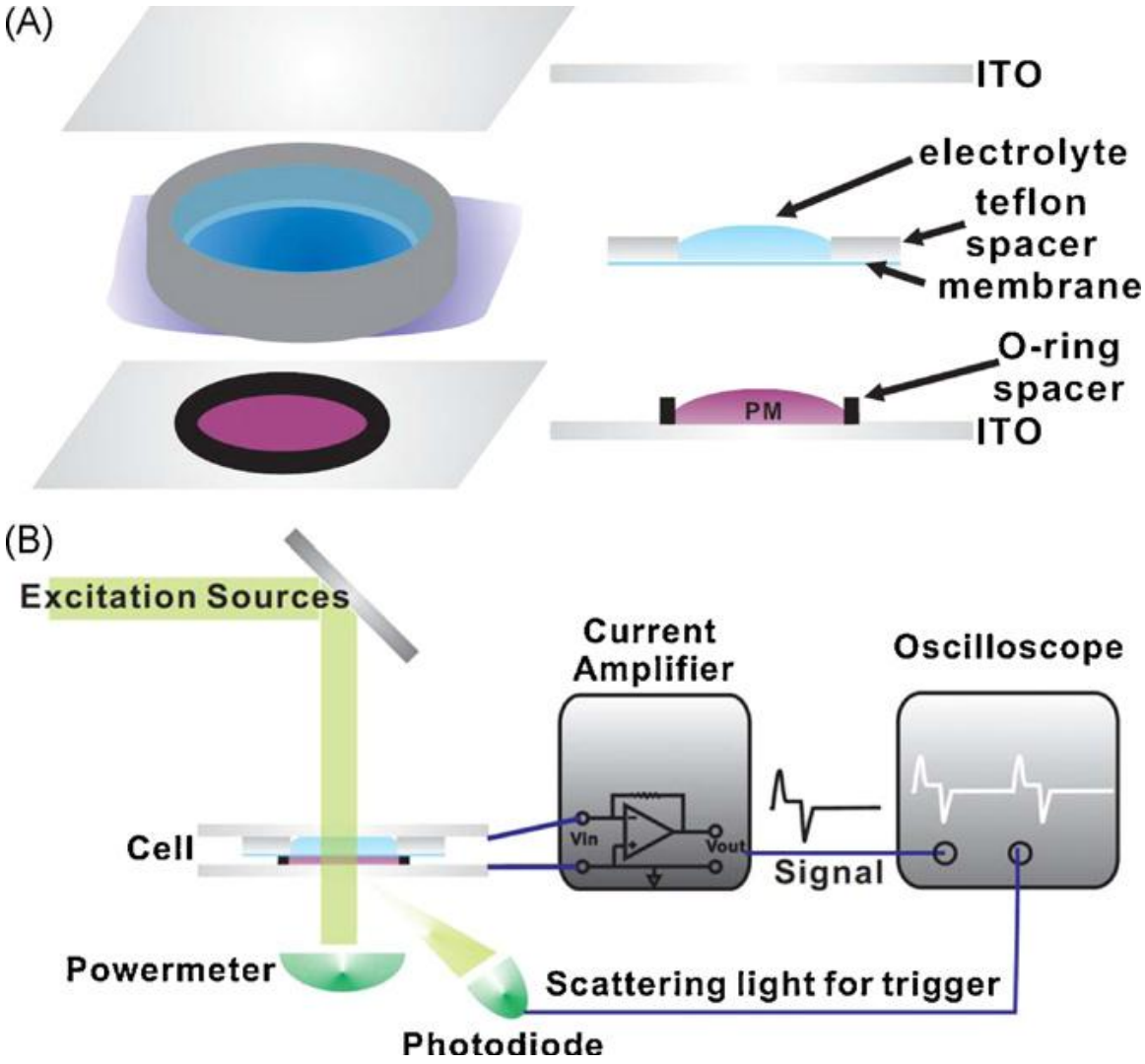

Figure 5-1: (A) The components used in assembling the electrochemical cell. (B) The experimental setup for measuring the photocurrent produced by either modulated cw light (Xenon lamp) or 532-nm pulsed nanosecond laser.

Photocurrent Measurements

The photocurrent measurements were carried out by using a pulsed laser and modulated cw broadband light as the excitation sources. The experimental setup is schemed in Fig. 5-1(B). Pulsed excitation was carried out using a frequency-doubled Nd:YAG laser (GCR-2, Spectral Physics) irradiating at 532 nm with a bandwidth of 10 ns, a repetition rate of 10 Hz, and a flux of 2.5 mJ cm^{-2} within 5% energy fluctuation. The modulated broadband excitation was introduced from a cw xenon lamp (UXL-75X,

Ushio), powered externally (LPS-220, PTI), through an optical fiber (long-pass at > 380 nm), and modulated with an external shutter (04IES001, Melles Griot), actuated electronically at a 0.7 Hz repetition rate, a 2 ms full-slew time and a 0.47 s exposure time. The current signal generated by the electrochemical cell was further amplified by an external current amplifier (Model-428, Keithley Instruments Inc.). The scattering light was collected with a home-made photodiode, used for triggering the record and storage of the waveform by a 500-MHz transient digitizer (9350A, LeCroy). Generally, 300 rounds and 1500 shots were averaged in broadband and pulsed excitation, respectively. A power-meter (30A, Ophir) was also equipped to monitor the instantaneous incident excitation energy.

5.3 Results and Discussions

Excitation with Different Light Sources

Upon pulsed 532-nm laser excitation of bR at pH 7, a transient photoelectric response is observed (Fig. 5-2A). An immediate photocurrent reaches a maximum in about 2ms decaying to the opposite polarity, followed by a slow recovery to zero. Upon irradiation of bR with a modulated cw broadband source, the photocurrent waveforms are recorded (Fig. 5-2B). The black and red traces represent the current upon irradiation with incident wavelengths 410–900 nm and 530–900 nm, respectively. When the light is switched on, an instantaneous electric response was observed, which reaches a maximum in about 7ms, followed by a stationary offset which retains ~6% intensity. When the light is switched off, an opposite current polarity is observed, followed by a slow recovery back to zero. It should be noted that the transient maximum current is larger when exciting bR with incident wavelengths including the blue region. Inset (i) of Fig. 5-2B

shows the normalized current temporal profiles and no significant difference was observed.

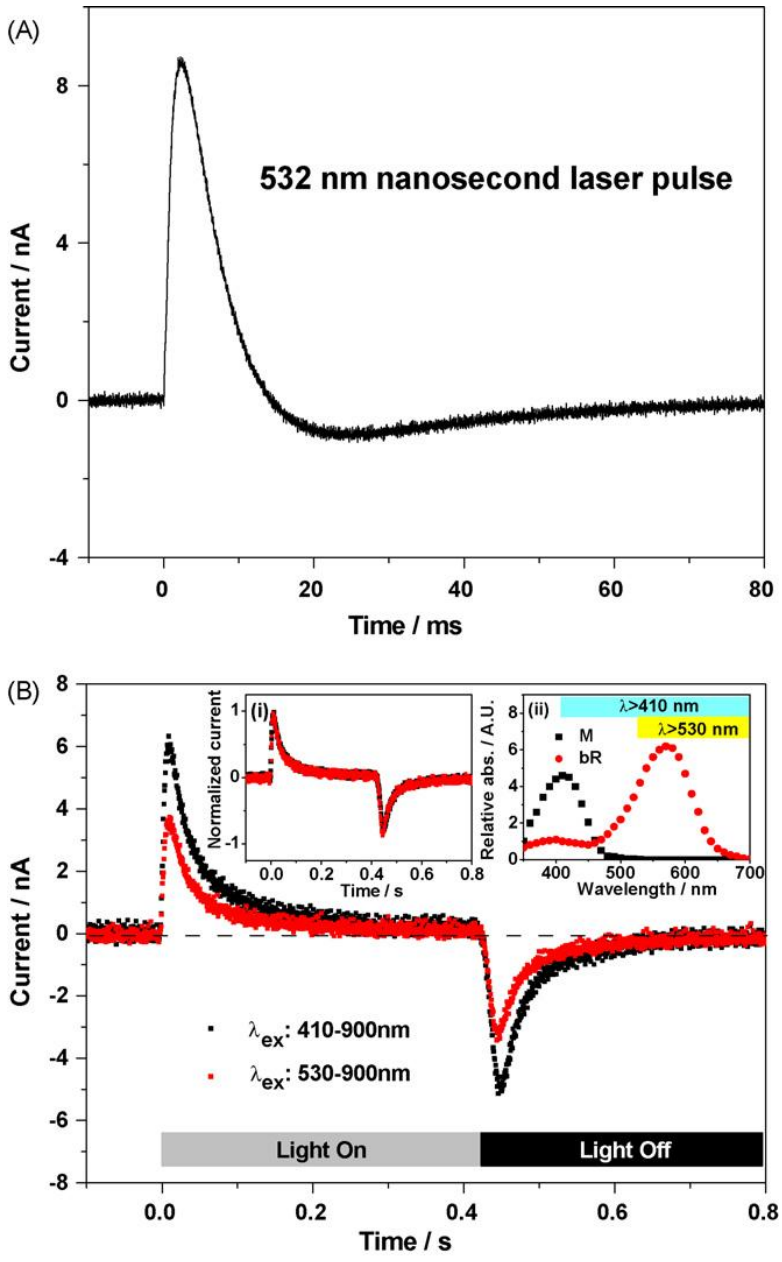

Figure 5-2: Photocurrent upon excitation of bR either with 532-nm ns-laser irradiation (A) and modulated cw broadband light (B). Inset (i) represents the normalized current signal in (B). Inset (ii) is a re-plot of the absorption spectra of bR and the M intermediate. The color blocks indicate the different incident broadband excitations.

Upon excitation of bR, the proton release and reuptake of the PRC occurring in the working half-cell results in the proton gradient difference between the two half-cells. Non-P-V work (W) is assumed to pour into the system and can be expressed as:

$$-W = -\Delta G = nF\varepsilon = RT \ln \frac{[H^+]br.cell}{[H^+]_{ref.cell}} \qquad (2)$$

where F, E, R, and T represent Faraday constant, electric potential, Avogadro constant, and ambient temperature, respectively. Protons serve as the carrier to generate the current signals. The bR electrochemical cell is regarded as the parallel connection of a transient battery and a resistance. In most conventional mechanism of the bR photocycle, the proton release occurs in the transition of M substates and the uptake from bR occurs in the transition of N→O at pH 7, respectively.[11] In comparison with our observed photoelectric response, the pulsed irradiation initiated proton generation, corresponding to the positive polarity. Afterward, the proton reuptake by bR occurred and resulted in the reduction of the transient proton concentration, which corresponds to the observed current amplitude decrease. During the proton release and uptake, some ionic species also moved through the molecular porous membrane between the two half-cells in order to neutralize the local positive charge accumulation. A slight recovery current in opposite polarity was observed when the proton migration process finished.

A similar phenomenon was observed by exposing bR to long duration irradiation. An instantaneous rise and decay correlates to the proton release and uptake through the protein. A stationary current during broadband exposure was observed. The current amplitude is related to the transient proton concentration, which can be described as:

$$bR + h\upsilon \xrightarrow{k_1, proton\ release} H^+ \xrightarrow{k_{-1}, proton\ uptake} bR \qquad (3)$$

k_1 and k_{-1} can be regarded as the simplified rate coefficients for proton release and uptake, respectively. The differential equation for proton concentration can be expressed as:

$$\frac{d[H^+]}{dt} = k_1[bR] \quad - k_{-1}[H^+] \qquad (4)$$

Upon long duration exposure, the proton concentration can reach a steady-state. Applying the steady-state approximation, $d[H^+]/dt = 0$, the steady-state proton concentration, $[H^+]_{ss}$, can be expressed as:

$$[H^+]_{ss} = \frac{k_1}{k_{-1}} bR \qquad (5)$$

The steady-state proton concentration gives rise to the stationary photocurrent. This concept can be applied to long-term solar energy transfer materials. When the light is switched off, the oppositely-polar recovery current was observed afterward. This mechanism is discussed in next section.

Inset (ii) of Fig. 5-2B shows the spectra of the M state and bR, as well as the different incident broadband excitations used. Upon excitation with different broadband wavelengths, the current amplitudes are different, but the waveforms of the temporal profiles (inset i) did not show significant differences. The excitation wavelengths of 410–900nm include photons that excite both bR (570 nm) and the M state (412 nm). It is known that strong absorption of M_{412} species can short-cut the photocycle by introducing the transition of the M intermediate back into bR, through a 13-cis to all-trans retinal isomerization, followed by reprotonation of the Schiff base from Asp85.[36] The bypass will not change the net proton release and uptake profiles, but will increase the current amplitude. This short-cut of the photocycle makes the transition of bR→M_{412}→bR more frequent and results in the increase of the rate constant k1, as well as the current amplitude.

Photocurrent upon excitation of bR with nanosecond pulse and modulated broadband light at different pHs

The photocurrent temporal profiles were recorded upon excitation of bR with a 532-nm pulse laser (Fig. 5-3A) and modulated broadband light ($\lambda > 380$ nm, Fig. 5-3B) at different pHs, as plotted in three-dimension and contour. The peak current (I_{max}) versus pH is summarized in Fig. 5-3C. The corresponding rise time of the current to reach its maximum (τ_{max}) is also summarized in Fig. 5-3D. The solid and open circles indicate the photoelectric signal generated upon excitation of bR with a 532-nm pulse and modulated broadband light, respectively. Upon both excitations, a significant current polarity inversion was observed at pH 5–6. This is consistent with previous reports.[24,27,37] The polarity inversion is due to the protonated state of the proton release complex in the M intermediate.[11] The priority of the proton release and uptake was altered at a medium pH of 5.8. This is the pKa of the proton release group complex involved in the proton pumping cycle. In addition, a significant difference of τ_{max} is observed at high and low pH regions. Previous reports focused on the relationship of peak current and the surrounding pH; addressing the kinetics of the intermediate transition, τ_{max} has rarely been discussed. As a result, the peak current and the corresponding duration will be discussed for different pH ranges.

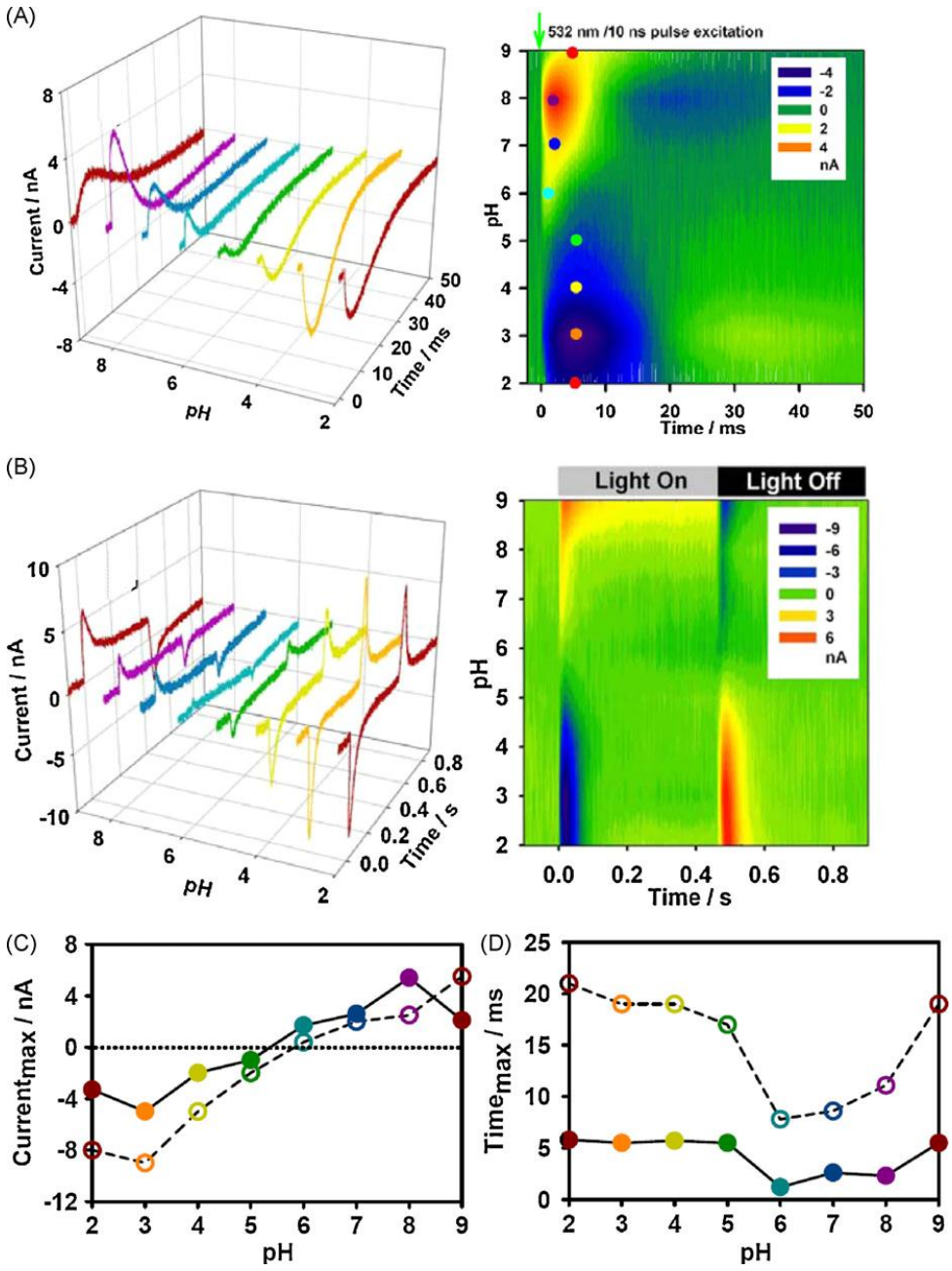

Figure 5-3: pH-dependent photocurrent polarity inversion results: the photo-induced current upon pulsed laser excitation at 532nm (A) and modulated cw excitation (B) in the pH range 2–9. Left and right figures represent the 3-D plot and contour plot. The current maximum (Imax) in (C) and the time needed to reach the maximal current (τ_{max}) in (D) show that the current polarity is inverted in the pH range between 5 and 6, which corresponds to the pKa value of the proton release complex. The solid and open circles indicate the photoelectric signal generated upon excitation of bR with a 532-nm pulse and modulated broadband light, respectively. The concentrations of buffer solutions of different pHs were kept at 1mM while the concentration of bR was kept at 26 µM.

Environmental pH < 5.8

Zimányi *et al.* have demonstrated that the proton uptake occurred in the transition of N→O, which is prior to the proton release in the transition O→bR, at pH< 5.8.[11] Upon long-duration irradiation, the analysis of the current transport is schemed in Fig. 5-4. The overall electric response is due to the proton chemical potential difference between the bR and the reference half-cells, as shown in purple line in the right half of Fig. 5-4A. In the half-cell containing bR at pH< 5.8 (right half of Fig. 5-4B), the proton uptake gave rise to the relatively negative polarity of the photoelectric response (dotted green line) when the cw light is switched on. Concurrent proton release occurred thereafter, contributing to the relatively positive polarity (dashed green line) and a resultant decrease of the transient proton concentration difference (red line). The slightly induced ion movement should be taken into consideration during the proton concentration modulation in the reference half-cell (right half of Fig. 5-4C).When the cw light is switched off, the proton uptake stopped, followed by a delayed proton release. The electric response show an opposite polarity, compared to the light-on event. The rise time and amplitude of the photoelectric response are dominated by environmental pH. Balashov *et al*. and Lu *et al*. have demonstrated that the rate of the N→O transition at pH< 6 is not dependent on the pH, whereas the rate of the O→bR transition decreased at low pH, leading to a transient accumulated population of the O intermediate.[37,38] Upon the excitation of bR with modulated broadband light at pH< 6, the Imax increased when pH decreased (Fig. 5-3C, open circles). In addition, the slow decay of O at low pH, corresponding to the slow proton release, also prolonged the max (Fig. 5-3D). Our observation is consistent with the demonstrations from the kinetics viewpoint.[37,38] As for the pulse excitation, similar results of Imax are observed, but the max did not show significant difference at pH< 6, as shown in Fig. 5-3C and D, respectively. A possible explanation would be that small amounts of ions move between the two half-cells during the proton release to compensate

for the proton deficiency in the proton uptake event in the bR half-cell. The neutralization hampered information regarding τ_{max}.

Environmental pH > 5.8

When the environmental pH is higher than 5.8, the proton release to the extracellular side occurred in the interconversion of M substates, whereas the proton uptake in the transition of N→O.[11] The overall electric response is opposite to that observed at pH< 5.8. The analysis of the photoelectric response of the bR upon long-duration irradiation is shown in left half of Fig. 5-4A. In the half-cell containing bR, the proton release gave rise to a relatively positive polarity of the photoelectric response (dashed green line in the left half of Fig. 5-4B). After proton release, concurrent proton uptake occurred, contributing to the relatively negative polarity (dotted green line) and the net transient proton concentration (red line) decreases. The induced ion movement occurred simultaneously during the proton concentration modulation, as shown in the left half of Fig. 5-4C. When the cw light is switched off, proton release stops. A delayed proton uptake results in an electric response with opposite polarity, compared to the light-on event. Balashov *et al.* have demonstrated that the transitions of M1→M2 and N→O are decelerated when the pH is higher than 8.[38] Upon excitation of bR with modulated broadband light at pH> 5.8, the Imax increased with increasing pH, as shown in Fig. 5-3C (open circles). In addition, the slower rise ($M_1 \rightarrow M_2$) and the decay (N→O), at higher pH, result in the increase of max, as shown in Fig. 5-3D. As for pulse excitation, similar results for I_{max} (Fig. 5-3C, solid circles) and τ_{max} (Fig. 5-3D, solid circles) were observed.

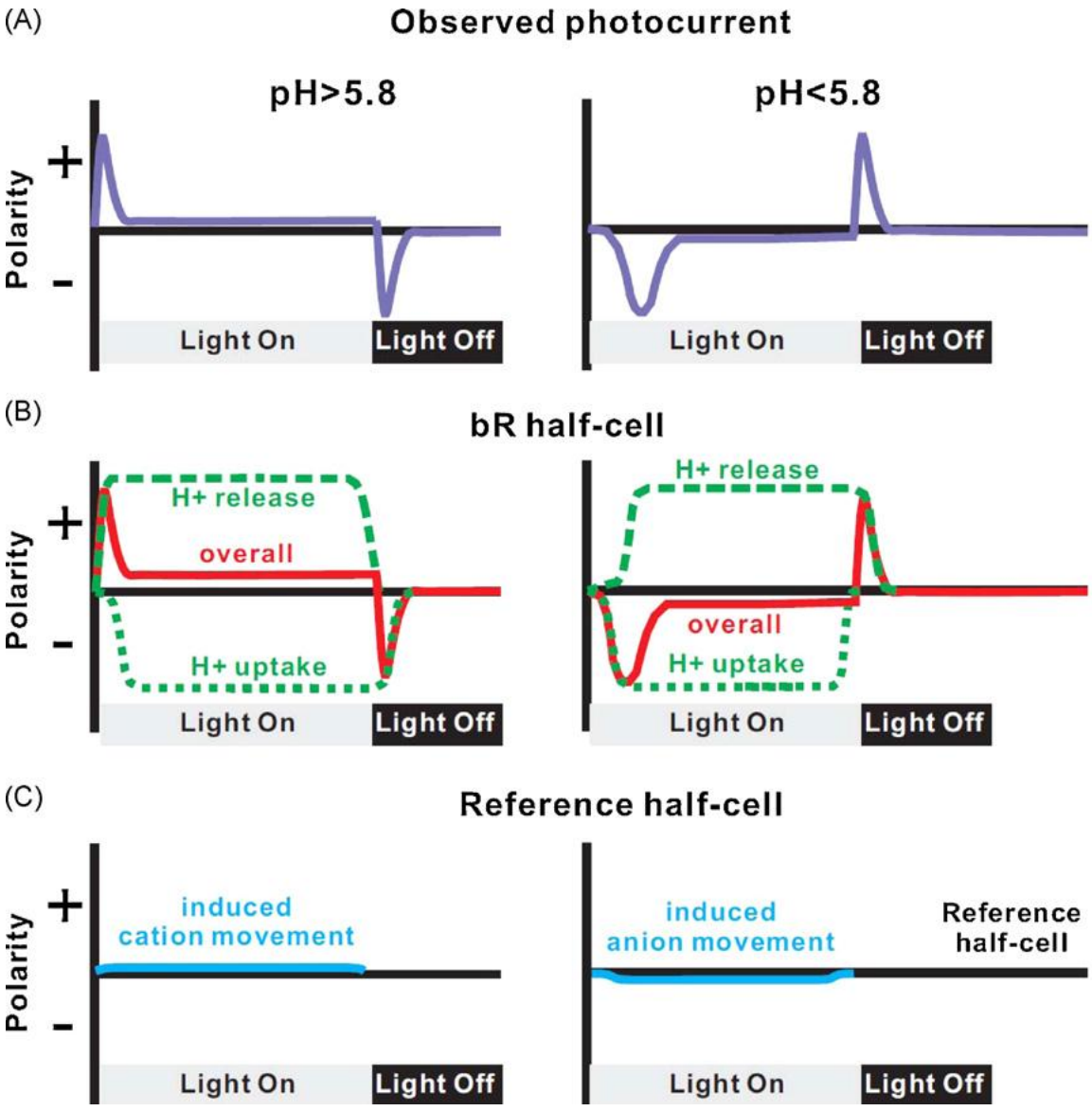

Figure 5-4: The decomposition of the observed photocurrent (A) into process occurring in the bR half-cell (B) and the reference half-cell (C) upon excitation of bR with modulated cw xenon lamp. Dashed and dotted lines represent the proton release and uptake in the proton pumping process upon photoexcitation of bR. The solid lines represent the net chemical potentials in two half-cells. The observed photocurrent results from the dynamic chemical potential difference between the bR and reference half-cells.

Ionic strength effects on photocurrent upon excitation of bR

Ionic strength studies have been carried out, using KCl as an electrolyte, in pulsed and modulated broadband excitation, as shown in Fig. 5-5A and B, respectively. Upon 532 nm pulsed excitation, the amplitude of the instantaneous electric response increased with increasing KCl concentration. The inset represents the zoom-in plot, showing that an oscillation is observed at higher KCl concentrations for a prolonged period. Upon modulated broadband light irradiation, Imax increased by adding more KCl, as shown in Fig. 5-5B. At higher KCl concentrations, an oscillation in the recovery temporal duration was observed. The inset in Fig. 5-5B represents the normalized current, showing that the rise and decay of the instantaneous response were accelerated, while the offset was diminished at higher KCl concentration. The apparent rise time constants (reciprocal of) and I_{max}, in different KCl concentration, τ_{max} are summarized in Fig. 5-5C and D, respectively. The solid and open circles represent results upon 532-nm pulsed and modulated broadband excitations, respectively. The apparent rate of the current rise is accelerated at higher KCl concentrations with both excitation methods. For a concentration of KCl > 100 mM, an asymptotic τ_{max}^{-1} value is observed upon modulated broadband excitation. This might be due to the shutter response time, which is estimated to be about 2 ms (approximately 500 s^{-1}). The effect of ionic strength has been previously considered in photocurrent experiments.[10,24] According to the explanation by Wang *et al.* proton release from the membrane surface to the bulk is delayed in the bound water layer near the membrane under low ionic strength.[24] By increasing the ionic strength, acceleration in the photoelectric response takes place. This explanation supported our observed enhancement of the rate of current generation.

I_{max} is also positively dependent on the KCl concentration, as shown in Fig. 5-5D. The electromotive force has been determined by the proton chemical potential difference in Eq. (2). By increasing the KCl concentration, the resistance of the bulk solution can be reduced, thus enhancing the current amplitude. However, the current

enhancement vanishes and an oscillation is observed at very high KCl concentrations. A possible explanation of this observation might be due to the bilayer (or multilayer) of the ionic species that exists around the purple membrane, which neutralizes the proton gradient in the vicinity of bR. The current oscillation could also be induced between different ionic layers. Moreover, the offset current is neutralized by abundant KCl around the purple membrane such that the net proton concentration difference will not be retained in long-duration exposure.

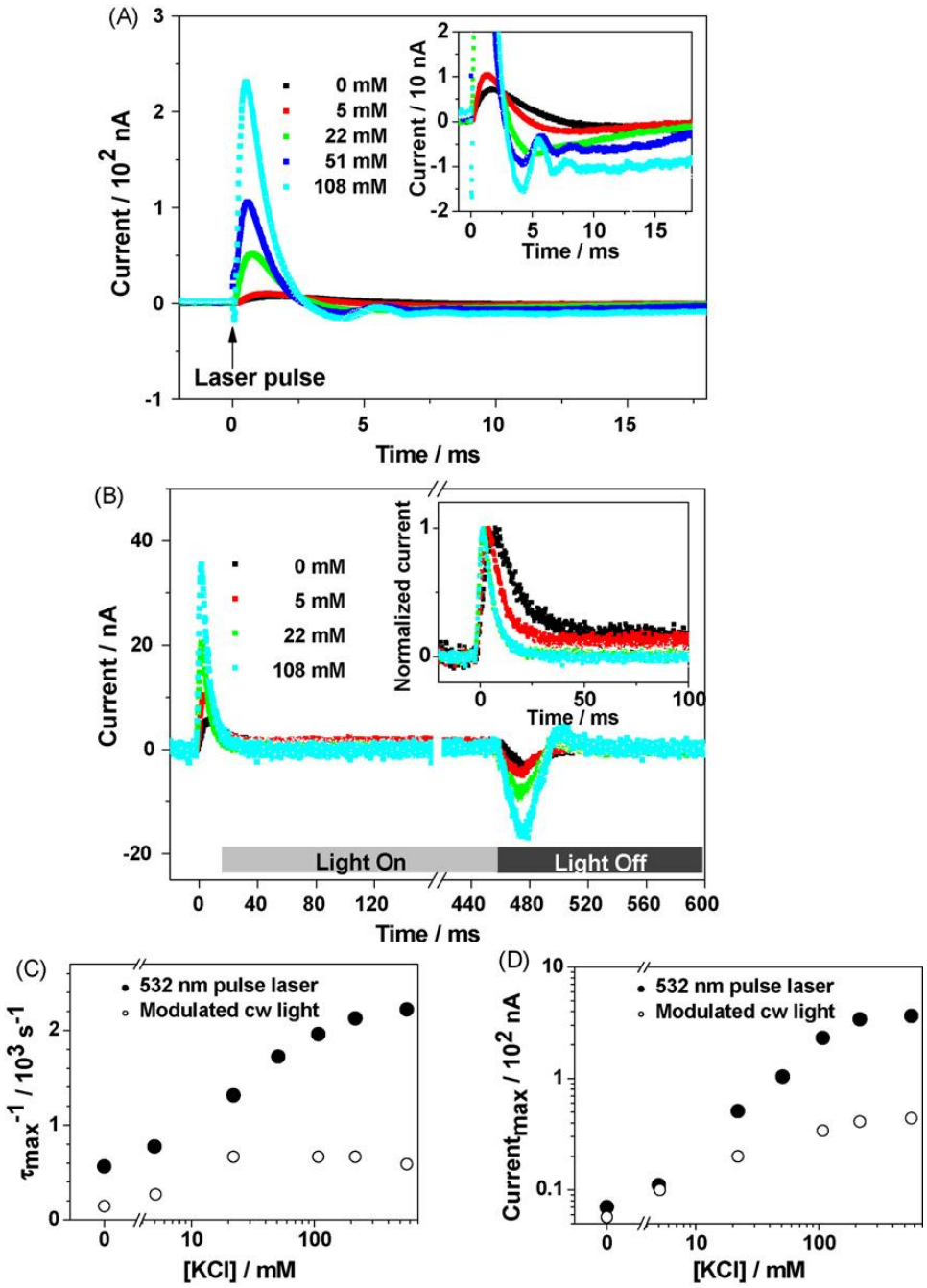

Figure 5-5: Effects of ionic strength (KCl concentration) on the observed photocurrent signals of bR upon 532-nm nanosecond laser irradiation (A) and modulated broadband cw excitation (B). The effects of ionic strength on the apparent time constant (defined as the reciprocal of τ_{max}) (C) and the photocurrent maximum (I_{max}) (D) for two types of excitation. Open circles and solid circles represent the excitation sources by modulated cw xenon lamp and 532-nm pulse laser, respectively. The concentrations of buffer solution (pH 7) and bR were kept at 1mM and 26 μM, respectively.

5.4 Conclusions

An electrochemical cell, constructed by two indium tin oxide (ITO) glasses (optical windows and electrodes) and bR suspensions (photovoltaic media), has been utilized in the detection of the photoelectric response upon photoexcitation of bR. The photo-induced proton gradient difference between the two half-cells results in an electromotive force, which drives the proton transport to serve as the carrier.

Excitation of bR at different pHs with broadband visible light ($\lambda > 380$ nm) and a short-pulse 532-nm laser brought about similar results that are consistent with previous reports. The priority of the proton release and uptake from bR was altered at pH 5–6, resulting in the corresponding current polarity change. Combining previous investigations of rate coefficients for the conversions of the intermediates in the photocycle, we successfully explained our observed pH-dependent τ_{max} and I_{max} in terms of kinetics models. Ionic strength effects were also investigated in the presence of different KCl concentrations. The rise and decay rates of the instantaneous photoelectric response are accelerated along with a current oscillation that is observed with higher KCl concentrations. The concept of the ionic bilayer supported this observation. In addition, the low ionic-strength environment is demonstrated to be beneficial to retaining stationary photocurrent upon long-duration broadband irradiation. Our easily-processed electrochemical cell offers an appropriate tool for biomolecule-based photovoltaic devices and is proposed as a candidate for the conversion of solar to electrical energy, without the need for manufacturing of film-based photovoltaic devices and external bias. Studies aimed at increasing the proton current efficiency are now in progress.

5.5 References

[1] Kelly, K. L.; Coronado, E.; Zhao, L. L.; Schatz, G. C. *J. Phys. Chem. B* **2003**, *107*, 668.

[2] Kreibig, U.; Vollmer, M. Optical Properties of Metal Clusters, Springer, Berlin, 1995.

[1] Pebay-Peyroula, E.; Rummel, G.; Rosenbusch, J.P.; Landau, E.M. *Science* **1997**, 277,1676.

[2] Essen, L.-O.; Siegert, R.; Lehmann, W.D.; Oesterhelt, D. *Proc. Natl. Acad. Sci.U.S.A.* **1998**, *95*, 11673.

[3] Luecke, H.; Richter, H.T.; Lanyi, J.K. *Science* **1998**, *280*, 1934.

[4] Balashov, S.P. *Biochim. Biophys. Acta* **2000**, 1460, 75–94.

[5] Lanyi, J.K. *Biochim. Biophys. Acta* **2006**, *1757*, 1012.

[6] Lórenz-Fonfría, V.A.; Kandori, H. *J. Am. Chem. Soc.* **2009**, *131*, 5891.

[7] Phatak, P.; Ghosh, N.; Yu, H.; Cui, Q.; Elstner, M. *Proc. Natl. Acad. Sci. U.S.A.* **2008**, *105*, 19672.

[8] Garczarek, F.; Gerwert, K. *Nature* **2006**, *439*, 109.

[9] Grzesiek, S.; Dencher, N.A. *FEBS Lett*. **1986**, *208*, 337.

[10] Liu, S.Y. *Biophys. J.* **1990**, *57*, 943.

[11] Zimányi, L.; Váró, G.; Chang, M.; Ni, B.; Needleman, R.; Lanyi, J.K. *Biochemistry* **1992**, *31*, 8535.

[12] Cao, Y.; Brown, L.S.; Sasaki, J.; Maeda, A.; Needleman, R.; Lanyi, J.K.; *Biophys. J.* **1995**, *68*, 1518.

[13] Jin, Y.; Honig, T.; Ron, I.; Friedman, N.; Sheves, M.; Cahen, D. *Chem. Soc. Rev.* **2008**, *37*, 2422.

[14] Miyasaka, T.; Koyama, K. *Thin Solid Films* **1992**, *210*, 146.

[15] Brizzolara, R.A. *Biosystems* **1995**, *35*, 137.

[16] He, J.A.; Samuelson, L.; Li, L.; Kumar, J.; Tripathy, S.K. *Langmuir* **1998**, *14*, 1674.

[17] Koyama, K.; Yamaguchi, N.; Miyasaka, T. *Science* **1994**, *265*, 762.

[18] Okajima, T.L.; Hong, F.T. *Biophys. J.* **1986**, *50*, 901.

[19] Simmeth, R.; Rayfield, G.W. *Biophys. J.* **1990**, *57*, 1099.

[20] Groma, G.I.; Szabó, G.; Váró, G. *Nature* **1984**, *305*, 557.

[21] Groma, G.I.; Hebling, J.; Ludwig, C.; Kuhl, J. *Biophys. J.* **1995**, *69*, 2060.

[22] Xu, J.; Stickrath, A.B.; Bhattacharya, P.; Nees, J.; Váró, G.; Hillebrecht, J.R.; Ren, L.; Birge, R.R. *Biophys. J.* **2003**, *85*, 1128.

[23] Wang, J.P.; Yoo, S.K.; Song, L.; El-Sayed, M.A. *J. Phys. Chem. B* **1997**, *101*, 3420.

[24] Wang, J.P.; Song, L.; Yoo, S.K.; El-Sayed, M.A. *J. Phys. Chem. B* **1997**, *101*, 10599.

[25] Keszthelyi, L.; Ormos, P. *Biophys. Chem.* **1983**, *18*, 397.

[26] Boucher, F.; Taneva, S.G.; Elouatik, S.; Déry, M.; Messaoudi, S.; Harvey-Girard, E.; Beaudoin, N. *Biophys. J.* **1996**, *70*, 948.

[27] Robertson, B.; Lukashev, E.P. *Biophys. J.* **1995**, *68*, 1507.

[28] Tamogami, J.; Kikukawa, T.; Miyauchi, S.; Muneyuki, E.; Kamo, N. *Photochem. Photobiol.* **2009**, *85*, 578.

[29] Manoj, A.G.; Narayan, K.S. *Appl. Phys. Lett*. **2003**, *83*, 3614.

[30] Horn, C.; Steinem, C. *Biophys. J*. **2005**, *89*, 1046.

[31] Zhang, L.; Zeng, T.; Cooper, K.; Claus, R.O. *Biophys. J.* **2003**, *84*, 2502.

[32] Korenstein, R.; Hess, B. *Nature* **1977**, *270*, 184.

[33] Váró, G. *Biochim. Biophys. Acta* **2000**, *1460*, 220.

[34] Oesterhelt, D.; Stoeckenius, W. *Methods Enzymol*. **1974**, *31*, 667.

[35] Lorber, B.; DeLucas, L.J. *FEBS Lett*. **1990**, *261*, 14.

[36] Hessling, B.; Herbst, J.; Rammelsberg, R.; Gerwert, K. *Biophys. J*. **1997**, *73*, 2071.

[37] Lu, T.; Li, B.F.; Jiang, L.; Rothe, U.; Bakowsky, U. *J. Chem. Soc., Faraday Trans.* **1998**, *94*, 79.

[38] Balashov, S.P.; Lu, M.; Imasheva, E.S.; Govindjee, R.; Ebrey, T.G.; Othersen III, B.; Chen, Y.; Crouch, R.K.; Menick, D.R. *Biochemistry* **1999**, *38*, 2026.

CHAPTER 6

PLASMONIC FIELD ENHANCEMENT OF THE BACTERIORHODOPSIN PHOTOCURRENT DURING ITS PROTON PUMP PHOTOCYCLE

Abstract

The proton pump photocycle of bacteriorhodopsin (bR) produces photocurrent on a micro-second time scale which is assigned to the deprotonation step forming the M_{412} intermediate. The return of the M_{412} intermediate to the bR ground state (bR_{570}) has two pathways: 1) thermally via multiple intermediates (which takes 15 ms) or 2) by a more rapid and direct process by absorbing blue light (which takes hundreds of ns). By using nanoparticles (Ag, Ag-Au, and Au NPs) having different surface plasmon resonance extinction spectra, it is found that Ag NPs whose spectrum overlaps best with the M_{412} absorption regions enhance the stationary photocurrent 15 times. This large enhancement is proposed to be due to the accelerated photoexcitation rate of the M_{412} (in the presence of plasmon field of the light in this region) as well as short-circuiting of the photocycle, increasing its duty cycles. We proposed a mechanism based on the plasmonic field enhancement of the blue light effect which bypasses the slow part of the photocycle and increases the rate of proton production and thus the observed photocurrent. We studied the AgNPs plasmonic field effect on the spectroscopy and kinetics of the bR proton pumping photocycle. We examined the blue light effect on both the recovery rate of bR and the decay rate of the M intermediate by using 532-nm short-pulsed laser excitation of bR in the presence of AgNPs and continuous-wave blue light exposure. Our observation showed that the recovery of bR and the decay of the M intermediate are both greatly accelerated in the presence of both AgNPs and blue light simultaneously. This gives support of the proposed mechanism of the enhanced proton current in the presence of

AgNPs with a plasmon band in the blue region. It was found experimentally that the 40 nm-AgNPs enhancement of the blue light effect on the decay rate is around 400 times larger than that of 8 nm-AgNPs. This is found to be in agreement with the known dependence of the plasmonic field on size and the overlap of the plasmonic extinction band with the absorption band of the M intermediates.

6.1 Introduction

Bacteriorhodopsin (bR) is the other photosynthetic system in nature and is the transmembrane protein found in *Halobacterium Salinarium*. It has been widely investigated due to its unique structural, optical, biochemical and biophysical properties and is the best studied proton pump system in biology.[1-17] The purple membrane (PM) is composed mainly of protein (75% by wt.), with the remaining 25% being composed of lipids.[1] The lattice parameters of crystallized PM have been investigated extensively and is found to be composed of seven helices and one interior retinal chromophore per bR in the two-dimensional hexagonal structure.[2-6]

The light-adapted bR exhibits an intense characteristic retinal absorption band centered at 568 nm with a corresponding extinction constant of ε_{568}=62,700 M^{-1} cm^{-1}.[7] Upon photoexcitation of bR, the corresponding transition from a ^1B_u-like ← S_0 state of the retinal chromophore gives rise to the isomerization from its all-*trans* conformation to the 13-*cis* conformation.[8] This is followed by the thermal formation of a series of spectrally distinguishable intermediates given by (Equation 1).[9]

$$\begin{aligned} \boldsymbol{bR}_{568} \xrightarrow{h\nu} \boldsymbol{I}_{460} \xrightarrow{0.5\,ps} \boldsymbol{J}_{625} \xrightarrow{3\,ps} \boldsymbol{K}_{590} \xrightarrow{\sim 2\mu s} \boldsymbol{L}_{550} \xrightarrow{50\mu s} \\ \boldsymbol{M}_{412}(\boldsymbol{M}_1 \rightarrow \boldsymbol{M}_2) \xrightarrow{1ms} \boldsymbol{N}_{560} \xrightarrow{2ms} \boldsymbol{O}_{640} \xrightarrow{8ms} \boldsymbol{bR}_{568} \end{aligned} \qquad (1)$$

Following retinal isomerization, the proton translocation from the protonated Schiff base to Asp85 gives rise to the generation of the early M state (labeled M_1). [10-12] The structures of the initial state and the early intermediates (K, L and M_1) are proposed to have one protein conformation in which the Schiff base has extracellular

accessibility.[13] A consequential proton release to the extracellular side of the protein, via Glu194, Glu204 and structure chain of water molecules, occurs during the conversion of M_1 to M_2 (labeled late M).[14,15] M_1 and M_2 are spectrally characterized by absorption at 410 nm with a corresponding extinction constant of 48,800 M^{-1} cm^{-1}.[16]

A sequential reprotonation of the Schiff base from Asp96 results in the generation of the N intermediate followed by the generation of the O intermediate involving the 13-*cis* to all-*trans* isomerization of the retinal.[17] The transition of O → bR occurs via the geometry of the protein structure to give bR_{568} and completes the photocycle (Equation 1).

$$\boldsymbol{bR}_{568} \xrightarrow{\boldsymbol{h\nu}} \boldsymbol{I}_{460} \xrightarrow{0.5\,\boldsymbol{ps}} \boldsymbol{J}_{625} \xrightarrow{3\,\boldsymbol{ps}} \boldsymbol{K}_{590} \xrightarrow{\sim 2\mu\boldsymbol{s}} \boldsymbol{L}_{550} \xrightarrow{50\mu\boldsymbol{s}} \boldsymbol{M}_{412}(\boldsymbol{M}_1 \rightarrow \boldsymbol{M}_2) \xrightarrow{1\boldsymbol{ms}} \boldsymbol{N}_{560} \xrightarrow{2\boldsymbol{ms}} \boldsymbol{O}_{640} \xrightarrow{8\boldsymbol{ms}} \boldsymbol{bR}_{568} \quad (1)$$

When the photocycle is exposed to blue light, the long-lived blue light absorbing M_{412} intermediate is converted to bR_{568} in hundreds of nanoseconds (Equation 2). This shortcut greatly reduces the conventional photocycle period which takes 15 ms.[18]

$$bR \xrightarrow{h\nu} K \rightarrow L \rightarrow M_1 or M_2 \xrightarrow{h\nu,\ 200\,ns} bR \quad (2)$$

Hessling *et al.* have demonstrated that the depletion of the M intermediate occurs upon exposure of the photocycle to an additional blue-flash light resulting in the retinal isomerization from 13-*cis* to all-*trans* in picoseconds followed by the reprotonation of the Schiff base returning to its bR state by FT-IR study.[18] Our recent study on the photocurrent from bR has indicated that the photocurrent density is greatly enhanced when the electrochemical cell is exposed to blue light in the presence of the plasmonic AgNPs in the bR solutions. The photovoltaic response is due to the change in the proton gradient. We have proposed that the plasmonic field of AgNPs greatly enhances the flux of blue photons which shortcut the photocycle by bypassing the slow paths of the conventional photocycle. This leads to a decrease in the photocycle period and increase in the rate of the proton release, resulting in the enhanced steady-state proton concentration and photocurrent.[19]

The proposed mechanism for the photocurrent enhancement suggest that the blue

light effect generated by the plasmonic field of AgNPs greatly perturbs the kinetics of the photocycle.[19] If this is indeed correct, the rates of the bR ground state recovery and that of the M intermediate decay should both be greatly accelerated by enhancing the blue light absorption rate by the plasmonic field of AgNPs. The kinetics can be studied by using time-resolved spectroscopic technique and these results can help to quantify the degree of enhanced blue light effect of the acceleration of bR photocurrent by the plasmonic field of AgNPs.

Upon the resonant excitation of the metallic nanoparticles, an intense plasmonic field is generated. The plasmonic field effect on radiative properties have been observed in many systems.[20-22] Previous publications on the plasmonic field effects on bR processes has also been investigated. [23,24] The previous reports showed that the retinal isomerization of bR in the I→J transition can be decelerated and the reprotonation of the Schiff base in the M→N transition can be accelerated in the presence of a plasmonic field upon excitation of gold nanoparticles and gold nanorods, respectively.[23,24]

In the present work, a time-resolved transient absorption technique was employed to study the plasmonic field of AgNPs with different sizes on the kinetics of bR photocycle. Due to the difference of the spectral overlap of their plasmonic resonance extinction and the M intermediate absorption, the plasmonic field enhancement of the blue photon effect will be different. These experiments can be carried out with continuous blue light exposure upon the photo-initiated bR photocycle with short-pulsed 532-nm laser. Consistent with our proposed mechanism for the photocurrent enhancement, the acceleration of the rate of the bR recovery and the M decay can be a result of bypassing the slow part of the photocycle in the presence of AgNPs and external blue photon exposure simultaneously. The dependence of the observed change in rate on the size of AgNPs is found to be consistent with the dependence of the plasmonic field on size and the degree of overlap of the plasmonic extinction spectrum of each nanoparticle with the absorption spectrum of the M intermediate.

6.2 Experimental Section

Preparation of Bacteriorhodopsin

Native bR in the PM from Halobacterium salinarium was prepared by a standard method described by Oesterhelt and Stoeckenius in 1974.[25] Strain S-9, with a higher PM yield and an absence of carotenoids, was chosen for these experiments. The PM suspension was stored at -10 ℃ for further use. The bR solutions were light adapted before the measurements.

Synthesis and Characterization of Silver Nanoparticles

The synthesis of silver nanoparticles is carried out by the reduction of silver ions (from $AgNO_3$) with sodium citrate or sodium borohydride to synthesize nanoparticles with sizes of 40 and 8 nm, respectively. Samples were freshly prepared by mixing fixed amounts of bR with different amounts of silver nanoparticle suspensions in pH=7 buffer solution (citrate, 10mM). Concentrations were controlled such that the buffer solution and bR suspension are 1.1 mM and 8.8 μM, respectively, in each sample. The concentrations of 8-nm and 40-nm AgNPs were adjusted to 75-300 nM and 0.5-2.0 nM, respectively. UV-vis spectra for all samples were acquired using a steady-state spectrometer (HR4000VG-UV-NIR, Ocean Optics) before and after the time-resolved experiments.

Photocurrent Measurement Setup

The photocurrent measurement was carried out by using a modulated cw broadband light as the excitation source (140 mW / cm^2, 10 mm). The modulated broadband excitation was introduced from a cw xenon lamp (UXL-75X, Ushio), powered externally (LPS-220, PTI), through an optical fiber (long-pass at λ>380nm), and modulated with an external shutter (04IES001, Melles Griot), actuated electronically

(04ISC001, Melles Griot), at 0.7 Hz repetition rate. Yellow long-pass optical filter (λ>500nm) is employed for excitation of bR. The current signal generated by the electrochemical cell is further amplified by an external current amplifier (Model-428, Keithley Instruments Inc.). The scattered light was collected by a home-made photodiode for triggering the record and storage by a 500-MHz transient digitizer (9350A, LeCroy). A powermeter (30A, Ophir) is also equipped to monitor the instantaneous incident excitation energy.

Kinetic and Spectroscopic Experimental Setup

The experimental setup of the short-pulsed laser excitation is drawn in Scheme 1. A frequency-doubled Nd:YAG laser (GCR-2, Spectral Physics) was employed for excitation at 532 nm with a bandwidth of 10 ns, repetition rate of 10 Hz, and a fluence of 5.5 mJ cm^{-2} within 5 % energy fluctuation. An optical fiber was employed to introduce the broadband light from a xenon lamp filtered in 350-500 nm for the excitation of silver nanoparticles, with corresponding power 0.12 W cm^{-2}. The excitation laser beam and the continuous wavelength (cw) blue light passed through the sample cell in opposite directions and overlapped in the center of the sample cell. Partial xenon lamp luminosity was employed for continuous probing combined with optical filters and a monochrometer (SpectraPro-300i, Acton Research Corporation) to define the detection wavelength at 600 or 450 nm for monitoring the bR and M intermediate, respectively. A photomultiplier tube (R1527, Hamamatsu) was utilized for collecting a photon signal and a 500-MHz transient digitizer (9350A, LeCroy) was used for data acquisition and storage. The temporal profiles of the bR recovery were recorded by probing the photon intensity modulation at 600 nm, and 3000 or 8000 laser shots were averaged depending on the signal-to-noise ratios. The intensity of the M intermediate at 450 nm is relatively weaker than that of bR state, thus the temporal profiles of the M intermediate were averaged in 10,000 laser shot. The temporally-resolved absorbance change can be derived by the

equation, $\Delta A=\log(S_t/S_o)$, where S_t and S_o represent the dc-coupled voltage in the presence and absence of the excitation laser, respectively.

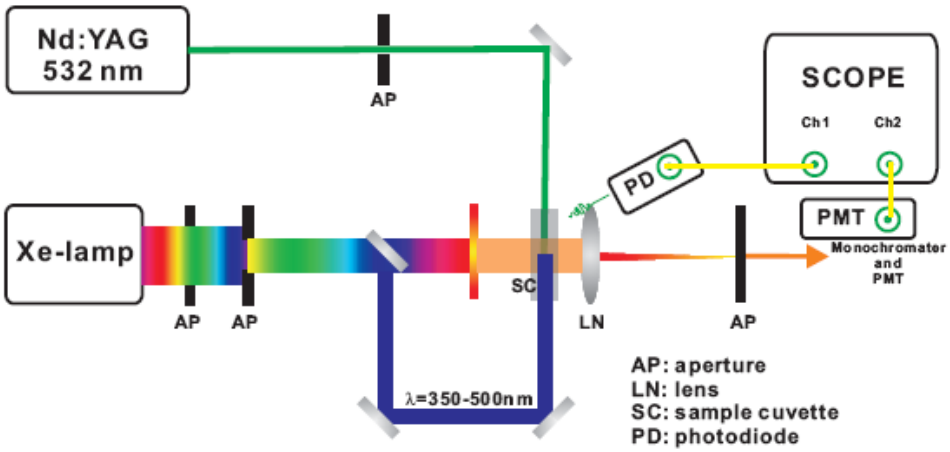

Scheme 6-1: The experimental setup of the pulsed laser (532 nm) and cw blue light (350-500 nm) photoexcitation of bR.

6.3 Results and Discussions

Plasmonic Field Enhancement of the Bacteriorhodopsin Photocurrent

The absorption of light by retinal of bR in the ground state (bR_{570}) initiates a photocycle involving a number of intermediates and drives protons across the membrane from the internal cytoplasm to the external medium, resulting in proton gradients that are used for ATP synthesis in the cell.[26,27] The protons are ejected from the cell at a rate comparable to that of the M_{412} intermediate formation.[28] By CW illumination, bR can transform light energy into electrochemical energy stored in a proton gradient across the membrane and exhibit a stationary photocurrent amplitude. This unique characteristic of bR could make it promising for applications in alternative energy. However, the photocurrent density values reported so far are around 0.2-40 pA cm^{-2} $monolayer^{-1}$ in thin film systems (Table 6-1).[29] Recently, our group was able to build a solution-based

electrochemical cell that did not require bR film preparation and external bias (details can be found in chapter 5). In this section, plasmonic field enhancement of the stationary photocurrent, orders of magnitude higher than previous reports, was observed and the mechanism involved was revealed.

Surface plasmon resonance (SPR) is an interesting optical phenomenon induced by the coupling of the incident electromagnetic wave of light with the conduction band electrons in the metal. This induces a coherent electronic oscillation of the free electrons of the metal.[30] There is a rich variety of applications utilizing the SPR property of metallic nanoparticles (NPs)[31] and our group has previously reported that retinal photoisomerization in the primary step and proton pump process of the bacteriorhodopsin were both perturbed by plasmonic fields of gold nanoparticles.[23,24] During the photocycle of bR, there are two important forms: the ground state of bacteriorhodopsin, bR_{570}, with protonated Schiff base (λmax= 570 nm) and the long lived intermediate, M_{412}, with deprotonated Schiff base (λmax= 412 nm).[32] The M_{412} can be generated following the retinal isomerization (in 70 μs) and revert to the ground bR_{570} either thermally through a number of other intermediates ($M412 \rightarrow N \rightarrow O \rightarrow bR_{570}$) in 15 ms or rapidly through photochemical process upon excitation with blue light in hundreds of nano-seconds (the known blue light effect).[33-34] The results of our experiments suggest that the surface plasmon enhancement of the M_{412} absorption (i.e. of the blue light effect) results in increasing the rate of proton release and forcing the photocycle to follow the short time bypassed path rather than the conventional thermal photocycle path of bR. The stationary photocurrent upon cw excitation of bR could be associated with the steady-state concentration of M_{412} in the $bR_{570} \rightarrow M_{412} \rightarrow bR_{570}$ photocycle.[35,36]

We synthesized Ag, Ag-Au alloy (Ag/Au=1/1), and Au NPs with similar sizes (around 30 nm) whose SPR absorption have maxima located at 425, 465, and 530 nm, respectively (Fig 6-1A). The spectral overlap between SPR band of NPs and that of M_{412}

absorption band decreased as the gold amounts added to the NPs was increased. The photocurrent measurements were carried out by our recently developed techniques.

Figure 6-1 shows the photocurrent generation from solution of bR and of bR/NPs mixtures. CW broad band irradiation ($\lambda_{incident}$> 380 nm) was used to ensure that we can excite bR at 570 nm to produce M_{412} and simultaneously excite Ag NPs at 420 nm to enhance the blue light intensity. During the light-on period, the photocurrent initially showed a sharp rise followed by decay to a near stationary photocurrent. During the light-off period, the observed inverted photocurrent was attributed to the net proton uptake of bR photocycle.

Upon excitation of pure bR, the maximum of the instantaneous rise of photocurrent density was 19.8 nA/cm^3 followed by a stationary offset of 1.6 nA /cm^3 (Fig 6-1B). When the bR solution was mixed with Ag NPs whose SPR band overlapped strongly with the M_{412} absorption band, the initial photocurrent density was increased to 45 nA/cm^3 (Fig 6-1B). The value of the stationary photocurrent density was 25 nA/cm^3 when bR was mixed with 1.2 nM of Ag NPs and it was 15 times higher than pure bR. The notable increase of photocurrent is due to the enhanced flux of blue photons by plasmonic field of Ag NPs.

When Ag-Au alloy NPs with the similar sizes and concentrations as the Ag NPs were used (Fig 6-1C), the stationary photocurrents was 11.3 nA/ cm^3 and increased by 6 times compared with the value of pure bR. This smaller enhancement was probably due to the smaller spectral overlap between the plasmonic absorption of Ag-Au NPs and the M_{412} intermediates compared that of Ag NPs. By shifting the plasmon band more towards to bR_{570} absorption by using Au NPs, a negative plasmonic field effect was observed (Fig 6-1D). There were two strong bands of Au NPs, the SPR band at long wavelength that overlapped with the bR_{570} absorption and another d-d nonplasmonic band in the blue region of the spectrum (Fig 6-1A). The bR_{570} absorption of the white light should increase as a result of its overlap with the SPR band from the Au NPs in this region;

however the blue light intensity was absorbed by the strong non plasmonic d-d absorption of the Au NPs, thus decreasing the blue light effect and the photocurrent.

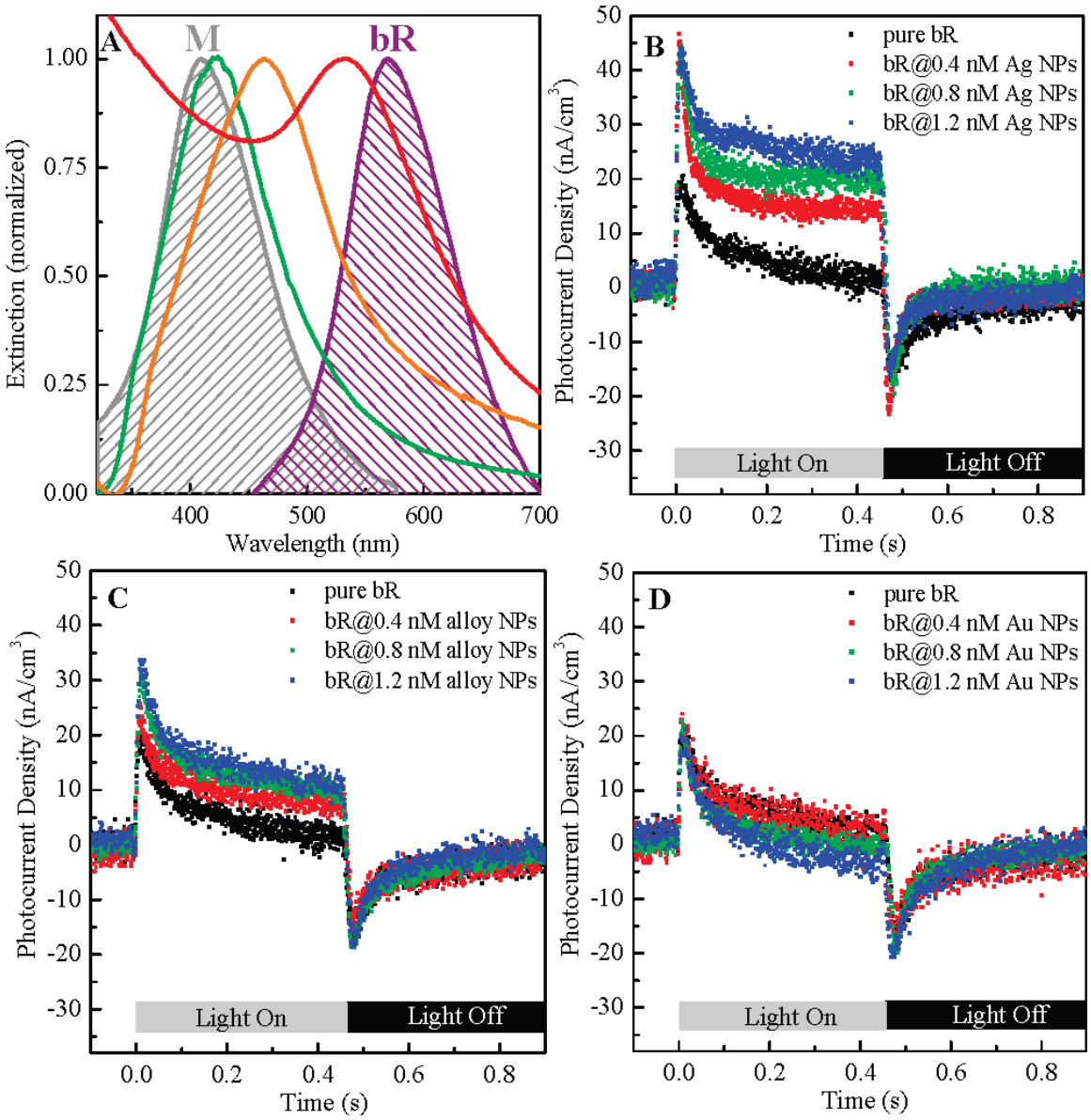

Figure 6-1: (A) Normalized SPR spectra of Ag NPs, Ag-Au alloy NPs (Ag/Au=1/1), and Au NPs was at 425 nm (green), 465 nm (orange), and 530 nm (red), respectively. The absorption contours of M state and bR state were represented by gray and violet shadows with corresponding maxima at 412 nm and 570 nm, respectively. The photocurrent density of bR observed by mixing different nanoparticles (B) Ag NPs, (C) Ag-Au alloy NPs (Ag/Au=1/1), and (D) Au NPs upon cw white light irradiation.

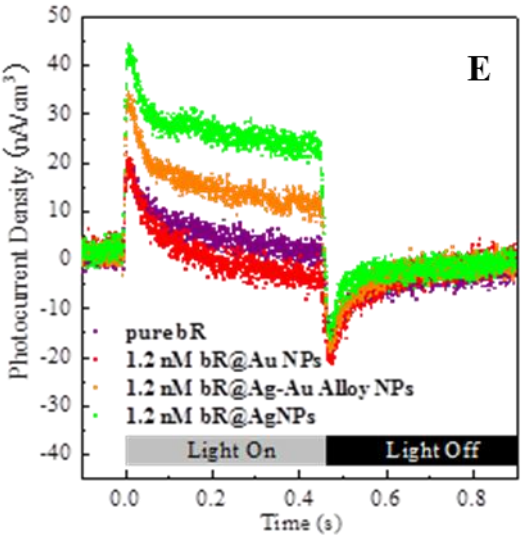

Figure 6-1: (E) The comparison of the 1.2 nM addition of Ag, Ag-Au alloy, and Au NPs. The Ag NP shows the greatest enhancement effect of photocurrent generation and the Au-Ag NP shows a mediocre effect of photocurrent enhancement. The negative effect was observed with Au NPs addition.

It is found that the plasmonic enhancement effect of Ag NPs on the absorption of the intermediate (M_{412}) is much more pronounced than that of the Au NPs on the ground state (bR_{570}). This might be due to two reasons. One is the filter effect of the blue light by the d-d absorption of Au NPs which eliminates the enhancement of the bR_{570} absorption. The second reason may be the different time scale of photocycle path; bR follows the full conventional photocycle when exciting the bR_{570}, but the blue light effect causes the bR to follow the much shorter bypass photocycle.[35,36] Both factors might explain the importance of the plasmonic field enhancement of the blue light effect to the bR photocurrent. The comparison of three nanoparticles with same concentration (1.2 nM) was shown in Figure 6-1E.

The above conclusion can be supported by the results of the following two experiments. The first experiment showed that there was no observed photocurrent enhancement of bR when 30 nm Ag NPs were used under the same intensity of cw

illumination but the blue light was filtered out ($\lambda_{incident}$> 500 nm), resulting in the absence of plasmonic field (Fig 6-2A). This suggest that the enhancement of photocurrent density was due to the exciting plasmonic effect of NPs in the blue light region, and not due to the chemical environment or the ionic concentration change by the addition of NPs. The other experiment showed that the larger the overlap between the SPR band of Ag NPs and M_{412} absorption band, the greater the photocurrent enhancement (Fig 6-2B). Ag NPs of smaller particle sizes (8 nm) were prepared whose SPR band was much narrower than the SPR band of the larger Ag NPs (30 nm) (Fig 6-3). The difference in photocurrent amplitude and photoelectric profile between the two different sizes of Ag NPs can be explained by the difference in the width of the absorption band of the Ag NPs. The absorption band of 30 nm Ag NPs overlapped better with the absorption contour of M_{412} than 8 nm Ag NPs (Fig 6-3) and the plasmonic-energy transfer was more efficient to the M_{412} under the same amount of light flux. The results of these above experiments strongly support the conclusion that the plasmonic effect of nanoparticles with extinction spectrum that overlap with the M_{412} absorption can excite M_{412} to rapidly form bR_{570} by bypassing of normal photocycle. This increases the duty cycles of the proton release and thus the photocurrent density.

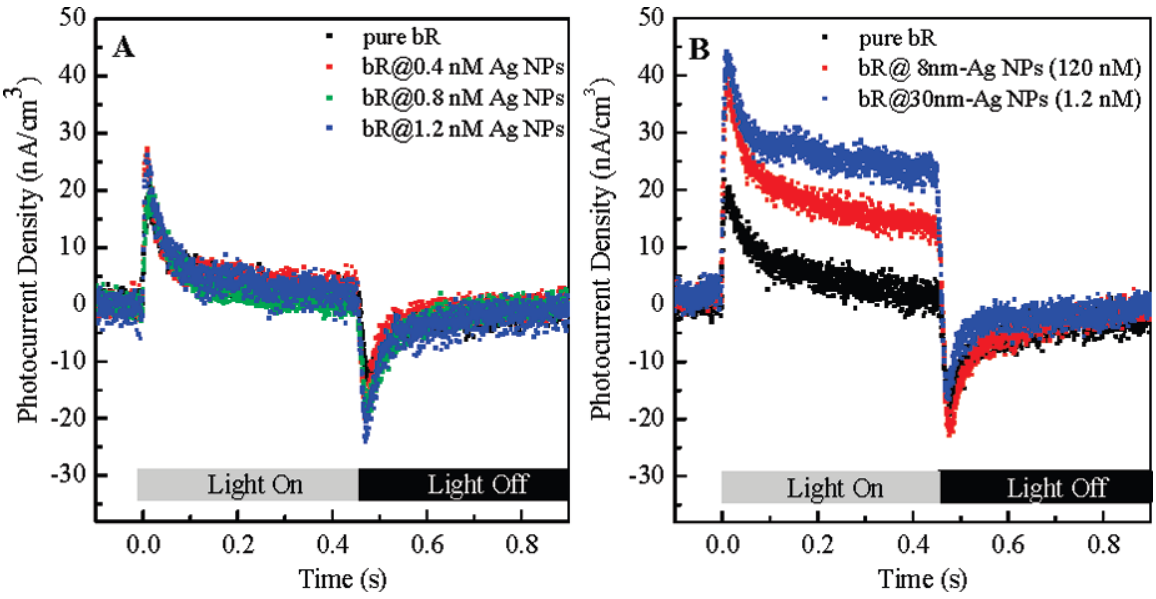

Figure 6-2: (A) The disappearance of the plasmonic photocurrent enhancement of 30 nm Ag NPs if the blue wavelength of the exciting light is filtered out ($\lambda_{incident} > 500$ nm is used). (B) The effect of changing the overlap between the SPR extinction band in the blue region with the M_{412} absorption band (see Fig 6-3). As the overlap decreases (by using 8 nm Ag NPs), the weaker the observed photocurrent becomes.

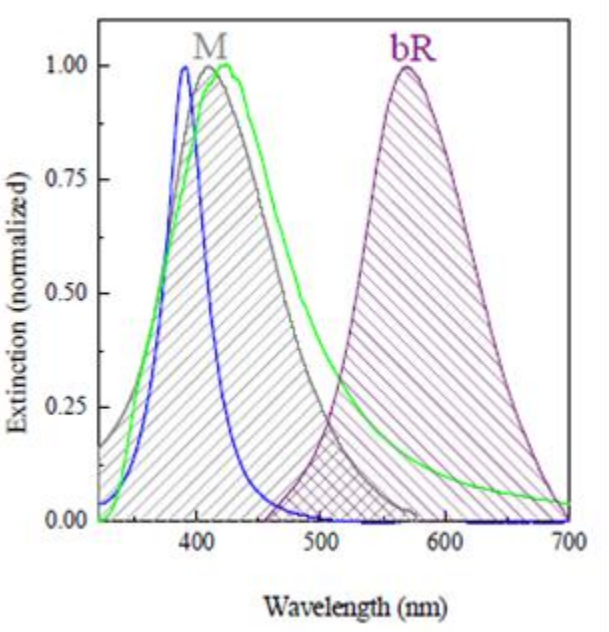

Figure 6-3: Normalized surface plasmon resonance (SPR) spectra of 8 nm (blue lines) and 30 nm Ag nanoparticles (green lines). The SPR band of 8 nm-Ag NPs is at 395 nm and the 425 nm for 30 nm Ag NPs. The contour of M state and bR state absorption region was represented by gray and violet shadows with corresponding maxima at 412 nm and 570 nm.

Kinetic and Spectroscopic Study on the Plasmonic Field Enhancement of the Solar-to-Electric Conversion by Bacteriorhodopsin

The absorption contour and extinction band of the surface plasmon resonance regions of the AgNPs are adjustable by controlling their size distributions. Figure 6-4 shows the normalized absorption contours of the bR (purple) and the M intermediate (blue). The 40-nm AgNPs (brown) whose corresponding extinction maximum at 430 nm exhibits greater spectral overlap with the M intermediate absorption band than the 8-nm particles (orange), whose maximum peak is at 397 nm.

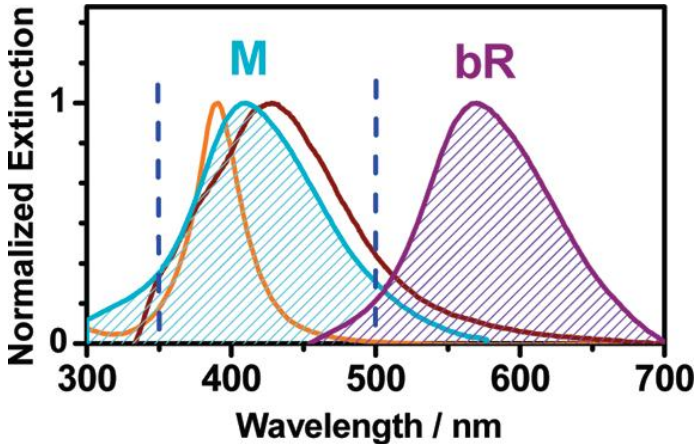

Figure 6-4: Normalized surface plasmon resonance spectra of 8 nm (orange) and 40 nm (brown) Ag NPs. The absorption contours of M and bR species are represented by blue and purple shadows with corresponding maxima at 412 nm and 570 nm, respectively. The bR photocycle is photo-initiated by the short-pulsed 532-nm laser and the continuous blue light exposure is between 350-550 nm (shown in blue dot lines). The monitor window of the recovery of bR and the decay of M intermediate are followed at 600 nm and 450 respectively to avoid the spectral overlap with AgNPs and laser scattering.

The above spectra are obtained by decomposing the observed spectrum into a contribution from pure bR absorption and AgNPs extinction. The extinction of AgNPs is at wavelengths shorter than 600 nm, which eliminates the spectral overlap with the bR absorption and the interference with the monitored temporal profile. Previous results shown

that the M intermediate absorbs one blue photon to return to the bR ground state without passing through the slow conventional photocycle.[18,41] If this is the reason for our previously reported plasmonic enhancement of the bR photocurrent, then the cooperation of plasmonic field effect and the blue light effect on the kinetics of bR photocycle should be observed. Furthermore, the degree of perturbation of the different sizes of AgNPs on the kinetics of bR photocycle should be strongly correlated with the overlap between the extinction of the AgNPs and the M absorption band.

The 532-nm pulsed laser and the cw blue light were collimated in opposite directions and overlapped at the center of the sample cell, as shown in Scheme 6-1. After the short pulsed irradiation from the 532-nm laser for 50 μs, the dominant components of the modulation at 600 nm absorption ($\Delta A_{600}(t)$) are the L decay and the bR recovery.[8] Although the N intermediate exhibits absorption at 600nm, the transient concentration of the N intermediate has been proven to be low in the photocycle when the pH is controlled at ~7.[42] In addition to the observation of the recovery of bR, the light modulation at 450 nm ($\Delta A_{450}(t)$) reflects the kinetics of the M intermediate.

The recovery of bR upon 532-nm pulsed laser excitation was monitored at 600 nm in the presence and the absence of exposure to the external blue light. Studies were carried out with addition of two sizes of AgNPs (8 and 40 nm). The dependence of the kinetics on the plasmonic field of these two sizes was compared.

Figure 6-5 represents the temporal profiles of the bR recovery in the presence and absence of blue light by adding AgNPs of 8-nm (A) and 40-nm (B), respectively. Upon excitation of the pure bR suspension, the simultaneous cw blue light exposure resulted in the acceleration of the recovery of the bR state. The addition of AgNPs (either 40 nm or 8 nm AgNPs) accelerates the bR recovery rate even without introducing the blue light to the systems. However, when both conditions were achieved (the addition of AgNPs and cw blue light), the bR recovery rate was accelerated significantly.

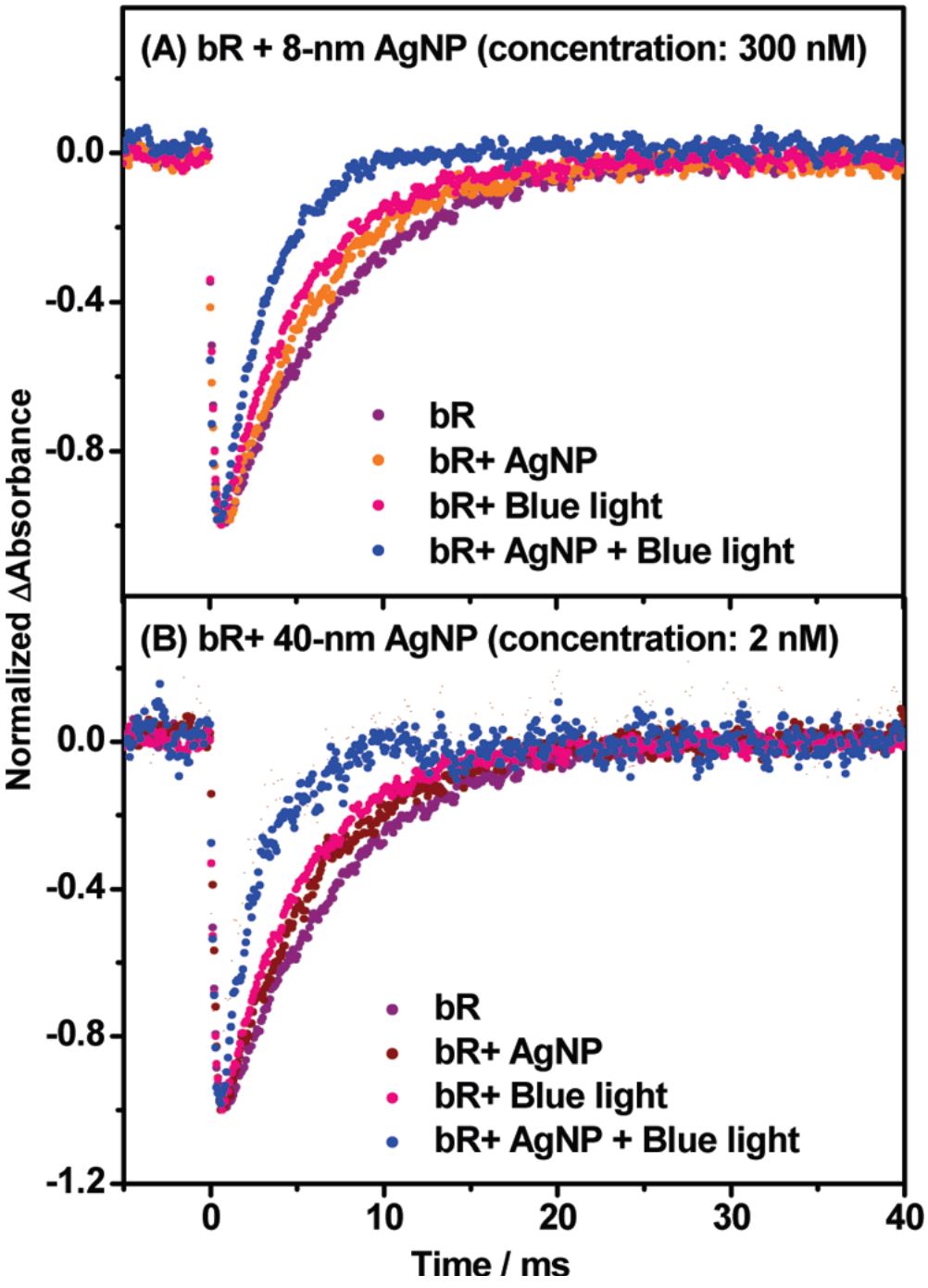

Figure 6-5: The plasmonic field enhancement of the blue light effect on the bR recovery during its photocycle. Normalized temporal profiles of the modulation at 600 nm upon 532-nm pulsed excitation of the mixtures of bR with (A) 8-nm AgNP and (B) 40-nm AgNP in the presence of cw blue photon (350-500 nm). The addition of AgNPs and exposure to the blue light accelerate the bR recovery. The concentration of buffer solution, bR, 8-nm AgNP and 40-nm AgNP are 1.1 mM, 8.8 μM, 300 nM and 2.0 nM, respectively. The power of the cw blue irradiation (in 350-500 nm) is 0.12 W cm^{-2} and the fluence of the 532-nm pulsed laser is 5.5 mJ cm^{-2}.

The blue light effect is shown to accelerate the recovery rate of bR. However, it is difficult to monitor the kinetics of the M intermediate at its absorption maximum by time-resolved spectroscopy because of the large overlap between the spectral regions of the 40 nm AgNPs and the M state. As a result, only 8 nm-AgNPs can be used with bR for observing the kinetics of the M intermediate. The monitoring window is set at 450 nm to avoid interference from the extinction of the 8 nm-AgNPs. The main component of the temporal profile at 450 nm is attributed to the M intermediate absorption (See Figure 1). On the basis of our proposed mechanism, the decay of the M intermediate can be described by single exponential curve. In Figure 6-6, the colored circles and their corresponding solid lines represent the observed and fitted data, respectively. The fitted data agree well with the observed temporal profiles. Similar to the results of the bR recovery rate, the decay of the M intermediate was accelerated by the addition of Ag NPs or by exposure to the blue light. A more pronounced acceleration of the M decay was observed by exposure to the blue light in the presence of AgNPs. The accelerated decay of the M intermediate was consistent with the recovery of bR when monitored at 600 nm.

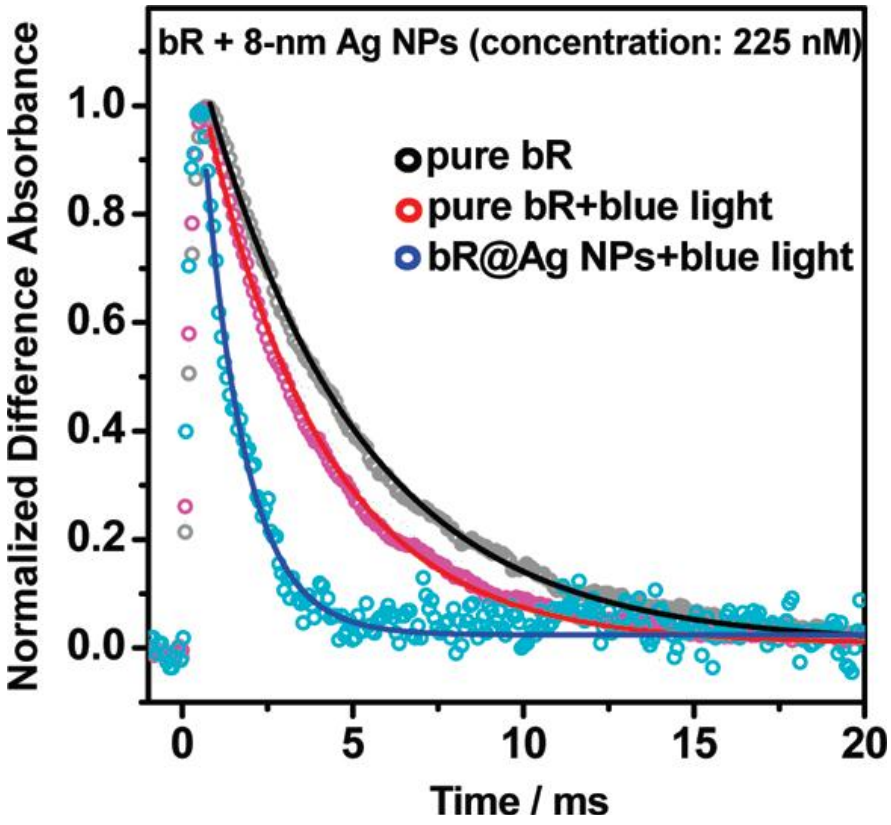

Figure 6-6: Plasmonic field enhancement of the blue light effect on the decay of M intermediate during its photocycle. The effect on the decay of the M intermediate (black), in presence of blue light (red), and by plasomincally enhanced blue light effect (blue). Normalized temporal profiles of the modulation at 450 nm upon 532-nm pulsed excitation of the mixtures of bR with 8nm Ag NPs in the presence of continuous irradiation of blue photon (350-500 nm). The concentration of 8-nm AgNPs is 225 nM. The power of the cw blue light is 0.12 W cm^{-2} and the fluence of the 532-nm pulsed laser is 5.5 mJ cm^{-2}, respectively.

In order to illustrate the temporal behavior of the bR recovery, the following simplified mechanism is used:

$$bR \xrightarrow{h\nu(\phi)} L \xrightarrow{k_1} M \xrightarrow{k_2} bR \quad k_2: \text{the rate constant of conventional cycle (No Blue light)} \qquad (3)$$
$$\xrightarrow{k_3} bR \quad k_3: \text{the rate constant of bypassed cycle (with Blue light)}$$

A detailed mathematical expression of the time dependence of the bR concentration ($\Delta A_{600}(t)$) and the time dependence of the M intermediate concentration ($\Delta A_{450}(t)$) is developed in the Appendix. k_{II} is the apparent rate constant of the conversion of M to bR.

In the absence of cw blue light exposure, only the conventional photocycle should be considered and k_{II} is merely composed of k_2 for the conventional photocycle ($k_{II} = k_2$). Upon the irradiation with the cw blue light, the bypassed photocycle is activated. Thus, k_{II} is composed of both k_2 and k_3, which denotes the apparent rate constant of the conversion of M to bR through the bypassed process ($k_{II} = k_2+k_3$). k_1 and k_{II} are derived by fitting the observed temporal profiles with two exponential components. The difference of k_{II} in presence and absence of blue light is due to k_3, which represents the rate constant of the bypassed cycle and measures blue light effect.

The comparisons of the observed and fitted data are shown in Figure 6-7. The minor residual intensities, derived from the difference of the observed and fitted temporal profiles, are also shown in each figure. Due to the strong light scattering from the 40 nm-Ag NPs, the signal to noise ratio is relatively smaller than that of the others (Figure 6-7). However, the observed agreement and the small residual intensity show that the proposed mechanism agrees well with the observed data.

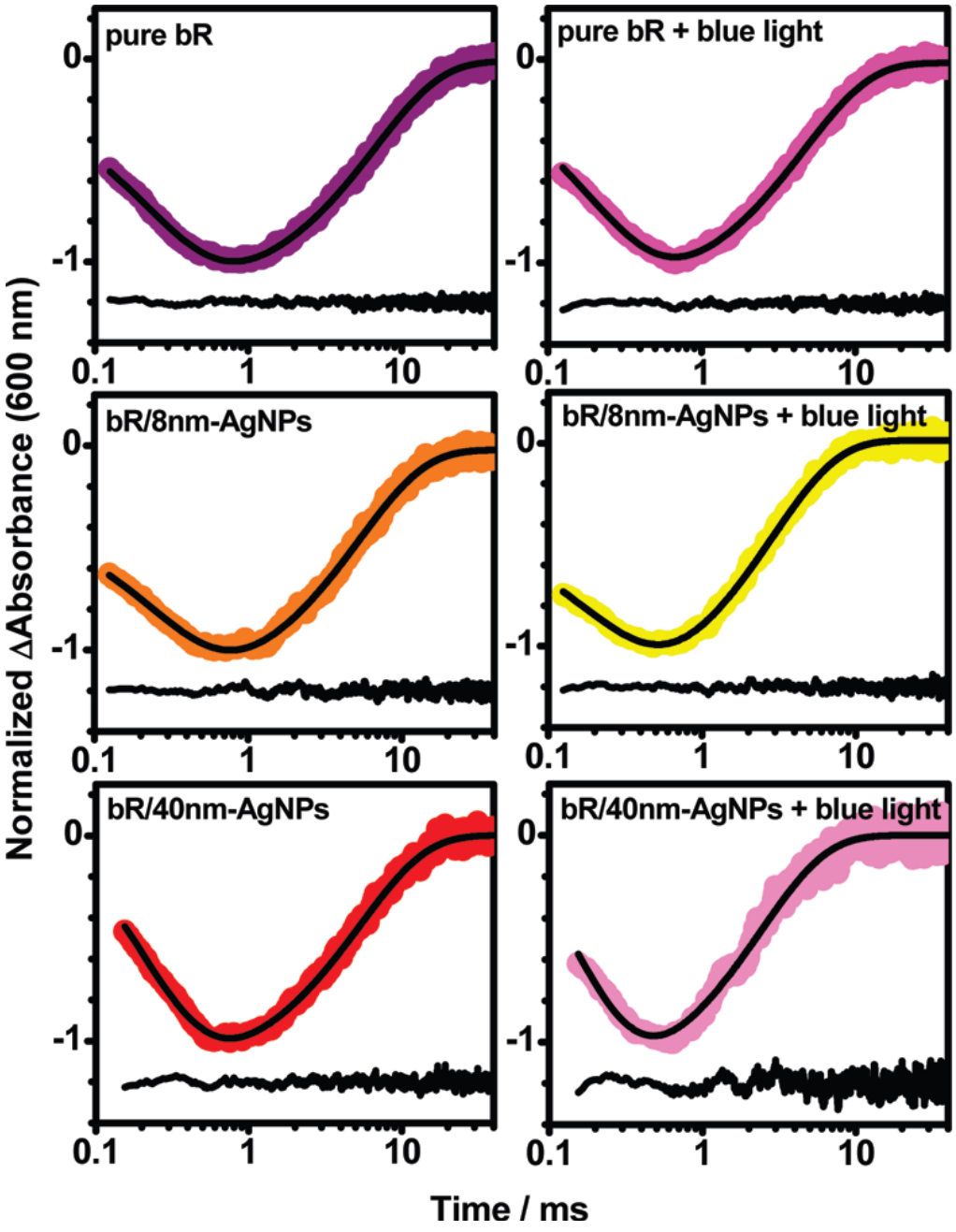

Figure 6-7: The comparisons of the experimental (color traces) and the fitted data (black lines) of the 600-nm modulation (bR recovery) for pure bR or bR/Ag NPs mixture upon 532-nm pulsed excitation in the absence or in the presence of blue photon. The differences of the observed and the fitted data (residual intensities) are also shown in black at the bottom traces in every figure.

Both sizes of Ag NPs show the ability to change the kinetics of the bR photocycle. However, the concentration of 8 nm-AgNPs was 100 times higher than that of the 40 nm particles (Figure 6-5). The rate constant of bR recovery in various concentrations of AgNPs are summarized in Figure 6-8a. Without exposure to blue light, the addition of AgNPs is also able to accelerate the rate of bR recovery slightly. With exposure to the cw blue light, the enhancement is much more significant. Moreover, this effect is more noticeable for AgNPs with large size (40 nm) than that for the small particles (8 nm). According to our proposed mechanism, the difference stands for the rate constant of the bypassed photocycle, denoted by k_3, involving the photoexcitation of the M intermediate followed by the rapid reprotonation and isomerization of retinal converting to its initial bR state (Figure 6-8b).

Although the concentration of the 40 nm Ag NPs is 100 times lower than that of the 8 nm Ag NPs, the larger Ag NPs still show more pronounced enhancement of the blue light effect. The broader absorption band of 40 nm Ag NPs can absorb more of blue light thus enhancing the flux of blue photons more than 8 nm particles under the same intensity of illumination.

In order to get a quantitative experimental measurement of the relative plasmonic enhancement of the blue light effect of the 40 and the 8 nm AgNPs, the ratio of the k_3 value per particle needs to be determined. This can be determined from the ratios of the slopes of the lines in fig 6-8b. This ratio is found to be around 400. The value of enhancement factor of each particle depends on a number of factors: 1) the plasmonic field strength as it determines the enhancement of the M absorption. Su et al have shown that the field strength is proportional to the size of nanoparticle. Using the radii of the 40 nm and the 8 nm of AgNPs, the ratio of their sizes is 125.[43,44] 2) The second factor is the transfer rate of the energy between the plasmonic field and the M intermediate which is proportional to the spectral overlap between the electromagnetic extinction band and the M absorption band. This ratio from the 40 nm and 8 nm AgNPs are determined to be 3

from Figure 6-4. These two factors alone suggest that the ratio of plasmon enhancement factor of the two nanoparticles used is around 375, which is close to that observed experimentally.

This agreement might suggest that the exact location of each nanoparticle is not critical. This is due to large size of the nanoparticles, even the small one compared to the size of the active site of retinal in the protein. Thus the retinals in the strongest regions of the field of each nanoparticle are the ones that show the observed enhancements.

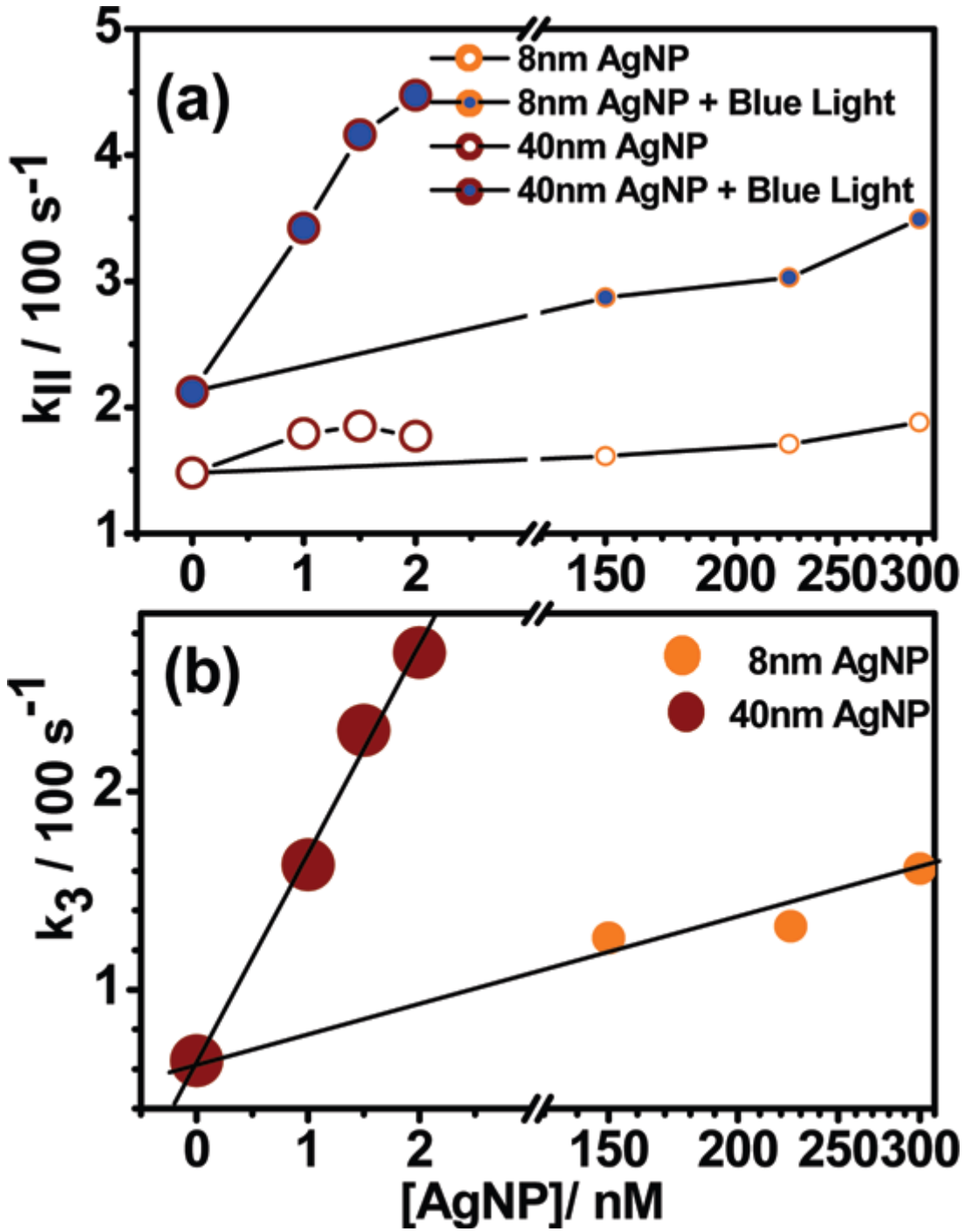

Figure 6-8: (a) The rate constant k_{II} in the presence and absence of blue light up upon excitation of bR with different concentrations of 8-nm and 40-nm AgNP. (b) The difference of the values of k_{II} in the presence and absence of blue light. The difference can be attributed to k_3, which represents the rate constant of the bypassed cycle, i.e., it represents the sensitivity of the plasmonic field enhancement of the blue light effect to the concentration and size of the nanoparticles used.

6.4 Conclusion

Bacteriorhodopsin's exceptional stability makes it a potential biomaterial for various applications.[37] The reported bR-based electrochemical cell used thin films and required external bias combination and laser irradiation source.[38] In our system, cw light is used for the irradiation source and no external bias is needed. Moreover, NPs whose SPR band overlaps well with the M_{412} absorption also overlaps with the maximum intensity region of the solar light at 450 nm (Figure 6-9).[39] Those factors make a bR-based electrochemical cell using plasmonically enhanced photocurrent attractive for solar energy conversion.[40]

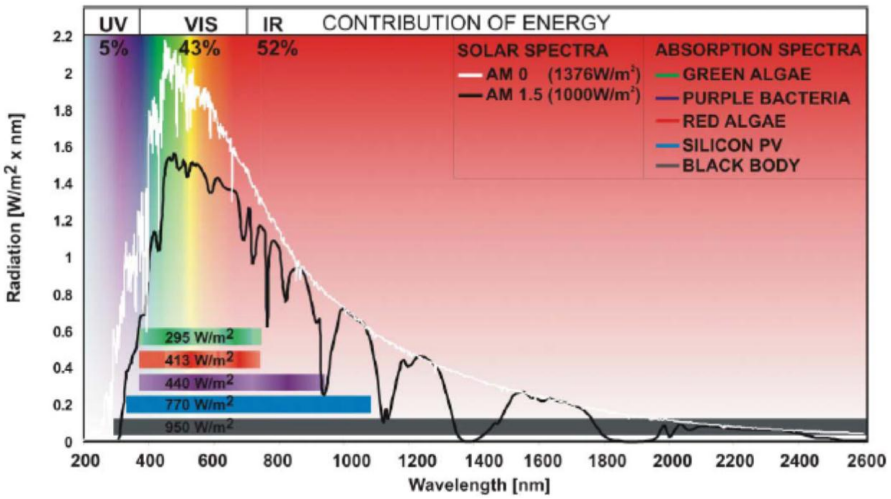

Figure 6-9: Solar irradiance spectrum above atmosphere and at surface

Using time-resolved spectroscopic techniques we were able to study the plasmonic field enhancement of the observed blue light effect on the bR photocycle. The observed blue light enhancement of the bR recovery and of the M intermediates decay give strong support for the previously proposed mechanism of the blue light photocurrent enhancement.[19] The bypassed photocycle can be activated by exposure to blue light and is greatly enhanced in the presence of AgNPs whose surface plasmon field is in the blue spectral region (and can thus greatly enhance the flux of blue light). It is found that the

40-nm AgNPs is about 400 times more efficient than the 8 nm because of the much larger field strength and better overlap between their extinction band and that of the M intermediate absorption band.

6.5 Appendix

Expression of $[L]_t$:

Based on the report by R. R. Birge *et al.* (Ref. 8), the decay rate constant of the L intermediate is slower than that of the generation. Due to the temporal integration window of 10 μs, which is slower than the L generation, the temporal behavior of L can be simplified in a decay component and described as follows,

$$\frac{d[L]}{dt} = -k_1[L].$$

An assumption can be made that the initial concentration of L (denoted as $[L]_0$) is proportional to the quantum yield of bR upon 532-nm pulsed excitation.

$[L]_O = [\boldsymbol{bR}]_{\boldsymbol{O}} \times \phi, \phi$ ***represents the quantum yield of bR bleach***

By means of Laplace transform (***L***),

$$\frac{d[L]}{dt} = -k_1[L], \therefore \boldsymbol{L}[L]' = s\boldsymbol{L}[L] - [L]_O = -k_1\boldsymbol{L}[L]$$

$$\therefore (s + k_1)\boldsymbol{L}[L] = [L]_O = [\boldsymbol{bR}]_{\boldsymbol{O}} \times \phi$$

$$\therefore \boldsymbol{L}[L] = \frac{[\boldsymbol{bR}]_{\boldsymbol{O}} \times \phi}{(s+k_1)}$$

As a result, the temporal profile of L can be expressed as

$$[L]_t = [\boldsymbol{bR}]_{\boldsymbol{O}} \times \phi \times \boldsymbol{e}^{-k_1 t}$$

Expression of $[M]_t$:

Expression of $[bR]_t$ recovery:

$$\frac{d[bR]}{dt} = (k_2 + k_3)[M] = k_{II}[M]$$

$$\therefore \boldsymbol{L}[bR]' = s\boldsymbol{L}[bR] - 0 = k_{II}\boldsymbol{L}[M] = \frac{k_1 \times k_{II} \times [\boldsymbol{bR}]_{\boldsymbol{O}} \times \phi}{(s+k_1)(s+k_{II})}$$

$$\therefore \boldsymbol{L}[bR] = \frac{k_1 \times k_{II} \times [\boldsymbol{bR}]_{\boldsymbol{O}} \times \phi}{s(s+k_1)(s+k_{II})} = \frac{k_1 \times k_{II} \times [\boldsymbol{bR}]_{\boldsymbol{O}} \times \phi}{(k_{II}-k_1)}\left(\frac{1}{s(s+k_1)} - \frac{1}{s(s+k_{II})}\right)$$

$$\therefore [bR]_t = \frac{k_1 \times k_{II} \times [\boldsymbol{bR}]_{\boldsymbol{O}} \times \phi}{(k_{II}-k_1)}\left(\frac{1}{k_1}\left(1-\boldsymbol{e}^{-k_1 t}\right) - \frac{1}{k_{II}}\left(1-\boldsymbol{e}^{-k_{II} t}\right)\right)$$

Expression of $\Delta A_{600}(t)$:

The overall absorbance modulation at 600 nm (ΔA_{600}) should include L decay and bR recovery. Due to the different absorption constants, two weighting parameters (***a*** and ***b*** for bR and L, respectively) should be introduced,

$$\Delta \boldsymbol{A}_{600} = -[\boldsymbol{bR}]_{\boldsymbol{o}} \times \phi \times (\boldsymbol{a} \times \boldsymbol{e}^{-\boldsymbol{k}_1 \boldsymbol{t}} - \boldsymbol{b} \times \boldsymbol{e}^{-\boldsymbol{k}_{\boldsymbol{II}} \boldsymbol{t}})$$

An equation is employed in fitting,

$\therefore \Delta \boldsymbol{A}_{600} = \boldsymbol{y} = \boldsymbol{y}_{\boldsymbol{o}} + \boldsymbol{c} \times \boldsymbol{e}^{-\boldsymbol{dt}} - \boldsymbol{g} \times \boldsymbol{e}^{-\boldsymbol{ht}}$, ***d*** and ***h*** represent $\boldsymbol{k}_1$ and $\boldsymbol{k}_{\boldsymbol{II}}$, respectively.

Expression of $\Delta A_{450}(t)$:

The absorbance modulation at 450 nm (ΔA_{450}) is merely composed of the M intermediate and can be expressed as

$$\therefore \Delta A_{450} = a \times (e^{-k_{II} t} - e^{-k_1 t})$$

When $k_1 >> k_{II}$ at later period, ΔA_{450} can be expressed in a single exponential decay as

$$\Delta \boldsymbol{A}_{450} \approx [\boldsymbol{bR}]_{\boldsymbol{o}} \times \phi \times \boldsymbol{e}^{-\mathrm{k_{II}t}}$$

6.6 References

[1] Oesterhelt, D.; Stoeckenius, W. *Nature New Biol.* **1971**, *233*, 149.

[2] Pebay-Peyroula, E.; Rummel, G.; Rosenbusch, J. P.; Landau, E. M. *Science* **1997**, *277*, 1676.

[3] Essen, L.-O.; Siegert, R.; Lehmann, W. D.; Oesterhelt, D. *Proc. Natl. Acad. Sci. U. S. A.* **1998**, *95*, 11673.

[4] Luecke, H.; Richter. H.-T.; Lanyi, J. K. *Science* **1998**, *280*, 1934.

[5] Luecke, H.; Schobert, B.; Richter, H.-T.; Cartailler. J.-P.; Lanyi, J. K. *J. Mol. Biol.* **1999**, *291*, 899.

[6] Edman, K.; Nollert, P.; Royant, A.; Belrhali, H.; Pebay-Peyroula, E.; Hajdu, J.; Neutze, R.; Landau E. M. *Nature* **1999**, *401*, 822.

[7] Rehorek, M.; Heyn, M. P. *Biochemistry* **1979**, *18*, 4977.

[8] Birge, R. R.; Gillespie, N. B.; Izaguirre, E. W.; Kusnetzow, A.; Lawrence, A. F.; Singh, D.; Song, Q. W.; Schmidt, E.; Stuart, J. A.; Seetharaman, S.; Wise, K. J. *J. Phys. Chem. B* **1999**, *103*, 10746.

[9] Lanyi, J. K.; Váró, G. *Isr. J. Chem.* **1995**, *35*, 365.

[10] Váró, G.; Lanyi J. K. *Biochemistry* **1991**, *30*, 5008.

[11] Váró, G.; Lanyi, J. K. *Biochemistry* **1991**, *30*, 5016.

[12] Váró, G..; Lanyi, J. K. *Biochemistry* **1991**, *30*, 7165.

[13] Subramaniam, S.; Lindahl, M.; Bullough, P.; Faruqi, A. R.; Tittor, J.; Oesterhelt, D.; Brown, L.; Lanyi, J. K.; Henderson, R. *J. Mol. Biol.* **1999**, *287*, 145.

[14] Spassov, V. Z.; Luecke, H.; Gerwert, K.; Bashford, D. *J. Mol. Biol.* **2001**, *312*, 203.

[15] Zimányi, L.; Váró, G.; Chang, M.; Ni, B.; Needleman, R.; Lanyi, J. K. *Biochemistry* **1992**, *31*, 8535.

[16] Gergely, C.; Zimányi, L.; Váró, G. *J. Phys. Chem. B* **1997**, *101*, 9390.

[17] Braiman, M. S.; Bousché O.; Rothschild, K. J. *Proc. Natl. Acad. Sci. U. S. A.* **1991**, *88*, 2388.

[18] Hessling, B.; Herbst, J.; Rammelsberg, R.; Gerwert K. *Biophys. J.* **1997**, *73*, 2081.

[19] Yen, C. W.; Chu, L.-K.; El-Sayed M. A. *J. Am. Chem. Soc*. **2010**, *132*, 7250.

[20] Neretina, S.; Qian, W.; Dreaden, E. C.; Hughes, R. A.; Preston, J. S.; Mascher, P.; El-sayed, M. A. *Nano Lett*. **2008**, *8*, 2410.

[21] Huang, X.; El-Sayed, I. H.; Qian W.; El-Sayed, M. A. *J. Am. Chem. Soc*. **2006**, *128*, 2115.

[22] Yen, C. W.; El-Sayed, M. A. *J. Phys. Chem. C* **2009**, *113*, 19585.

[23] Biesso, A.; Qian, W.; El-Sayed M. A. *J. Am. Chem. Soc.* **2008**, *130*, 3258.

[24] Biesso, A.; Qian, W.; Huang. X. H.; El-Sayed, M. A. *J. Am. Chem. Soc*. **2009**, *31*, 2442.

[25] Oesterhelt, D.; Stoeckenius W. *Methods Enzymol*. **1974**, *31*, 667.

[26] Oesterhelt, D.; Stoeckenius, W. *Nature New Biol*. **1971**, *233*, 149.

[27] Mitchell, P. *Nature* **1961**, *191*, 144.

[28] Belliveau, J. W.; Lanyi, J. K. Arch. *Biochem. Biophys*. **1997**, *178*, 308.

[29] Jin, Y.; Honig, T.; Ron, I.; Friedman, N.; Sheves, M.; Cahen, D. *Chem. Soc. Rev.* **2008**, *37*, 2422.

[30] Ghosh, S. K.; Pal, T. *Chem. Rev*. **2007**, *107*, 4797.

[31] Gersten, J. I.; Nitzan, A. *J. Chem. Phys.* **1980**, *73*, 3023.

[32] Drachev, L. A.; Kaulen, A. D.; Skulachev, V. P. *FEBS Lett*. **1984**, *2168*, 331.

[33] Robertson, B.; Lukashev, E. *Biophys. J.* **1995**, *68*, 1507.

[34] Ormos, P.; Dancshazy, Z.; Karvaly, B. *Biochim. Biophys. Acta* **1978**, *503*, 304.

[35] Li, R.; Li, C. M.; Bao, H.; Bao, Q.; Lee, V. S. *Appl. Phys. Lett.* **2007**, *91*, 223901.

[36] Uehara, K.; Kawai, K.; Kouyama, T. *Thin Solid Films* **1993**, *232*, 271.

[37] Shen, Y.; Safinya, C. R.; Liang, K. S.; Ruppert, A. F.; Rothschild, K. J. *Nature* **1993**, *366*, 48.

[38] Manoj, A. G.; Narayan, K. S. *Appl. Phys. Lett*. **2003**, *83*, 3614.

[39] Kruse, O.; Rupprecht, J.; Mussgnug, J. H.; Dismukes, G. C.; Hankamer, B. *Photochem. Photobiol. Sci*. **2005**, *4*, 957.

[40] El-Sayed, M. A. *Acc. Chem. Res*. **1992**, *25*, 279.

[41] Ludmann, K.; Ganea, C.; Váro, G. J. *Photochem. Photobiol. B: Biol*. **1999**, *49*, 23.

[42] Ludmann, K.; Gergely, C.; Váro G. *Biophys. J*. **1998**, *75*, 3110.

[43] Jain, P. K.; El-Sayed, M. A. *Chem. Phys. Lett*. **2010**, *487*, 153.

[44] Su, K. H; Wei, Q. H.; Zhang, X.; Mock, J. J.; Smith, D. R.; Schultz, S. *Nano Lett*. **2003**, *3*, 1087.

CHAPTER 7

BACTERIORHODOPSIN/TiO_2 NANOTUBE ARRAYS HYBRID SYSTEM FOR ENHANCED PHOTOELECTROCHEMICAL WATER OXIDATION

Abstract

In recent years, considerable efforts have been made to improve the performance of photoactive nanostructured materials for water splitting applications. Herein, we report on the assembly and use of bacteriorhodopsin (bR)/TiO_2 nanotube arrays hybrid electrode system. Photoanode materials composed of ~ 7μm long self-ordered and vertically oriented nanotube array of titanium dioxide films were fabricated via the anodization of Ti foil in electrolytes containing NH_4F at room temperature followed by sensitization of the electrodes with bR. The stability of bR on the TiO_2 surface was found to depend on the pretreatment process of the TiO_2 films. Our results demonstrate the opportunity to fabricate fairly stable bR/TiO_2 hybrid electrodes that can be used as photoanodes for photoelectrochemical water splitting. Under AM 1.5 illumination (100 mW/cm^2), the hybrid electrodes achieved a photocurrent density of 0.65 mA/cm^2 which is a ~ 50% increase as compared to that measured for pure TiO_2 nanotubes (0.43 mA/cm^2) fabricated and tested under the same conditions. This enhancement in photocurrent can be related to the unique proton pumping ability of bR as well as to the novel structural properties of the fabricated nanotube arrays. In the presence of a redox electrolyte, bR can inject electrons into the conduction band of TiO_2 and hence further enhance the resulting photocurrent density. To the best of our knowledge, this is the first report on the use of bR/TiO_2 hybrid electrodes in photoelectrochemical water oxidation cells. We believe the

proton pumping property of bR can be used in a variety of applications, especially those related to third generation photovoltaic cells.

7.1 Introduction

Researchers have been actively trying to transfer solar energy into a fuel for the last 40 years without a profound success despite the fact that nature was already been doing so for millions of years through photosynthesis. There are two distinct photosynthetic systems in nature: chlorophyll (using electron pump system) and bacteriorhodopsin (using proton pump system).[1] Bacteriorhodopsin (bR), a natural light activated protein, is found in the purple membrane of *Halobacterium salinarum*.[2-4] The exceptional stability of bR makes it a potential biomaterial for various applications. bR can absorb sun light and transform it into electricity which makes it promising for a plethora of applications especially those related to solar energy conversion.[5,6] However, the photocurrent of bR-based photovoltaic cells is still limited to the pico-ampere range.[7] This is mainly due to the fact that the photocycle of bR takes 15 ms to finish. A short cut of the photocycle is expected to enhance the proton pumping effect of bR. Recently, we developed a new bR solution-based photoelectrochemical cell that takes advantage of the plasmonic field effect of nanoparticles to modify the photocycle of bR[8,9] and thus increase the duty cycle of proton production by decreasing the time to 70 μs.[10-12] Upon the addition of silver nanoparticles (with a resonance peak in the blue light region), the plasmonic field of the silver nanoparticles was found to significantly enhance the generated photocurrent density up to 25 nA/cm^3, which is 15 times higher than that of pure bR.[9] This mechanism was further verified by spectroscopic and kinetic studies.[13] Although the plasmonic field enhancement of bR produces a photocurrent that is orders of magnitude higher than the previous reports, it is still not sufficient for realistic

applications.

Fujishima and Honda reported the generation of hydrogen gas via water splitting using TiO_2 under UV light irradiation.[14] Since then, H_2 generation based on various semiconductors has been extensively studied.[15] Of particular interest are anodically fabricated TiO_2 nanotube arrays, which are being widely investigated due to their advantageous properties such as low cost, abundance, stability and vectorial charge transfer.[16-18] However, the wide bandgap of this material (3.0−3.2 eV) limits its spectral response to the UV region of the light spectrum, which accounts only for less than 5% of the full solar spectrum.[19] More efficient visible light utilization would render this material quite attractive for solar energy conversion applications.

The relatively low efficiencies and high costs of first and second generation photovoltaic cells, compared to traditional energy sources, has limited their mainstream use. The third-generation of such cells aims at decreasing the cost while achieving higher efficiency.[19] The concept behind this new generation is to use materials which are both nontoxic and highly abundant. The abundant and environmentally friendly bio-conjugated semiconductor hybrid systems seem to be promising as a third generation photoelectrochemical/photovoltaic technology.[20] To this end, Grätzel developed chlorophyll-based dye-sensitized solar cells.[21,22] In those devices, photo-excited chlorophyll injects electrons into the conduction band of a TiO_2 photoanode to power an external load which in turn are being re-introduced into the cell through the use of a redox electrolyte. [21,22] However, the majority of the bio-conjugated semiconductor hybrid systems treat biomaterials as dye molecules which can absorb visible light and transfer electrons to semiconductors. In addition to extending the absorption to the visible range (intense absorption peak in the range 500-600 nm) and transferring electrons to the photoanode, bR's unique proton pumping characteristic can successfully be applied to solar-driven hydrogen production.

In this work, we create the first bR/TiO_2 nanotube hybrid photoanode to perform

water-splitting and generate photocurrent. The bR/TiO_2 hybrid photoanode shows a better photoelectrochemical performance than either of TiO_2 or bR alone. A possible mechanism for the observed enhancement of photocurrent has been investigated. The electron transfer property of bR, in the presence of redox electrolyte, is also discussed.

7.2 Experimental Section

Fabrication and Characterization of TiO_2 Nanotube Arrays

Prior to anodization, pure titanium foil samples (2.0 cm x 1.0 cm x 0.25 mm) were ultrasonically cleaned with acetone followed by a deionized (D.I.) water rinse. The anodization was performed in a two-electrode electrochemical cell, with the titanium foil as the working electrode and platinum foil as the counter electrode, at room temperature (approximately 22℃) at 20V for 20h in a formamide-based electrolyte containing 0.2M NH_4F, 0.1M H_3PO_4 and 3 vol.% H_2O. Agilent E3612A DC power supply was used for potentiostatic anodization. After anodization, the samples were rinsed thoroughly with deionized water and isopropyl alcohol, then dried under a stream of nitrogen. The as-anodized samples were crystallized by oxygen annealing at 500 ℃ with a heating and cooling rate of 1℃/min. The morphology of the as-anodized samples was examined using a Zeiss SEM Ultra60 field emission scanning electron microscope (FESEM). X-ray photoelectron spectroscopy (XPS) experiments were performed on the TiO_2 films using a Thermo Scientific K-alpha XPS with an Al anode. Spectra were charge referenced to O 1s at 532 eV. The crystalline phases were detected and identified by a glancing angle x-ray diffractometer (GAXRD) on an X'pert PRO MRD with Copper source.

Sensitization of TiO_2 with bR

Native bR in the purple membrane (PM) from *Halobacterium Salinarium* was

prepared by a standard method described by Oesterhelt and Stoeckenius.[23] Strain S-9, with a higher PM yield and an absence of carotenoids, was chosen for these experiments. The PM suspension was stored at -10 ℃ for further use. The bR solutions were light adapted before the measurements. The photo-bleached bR was prepared following the method presented by Oestergel *et al*.[24,25] Briefly, the purple bR was suspended in 1.0 M hydroxylamine (NH_2OH) and the pH was adjusted to 8.0 by 1.0 M NaOH. It was then taken for light irradiation from a Xe lamp filtered through a Corning glass filter type 3-66 and 3-67. The complete removal of retinal took 4-5 hours to accomplish. The bleached samples were ready to use after being washed with DI water and centrifuged three times at 19,000 g. Two methods were used to attach bR onto TiO_2 surfaces: without a linker and with a linker. Attaching the bR onto the TiO_2 without a linker was accomplished by simply immersing the TiO_2 thin films into a bR solution (pH=7) and leaving them overnight. The excess solution on the TiO_2 surface was then dried by nitrogen gas. In the other method, the linker chosen was 3-Mercaptopropionic acid. Here, the TiO_2 electrode was first soaked in the 3-Mercaptopropionic acid solution overnight. Then it was cleaned under nitrogen gas, transferred into a bR solution and sonicated for 4 hours. The concentration of bR for both methods was 0.1 mM.

Optical and Photoelectrochemical Characterization

The optical characterization of the bR/TiO_2 films was performed using a Shimadzu UV-Vis-NIR spectrophotometer UV-3101PC. The photoelectrochemical properties were investigated in pH=7 solutions using a three-electrode configuration with TiO_2 nanotubes as photoanode, saturated Ag/AgCl as a reference electrode, and platinum foil as the counter electrode (Scheme 7-1). The redox electrolyte (Iodolyte AN-50) was obtained from Solaronix, Inc. (Switzerland). A scanning potentiostat (Solartron, model 1287) was used to measure dark and illuminated currents at a scan rate of 10 mV/s. A 150 W ozone-free xenon arc lamp fitted with an AM 1.5G filter was used as the light source.

The incident power intensity of the radiation from the AM 1.5 light was set to 100 mW/cm^2

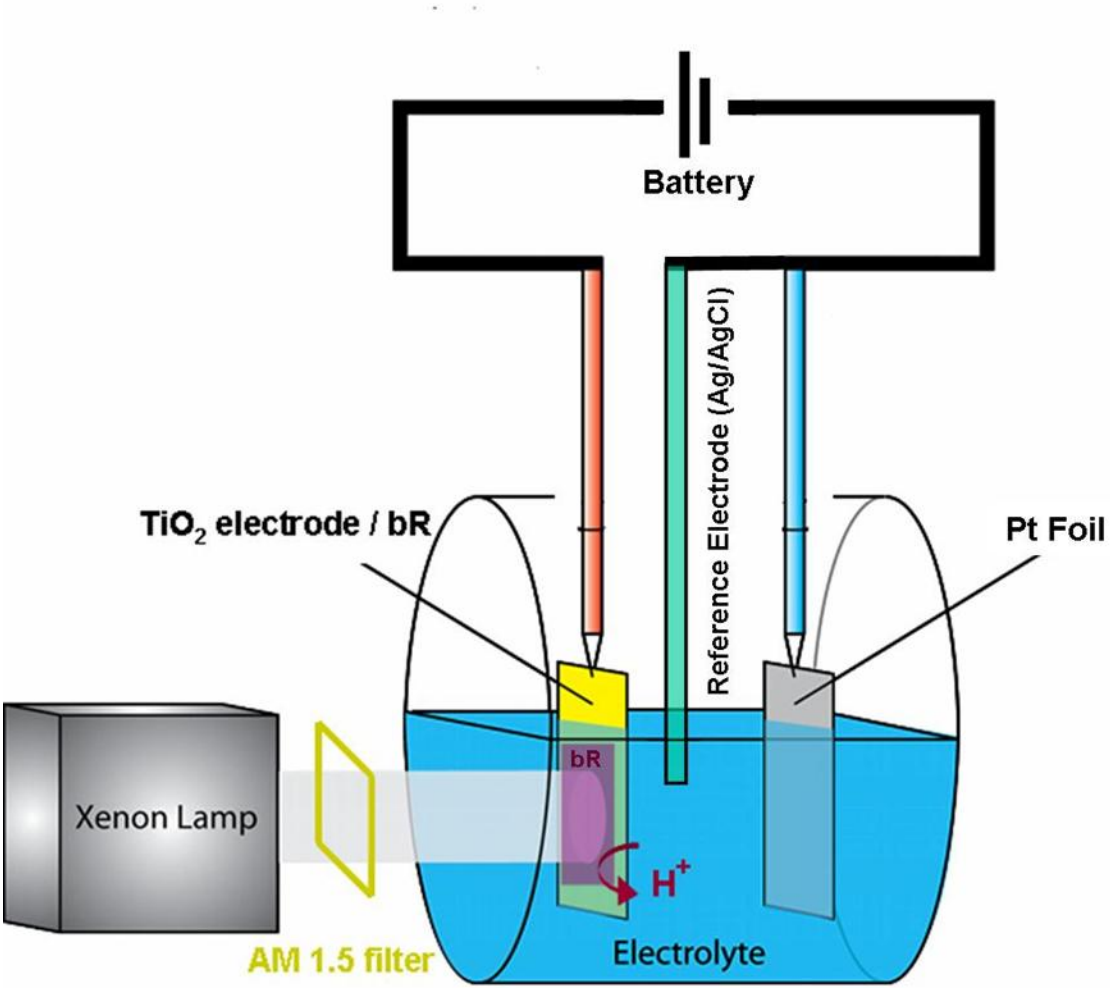

Scheme 7-1: Experimental setup for photoelectrochemical water splitting. The three electrode configuration was used. The TiO_2 or bR/TiO_2 was as photoanode, platinum foil as counter electrode, and Ag/AgCl as reference electrode. The irradiation source was Xe lamp with 1.5 AM filter (intensity: 100 mW/cm^2).

7.3 Results and Discussion

Synthesis and Structural Characterization

Figure 7-1 shows the morphology of the anodically fabricated titania nanotube arrays. The tubular structure with nearly uniform wall thickness throughout the length of the tube is evident. The fabricated nanotubes were found to be approximately 7 ± 0.2 μm in length with outer diameters of 140 ± 2 nm and wall thicknesses of 20 ± 2 nm.

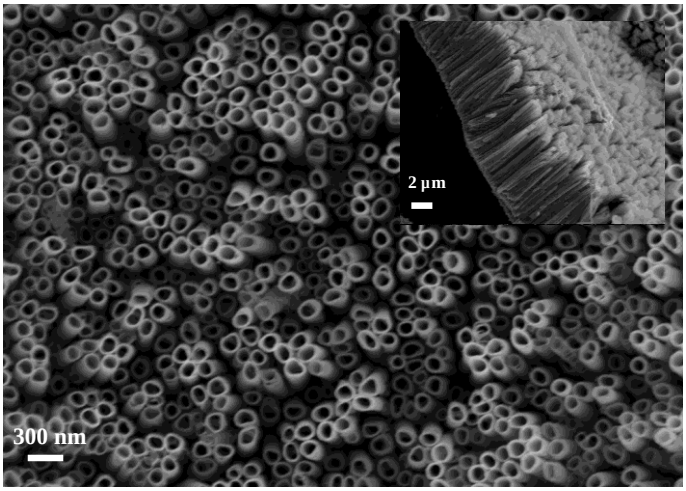

Figure 7-1: FESEM top view image of the fabricated TiO_2 nanotube arrays with the inset showing the cross-sectional view.

After annealing at 500 ℃ for 4 hours in dry oxygen ambient, the pure anatase phase of TiO_2 was formed as confirmed by GAXRD measurements (Figure 7-2a). To further investigate the composition of the annealed nanotube arrays, XPS analysis was performed (Figure 7-2b and 7-2c). Note that the formation of oxide is evident from the O1s and Ti2p peaks with the molar ratio Ti/O being close to the stoichiometric proportion. Note also that both Ti $2p_{3/2}$ and $2p_{1/2}$ peaks are observed with a separation of 5.7 eV, which confirms the presence of Ti^{4+}.[17,18] The above characterizations confirm the synthesized TiO_2 nanotubes to be highly crystalline anatase.

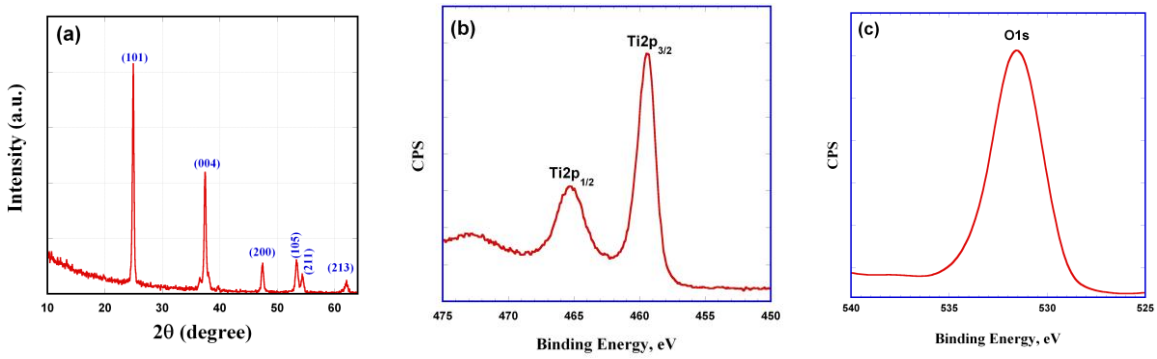

Figure 7-2: (a) Glancing angle x-ray diffraction patterns and (b), (c) XPS spectra of 7 μm long TiO_2 nanotube arrays annealed at 500 ^{0}C for 4 hours in dry oxygen ambient

The main absorption range of native bR in solution phase is between 500-600 nm and the maximum absorption peak lies at 568 nm (Figure 7-3). Anchoring bR molecules onto a TiO_2 surface effectively expands the absorption region of TiO_2 from UV to visible light. Herein, we used two different protocols to attach bR to TiO_2 and followed the treatment effect on the absorption properties of the resulting bR/ TiO_2 assembly. In the first protocol, the TiO_2 electrode was immersed in a solution containing bR. This method is expected to result in the physisorption of bR onto TiO_2 surface where the binding force between bR molecules and TiO_2 surface is weak. The random attachment of bR onto the surface of TiO_2 results in a broad bR absorption peak which loses its characteristic band structure (peak 2, Figure 7-3). In the other protocol, 3-Mercaptopropionic acid was used as a linker to attach the bR molecules onto the surface of TiO_2. In this case, a well-established bR absorption peak was observed (peak 3, Figure 7-3). Note also that the absorption intensity of bR improves upon the use of linker molecules.

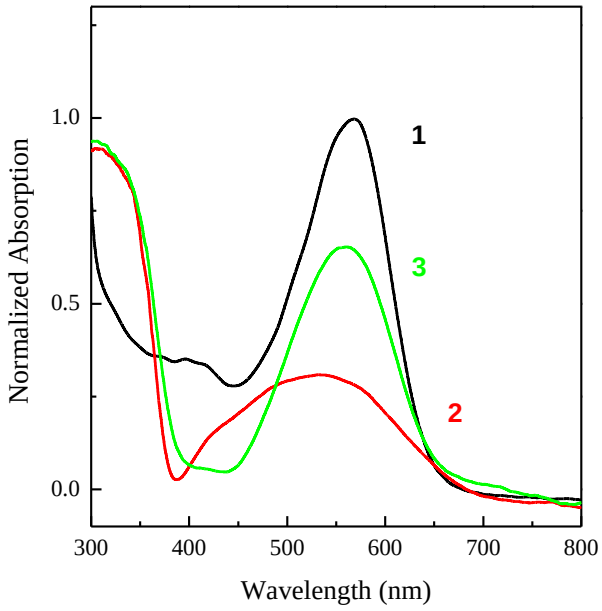

Figure 7-3: UV-Vis spectra of bR in the solution phase (black 1), and bR anchored to TiO_2 without (red 2) and with (green 3) linker.

Proton Pumping Effect of bR

Upon conducting the photoelectrochemical tests, almost 50% of the bR anchored onto the TiO_2 surface without a linker were lost into the electrolyte solution after several electrochemical runs. However, no noticeable change for the bR molecules attached to TiO_2 using linker was observed even after multiple runs. Therefore, the photoelectrochemical measurements were only done for the samples prepared via anchoring bR to TiO_2 using linker.

The photocurrent density-versus-potential measurements are shown in Figure 7-4. The maximum obtained photocurrent of pure TiO_2 (shown in black) was 0.43 mA/cm^2 with an open-circuit voltage (V_{OC}) of -0.49 V. When bR molecules were anchored to the TiO_2 surface (shown in green), the maximum value of photocurrent jumped to 0.65 mA/cm^2 and the V_{OC} was shifted to -0.56 V, i.e. the maximum photocurrent density increased by about 50%. The open-circuit voltage represents the contribution of light

toward the minimum voltage needed for the water-splitting potential (1.229V).[18] Therefore, it seems that the bR/TiO_2 photoanode requires less voltage for water oxidation than pure TiO_2 photoanode does. To explain how bR can enhance the photocurrent density of TiO_2 and shift its open-circuit voltage, it will be necessary to describe the processes of photoelectrochemical water-splitting reactions using TiO_2 photoanode[26]:

$$TiO_2 \xrightarrow{h\upsilon} e^- + h^+$$

$$Anode: \quad H_2O_{(liquid)} + 2h^+ \rightarrow 2H^+ + \tfrac{1}{2}O_{2(gas)}$$

$$Cathode: \quad 2H^+ + 2e^- \rightarrow H_{2(gas)}$$

$$Overall: \quad 2h\upsilon + H_2O_{(liquid)} \rightarrow \tfrac{1}{2}O_{2(gas)} + H_{2(gas)}$$

Absorption of photons by the TiO_2 photoanode results in the formation of electron-hole pairs (e^-/h^+). The photogenerated holes oxidize water and the resulting hydrogen ions migrate to the cathode through the electrolyte. On the other hand, the photogenerated electrons move from photoanode to cathode through the external circuit. Then, reduction of the hydrogen ions by the transferred electrons at the cathode occurs. In a typical TiO_2-based photoelectrochemical cell, the only source of protons is the water oxidation via the photogenerated holes. However, when bR is anchored to the TiO_2 surface, bR can provide another channel for proton production as it is a well-known proton pump.[1] In our designed cell, the proton pumping process of bR continued with light irradiation and the generated protons drifted from the photoanode to the cathode. The increased number of protons at the cathode acts as a driving force to attract more electrons from the external circuit leading to more hydrogen reduction and more photocurrent generation. Additionally, bR can function as a traditional dye in the same way dye molecules act in dye sensitized solar cells, i.e. absorb visible light and help extend the system's absorption capability. The enhanced proton generation and the extended absorption spectrum of bR/TiO_2 cell improve both the water-oxidation performance and photocurrent density.

It may be questioned whether the improvement of the performance of the bR/TiO_2 photoanode is due to a structural change or chemical modification of TiO_2 during the sample preparation process instead of being due to the bR. Therefore, we designed two experiments to prove that the proton pumping characteristic and the extended absorption spectrum of bR are the main reasons for the observed enhancement. The first experiment uses the same bR/TiO_2 sample under the same experimental conditions except a filter is used to cut off the light between 500 to 600 nm for sample irradiation. Note that the unique absorption band of bR lies between 500 and 600 nm (yellow light) and the light in this region is the source for initiating the bR photocycle, i.e. bR could not accomplish the proton pumping process in the absence of such light. The obtained photocurrent under these conditions is shown in red in Figure 7-4a. The maximum photocurrent density of bR/TiO_2 in the absence of yellow light is 0.47 mA/cm^2 and the open-circuit voltage is -0.50 V. The performance of the bR/TiO_2 photoanode in the absence of yellow light is as same as that of the pure TiO_2 photoanode (0.43 mA/cm^2, -0.49V) confirming the fact that proton pumping is a determinant factor in enhancing the photogenerated current.

In the other experiment, bleached bR was used instead of native bR (Figure 7-4b). Retinal is in the center of bR and is the component responsible for triggering the bR photocycle after retinal photo-excitation by yellow light. The retinal of bR can be extracted by photo-bleaching using hydroxylamine which is characterized by the absence of its absorption peak at 568 nm. The bleached bR is anchored, under the same conditions as the unbleached (native) one, to the TiO_2 surface. No obvious absorption peak in the visible range of bleached bR/TiO_2 was observed and the main absorption was shown only in the UV region, characteristic of TiO_2. As bR could not accomplish proton pumping without retinal, the bleached bR on the TiO_2 surface could not increase the concentration of protons even under full light irradiation. The maximum obtained photocurrent density of bleached bR/TiO_2 is 0.47 mA/cm^2 and the V_{OC} is -0.49 V, compared to pure TiO_2 indicating no enhancement in photocurrent density or V_{OC}. These two experiments

confirm that the increased photoelectrical performance of the bR/TiO_2 hybrid system is due to the proton pumping effect of bR and not surface composition or structural change of TiO_2 photoanode.

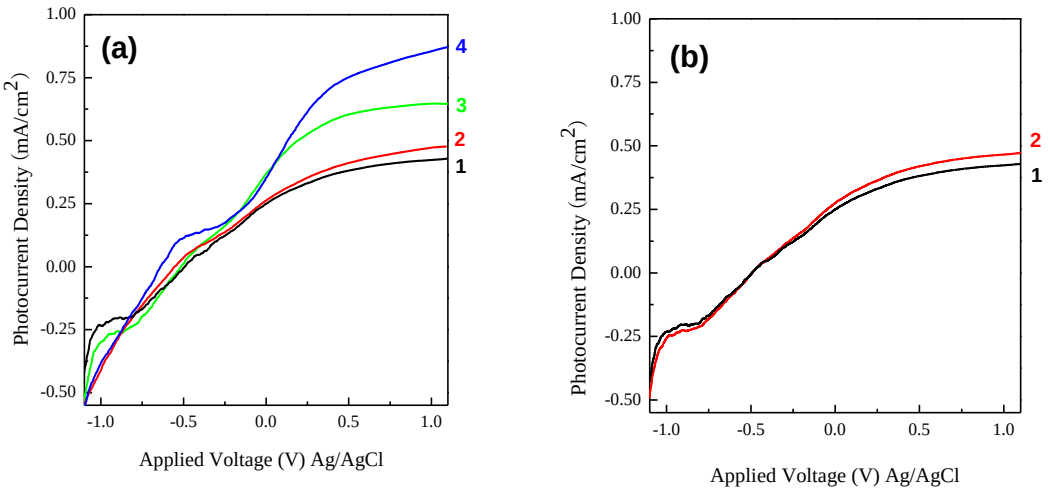

Figure 7-4: Photocurrent density versus potential (I-V) in pH=7 solution under AM 1.5 G illumination (100 mW/cm^2). (a) (1) pure TiO_2, (2) native bR/TiO_2, with the yellow light for bR photoexcitaion is filtered out (cut off $\lambda_{incident}$ 500-600 nm), (3) native bR/TiO_2, and (4) native bR/TiO_2 with redox molecules in the electrolyte. (b) I-V characteristics of (1) pure TiO_2 and (2) bleached bR/TiO_2

As the stability of the hybrid electrode is critical, we also studied the change in the photocurrent response over time. The photocurrent response was almost identical over 50 cycles which demonstrates the rigid structure of bR/TiO_2 photoanode (Figure 7-5). These results show that bR/TiO_2 hybrid electrodes can be used for many applications because of their high stability and performance.

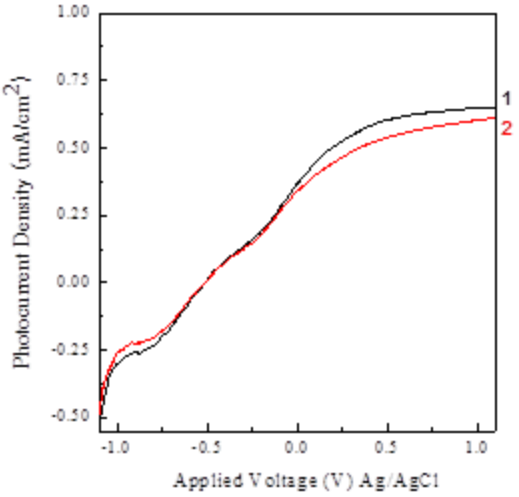

Figure 7-5: Stability tests of bR/TiO_2 photoanode (1) The 1st scan for photoelectrochemical water oxidation, (2) The performance of water oxidation after 50th scan.

Electron Transfer effect

Can bR inject electrons into TiO_2 in the same way dyes do in dye-titania system? Recently, Thavasi *et al* used bR triple mutant E9Q/E194Q/E204Q (3Glu) to construct an excitonic solar cell and found the 3Glu could help transfer electrons from redox electrolyte to anode.[27] Lu *et al* has also found the trans-membrane protein complex from non-sulfur bacteria (Rb. Sphaeroides) to have the same electron transfer effect.[28] Herein, the electron transfer effect of bR has also been investigated in our system by introducing an additional source of electrons to the electrolyte system, i.e. redox electrolyte (iodide/tri-iodide). The lowest unoccupied molecular orbital (LUMO) and highest occupied molecular orbital (HOMO) of bR were previously determined by surface photovoltage spectroscopy (SPS) to be -3.8 eV and -5.2 eV.[29] The energy diagram of bR and TiO_2 is shown in scheme 1. The conduction band (CB) energy of TiO_2 is located at -4.2 eV and therefore the bR is energetically favorable for electron injection into TiO_2, see

Scheme 1. In the presence of the redox electrolyte (I^-/I_3^-), the electrons from the redox molecules can be caught by bR molecules which in turn is expected to inject them into the TiO_2 surface. The I-V characteristic curve upon the addition of redox electrolyte is shown in Figure 4a. The maximum photocurrent density is found to be 0.87 mA/cm^2 and the V_{OC} is -0.64 V. Compared to the value of bR/TiO_2 in the absence of redox electrolyte (maximum photocurrent of 0.65 mA/cm^2 and V_{OC} of -0.56V), a 33% increase in the photocurrent was obtained which can be mainly attributed to the electron transfer effect of bR.

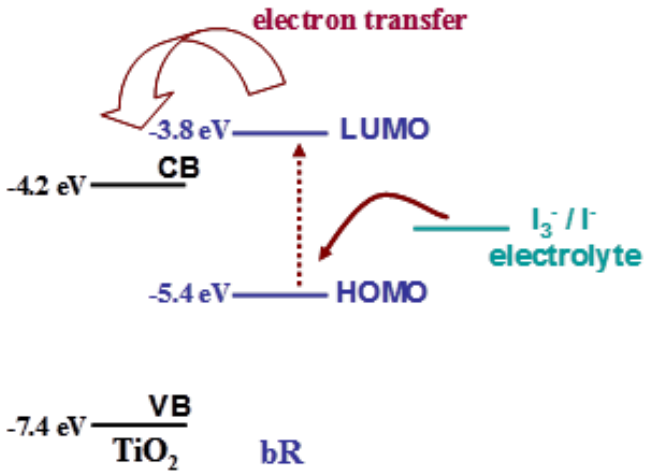

Scheme 7-2: Energy level diagram and a possible mechanism of charge carrier injection in the bR/TiO_2 photoanode cell in the presence of redox electrolyte solution.

7-4 Conclusion

Bacteriorhodopsin/TiO_2 hybrid electrodes were fabricated by anchoring bR molecules onto the surface of anodically fabricated TiO_2 nanotube arrays with and without linkers. When used as photoanodes to split water photoelectrochemically, the assembled bR/TiO_2 electrodes showed better photoelectrochemical performance than that of pure TiO_2 when bR is anchored using a linker. A ~ 50% increase in the photocurrent

density was observed when TiO_2 was sensitized with bR. It is proposed that the enhanced photocurrent generation comes from the proton pumping effect of bR. In the presence of a redox electrolyte, the bR/TiO_2 photoanode achieved even higher photocurrent. This enhancement is based on the band alignment of the HUMO-LUMO levels of bR as related to the band edge positions of TiO_2 in a similar way used in dye-titania systems. The photocurrent response after multiple measurements revealed the high stability of the fabricated hybrid electrode. We believe our bR/TiO_2 hybrid photoanode provides a new perspective method for developing versatile bio-photoelectric devices for solar-to-fuel generation. We are very optimistic that optimization of this system and related assemblies could lead to a breakthrough in the field.

7-5 References

[1] Li, Y.; Kunitake, T.; Fujikawa, S. *J. Phys. Chem. B* **2006**, *110*, 13000.

[2] Ng, Y. H.; Ikeda, S.; Harada, T.; Higashida, S.; Sakata, T.; Mori, H.; Matsumura, M. *Adv. Mater.* **2007**, *19*, 597.

[1] El-Sayed, M. A. *Acc. Chem. Res.* **1992**, *25*, 279.

[2] Pebay-Peyroula, E.; Rummel, G.; Rosenbusch, J. P.; Landau, E. M. *Science* **1997**, *277*, 1676.

[3] Luecke, H.; Richter, H.-T.; Lanyi, J. K. *Science* **1998**, *280*, 1934.

[4] Edman, K.; Nollert, P.; Royant, A.; Belrhali, H.; Pebay-Peyroula, E.; Hajdu, J.; Neutze, R.; Landau, E. M. *Nature* **1999**, *401*, 822.

[5] LaVan, D. A.; Cha, J. N. *Proc. Natl. Acad. Sci. U.S.A.* **2006**, *103*, 5251.

[6] Shen, Y.; Safinya, C. R.; Liang, K. S.; Ruppert, A. F.; Rothschild, K. J. *Nature* **1993**, *366*, 48.

[7] Jin, Y.; Honig, T.; Ron, I.; Friedman, N.; Sheves, M.; Cahen, D. *Chem. Soc. Rev.* **2008**, *37*, 2422.

[8] Chu, L.-K.; Yen, C. W.; El-Sayed, M. A. *Biosens. Bioelectron.* **2010**, *26*, 620.

[9] Yen, C. W.; Chu, L.-K.; El-Sayed, M. A. *J. Am. Chem. Soc.* **2010**, *132*, 7250.

[10] Robertson, B.; Lukashev, E. *Biophys. J.* **1995**, *68*, 1507.

[11] Ormos, P.; Dancshazy, Z.; Karvaly, B. *Biochim. Biophys. Acta* **1978**, *503*, 304.

[12] Hessling, B.; Herbst, J.; Rammelsberg, R.; Gerwert, K. *Biophys. J.* **1997**, *73*, 2071.

[13] Chu, L.-K.; Yen, C. W.; El-Sayed, M. A. *J. Phys. Chem. C* **2010**, *114*, 15358.

[14] Fujishima, A. ; Honda, K. *Nature* **1972**, *238*, 37.

[15] Ni, M.; Leung, M. K. H.; Leung, D. Y. C. ; Sumathy, K. *Renewable and Sustainable Energy Rev.* **2007**, *11*, 401.

[16] Allam, N.K.; Grimes, C.A. *J. Phys. Chem. C* **2009,** *113*, 7996.

[17] Allam, N. K.; El-Sayed, M. A. *J. Phys. Chem. C* **2010**, *114*, 12024.

[18] Allam, N. K.; Alamgir, F.; El-Sayed, M. A. *ACS Nano* **2010**, *4*, 5819.

[19] Conibeer, G. *Materials Today* **2007**, *10*, 42.

[20] Li, C.; Wang, F.; Yu, J. C. *Energy Environ. Sci.* **2011**, *4*, 100.

[21] Oregan, B.; Gräzel, M. *Nature*, **1991**, *353*, 737.

[22] Gräzel, M. *Acc. Chem. Res.* **2009**, *42*, 1788.

[23] Oesterhelt, D. ; Stoeckenius, W. *Methods Enzymol.* **1974**, *31*, 667.

[24] Oesterhelt, D.; Schuhmann, L. *FEBS Lett.* **1974**, *44*, 262.

[25] Wu, S. G.; Awad, E. S.; El-Sayed, M. A. *Biophys. J.* **1991**, *59*, 70.

[26] Grimes, C. A.; Varghese, O. K.; Ranjan, S. Light, Water, Hydrogen: The Solar production of hydrogen by water photoelectrolysis. Springer, Norwell, MA. (2007).

[27] Thavasi, V.; Lazarova, T.; Filpek, S.; Kolinski, M.; Querol, E.; Kumar, A.; Ramakrishna, S.; Padros, E.; Renugopalakrishnan *J. Nanosci. Nanotech.* **2009**, *9*, 1679.

[28]Lu, Y.; Yuan, M.; Liu, Y.; Tu, B. Xu, C. ; Liu, B. ; Zhao, D. ; Kong, J. *Langmuir* **2005**, *21*, 4071.

[29]Li, L. S.; Xu, T.; Zhang, Y. J.; Jin, J.; Li, T. J.; Zou, B. S.; Wang, J. P. *J. Vac. Sci. Technol. A* **2001**, *19*, 1037.

VITA

Chun-Wan Yen

Education

Georgia Institute of Technology, Atlanta, GA Aug 2006-May 2011
Ph.D. in Chemistry and Biochemistry
Major in Inorganic Chemistry, minor in Material Science and Engineering

National Taiwan University, Taipei, Taiwan Aug 2003-Jun 2005
M.S. in Chemistry

National Taiwan University, Taipei, Taiwan Aug 1999-Jun 2003
B.S. in Chemistry, Minor in nanoscience and engineering

Research Experiences

Graduate (Ph. D.) Research
August 2006-present
Prof. Mostafa A El-Sayed
Department of Chemistry and Biochemistry, Georgia Institute of Technology, Atlanta, GA

- Developed a unique hollow metal oxides to degrade pollutant more efficiently
- Synthesize and characterized nanocatalysts and explore their catalytic ability
- Build up a photosynthetic system based solar cell and improved its photocurrent generation by introducing plasmonic effect of metal nanoparticles
- Introduced photosynthetic systems into TiO_2 based fuel cell system and significantly increased the efficiency of electricity generation

Graduate (M. S.) Research
June 2004-May 2005
Prof. Sow-Hsin Chen
National Institute of Standards and Technology, Gaithersburg, MD

- Analyzed the transition of supercooled water by neutron scattering

Graduate (M. S.) Research
Aug 2003-May 2004
Prof. Chung-Yuan Mou
National Taiwan University, Taipei, Taiwan

- Enhanced CO to CO_2 conversion rate by using alloy nanoparticles and applied it into perform PROX reaction in the PEM system
- Analyzed the alloy structure by XAFS experiments (X-ray Absorption Fine Structure)

Award and Honors

- 3^{rd} Place, Georgia Tech Chemistry Graduate Student Awards Symposium 2010.
- Travel Grant Award from Georgia Tech Research and Innovation Conference 2010.

- ◆ Taiwan Merit Scholarship from National Science Council (Taiwan) 2006.
- ◆ Dean's Award for Graduate from College of Science, National Taiwan University, 2005
- ◆ Excellent Dissertation Award, National Taiwan University 2005

Skills

Lab Skills:

- ✓ metallic nanoparticles synthesis (Ag, Au-Ag alloy, Au spheres, and Au nanocages)
- ✓ laser operation (employed Nd:YAG Laser for ultrafast spectroscopy measurement)
- ✓ *Materials Characterization:* x-ray diffraction (XRD), scanning electron microscopy (SEM), scanning tunneling microscopy (STM), BET, transmission electron microscopy (TEM), Gas chromatograph (GC), Dynamic light scattering (DLS), and ICP AES
- ✓ *Spectrometric Characterization:* UV-Vis, FT-IR, and Raman
- ✓ *Synchrotron Radiation Sources Technique:* XAFS, *in-situ* XRD, and neutron scattering

Software:

- ✓ MS Office Suite, Origin, Photoshop, and ChemOffice Suite

Publications (selected):

- ■ Chu, L.-K.; **Yen, C. W**.; El-Sayed, M. A. "Bacteriorhodopsin-based photo-electrochemical cell" *Biosens. Bioelectron.* **2010**, *26*, 620.
- ■ **Yen, C. W.**; Chu, L.-K.; El-Sayed M. A. "Kinetic and spectroscopic study on the mechanism of the solar-to-electric energy conversion by the other photosynthetic system in nature: bacteriorhodopsin" *J. Phys. Chem. C* **2010**, *114*, 15358.
- ■ **Yen, C. W.**; Chu, L.-K.; El-Sayed, M. A. "Plasmonic field enhancement of the bacteriorhodopsin photocurrent during its proton pump photocycle" *J. Am. Chem. Soc.* **2010**, *132*, 7250.
- ■ **Yen, C. W.**; El-Sayed, M. A. "Plasmonic field effect on electron transfer catalytic reaction on gold nanoparticles" *J. Phys. Chem. C* **2009**, *113*, 19585.
- ■ **Yen, C. W.**; Mahmoud, M. A.; El-Sayed, M. A. "Photocatalysis in gold nanocage nanoreactors" *J. Phys. Chem. A.* **2009**, *113*, 4340.
- ■ **Yen, C. W.;** Lin, M. L.; Wang, A. Q.; Chen, S. A.; Chen, J. M.; Mou, C. Y. "CO oxidation catalyzed by Au-Ag bimetaliic nanoparticles confined in mesoporous silica" *J. Phys. Chem C* **2009**, *113*, 17831.

Teaching Experiences:

Teaching Assistant for General Chemistry — Aug 2006-May 2007
Georgia Institute of Technology, Atlanta, GA

Teaching Laboratory Assistant for Analytical Chemistry — Aug 2003-May 2004
National Taiwan University, Taipei, Taiwan

Extracurricular Activities

Volunteer, Girls Inc. — Jan 2011
Volunteer, National Nanotechnology Youth Outreach Program — Jun 2010

Member, World Vision Organization Dec 2008-present

Presentations

2010 The 8th Cross-Strait Workshop on Nanoscience and Technology, *Hong Kong*
"Application of Nanotechnology in the Plasmonic Enhancement of the Solar-to-Electric Energy Conversion by Bacteriorhodopsin" (oral)

2010 Georgia Life Sciences Summit, Atlanta, GA
"Application of nanotechnology in the plasmonic enhancement of the solar-to-electric energy conversion by Bacteriorhodopsin" (poster)

2010 Georgia Tech Research and Innovation Conference, *Atlanta*, GA
"Nanotechnology applications on environment, catalysis, and energy" (poster)

2010 Spring American Chemical Society Meeting, *San Francisco*, CA
"Photocatalysis in gold nanocage nanoreactors" (poster)